

**NASA CONTRACTOR
REPORT**

NASA CR-1757



NASA CR-17

Q.1

0060804

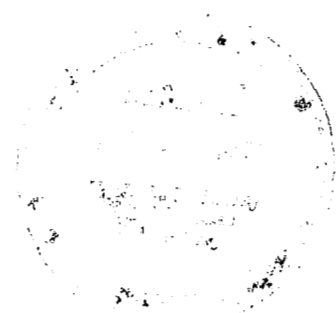


**LOAN COPY: RETURN TO
AFWL (DOGL)
KIRTLAND AFB, N. M.**

**EXPERIMENTAL VALIDATION
AND ANALYTICAL ELABORATION
FOR MODELS OF THE PILOT'S
NEUROMUSCULAR SUBSYSTEM
IN TRACKING TASKS**

by R. E. Magdaleno and D. T. McRuer

*Prepared by
SYSTEMS TECHNOLOGY, INC.
Hawthorne, Calif.
for Ames Research Center*





0060804

| | | | | | |
|---|--|--|--|--|--|
| 1. Report No. NASA CR-1757 | | 2. Government Accession No. | | 3. Recipient's Catalog No. | |
| 4. Title and Subtitle Experimental Validation and Analytical Elaboration for Models of the Pilot's Neuromuscular Subsystem in Tracking Tasks | | | | 5. Report Date April 1971 | |
| | | | | 6. Performing Organization Code | |
| 7. Author(s) R.E. Magdalenos and D. T. McRuer | | | | 8. Performing Organization Report No. | |
| | | | | 10. Work Unit No. | |
| 9. Performing Organization Name and Address Systems Technology, Inc. Hawthorne, California | | | | 11. Contract or Grant No. NAS 2-4828 | |
| | | | | 13. Type of Report and Period Covered Contractor Report | |
| 12. Sponsoring Agency Name and Address National Aeronautics & Space Administration Washington, D.C. 20546 | | | | 14. Sponsoring Agency Code | |
| | | | | | |
| 15. Supplementary Notes | | | | | |
| 16. Abstract <p>The purpose of the experiments is to obtain direct describing function data for the muscle/manipulator actuation element, G_m, portion of the whole human, Y_p, in tracking situations. Both these describing functions were measured in a single-loop compensatory situation where the pilot used either a rudder pedal or a hand manipulator and controlled a first-order subcritical task $[\lambda_1/(s-\lambda_1)]$ for a variety of instability values. In addition second- and third-order subcritical tasks (hand manipulator only) were run to investigate neuromuscular system effects when the pilot must generate low-frequency lead. G_m for rudder pedals and hand manipulator was quite similar in form and close in bandwidth. A spinal level closed-loop neuromuscular system was obtained which gives an excellent fit to the data if the alpha command signal is the command input to the neuromuscular system. The feedback path assumptions imply that muscle spindles are the dominant element for stiff spring restraints although the Golgi tendon organs fulfill a similar role. In addition the joint angle sensors may modify the pilot's dynamics for free-moving manipulators. For the hand manipulator G_m was basically unchanged for first-, second-, and third-order subcritical tasks, where the pilot must generate none, first-, and second-order low-frequency lead respectively, indicating that this lead is generated centrally rather than involving the peripheral neuromuscular system. The time delay penalty involved in computing low-frequency lead is inferred from some precision curve fits. The data in this report validate the neuromuscular systems basic organization and dynamics in actual tracking situations. Once the detailed identification of model elements in the muscle/manipulator dynamics is done then the likely effects of control system nonlinearities (e.g., hysteresis, backlash, Coulomb friction, preload) on pilot/vehicle system stability and performance could be obtained by simulation or via describing function analysis and/or measurement.</p> | | | | | |
| 17. Key Words (Suggested by Author(s)) neuro-muscular subsystem pilot describing function lead generating tasks | | | 18. Distribution Statement UNCLASSIFIED-UNLIMITED | | |
| 19. Security Classif. (of this report) Unclassified | | 20. Security Classif. (of this page) Unclassified | | 21. No. of Pages 81 | |
| | | | | 22. Price* 3.00 | |

FOREWORD

This report was prepared under Contract NAS2-4828 between Systems Technology, Inc., Hawthorne, California, and the NASA-Ames Research Center, Man/Machine Integration Branch. The NASA project monitors were Mr. M. Sadoff and Mr. C. B. Dolkas. STI technical director was Mr. Duane T. McRuer and the project engineer was Mr. Raymond E. Magdaleno. The authors would like to thank Mr. R. H. Klein and Mr. R. W. Allen for their efforts in the setting up and running of the experiments and aiding in the data reduction.

ABSTRACT

The purpose of the experiments is to obtain direct describing function data for the muscle/manipulator actuation element, G_m , portion of the whole human, Y_p , in tracking situations. Both these describing functions were measured in a single-loop compensatory situation where the pilot used either a rudder pedal or a hand manipulator and controlled a first-order subcritical task $[\lambda_1/(s-\lambda_1)]$ for a variety of instability values. In addition second- and third-order subcritical tasks (hand manipulator only) were run to investigate neuromuscular system effects when the pilot must generate low-frequency lead.

The rudder pedal manipulator has an inherently balanced agonist/antagonist muscle system and consequently produced the highest quality data for the processed EMG signals used to find G_m . G_m for rudder pedals and hand manipulator was quite similar in form and close in bandwidth despite the difference in limb size and function (the form has a small time delay plus a low pass third-order system with all modes above 10 rad/sec).

The rudder pedal experiments showed that the pilot's effective time delay decreased as average tension increased (providing the first direct validation of this oft stated relationship). Typical high frequency peaks in Y_p are due to the closed-loop neuromuscular system. Using a curve fit to a direct measurement of G_m and some reasonable assumptions about the effective feedback path yields a spinal level closed-loop neuromuscular system which gives an excellent fit to the data if the alpha command signal is the command input to the neuromuscular system. The feedback path assumptions imply that muscle spindles are the dominant element for stiff spring restraints although the Golgi tendon organs fulfill a similar role. In addition the joint angle sensors may modify the pilot's dynamics for free-moving manipulators.

For the hand manipulator G_m was basically unchanged for first-, second-, and third-order subcritical tasks, where the pilot must generate none, first-, and second-order low-frequency lead respectively, indicating that this lead is generated centrally rather than involving the peripheral neuromuscular system. The time delay penalty involved in computing low-frequency lead is inferred from some precision curve fits.

The data in this report validates the neuromuscular systems basic organization and dynamics in actual tracking situations. Once the detailed identification of model elements in the muscle/manipulator dynamics is done then the likely effects of control system nonlinearities (e.g., hysteresis, backlash, Coulomb friction, preload) on pilot/vehicle system stability and performance could be obtained by simulation or via describing function analysis and/or measurement.

CONTENTS

| | <u>Page</u> |
|--|-------------|
| I. INTRODUCTION. | 1 |
| A. Review of Data Bank | 2 |
| B. Review of Human Operator Describing Function Models — Effects of Forcing Function and Controlled Element Variations | 5 |
| C. Human Operator Subsystems | 7 |
| D. Purposes and Outline of Report. | 17 |
| II. EXPERIMENTAL PLAN, APPARATUS AND MEASUREMENT TECHNIQUES . . | 19 |
| A. Matrix of Experiments. | 21 |
| B. Rudder Pedal Muscle Groups | 22 |
| C. Hand Manipulator | 25 |
| D. EMG Signal Conditioning | 27 |
| E. Manipulator Characteristics. | 32 |
| F. Forcing Functions | 33 |
| G. Data Reduction Equipment. | 33 |
| H. Digital Data Reduction | 35 |
| I. Subjects | 37 |
| III. EXPERIMENTAL DESCRIBING FUNCTION COMPARISONS — NEUROMUSCULAR SYSTEM AND WHOLE HUMAN | 38 |
| A. Rudder Pedal Data | 38 |
| B. Hand Manipulator Data Comparisons. | 45 |
| C. Conclusions | 57 |
| IV. DESCRIBING FUNCTION DATA INTERPRETATION AND MODEL REVISION . | 59 |
| A. Neuromuscular System Model | 59 |
| B. Closed-Loop Neuromuscular System for Various Manipulator Restraints | 61 |
| C. Effects of Low Frequency Lead Generation on Y_p | 67 |
| D. Revised Muscle/Manipulator Dynamics Model | 73 |
| V. CONCLUSIONS | 78 |
| REFERENCES | 80 |

FIGURES

| | <u>Page</u> |
|---|-------------|
| 1. General Compensatory Control Situation and Basic Human Operator Subsystems. | 3 |
| 2. Typical Pilot Describing Function Data and Models [$Y_c = K_c/(s-2)$; $\omega_1 = 4.0$ rad/sec] (Ref. 6). | 8 |
| 3. Pilot/Vehicle System for Head-Fixed Attitude Control Tasks | 9 |
| 4. Idealized Agonist/Antagonist Muscle Pair. | 10 |
| 5. Functional Diagram of Agonist/Antagonist Neuromuscular System Elements Involved in Tracking | 11 |
| 6. Simplified Neuromuscular System Model. | 14 |
| 7. General Arrangement of Equipment | 20 |
| 8. Subject Using Rudder Pedals and EMG Electrodes. | 23 |
| 9. Thigh and Leg Geometry for ± 13 cm Movement | 23 |
| 10. Cross Section Through the Middle of the Thigh Looking Toward the Body. Four-fifths of Natural Size. | 24 |
| 11. Primary Wrist-Manipulator Actuation Muscles. | 26 |
| 12. Muscle Action Potential (EMG) Processing to Obtain Effective Muscle Actuation Signal and Average Tension. | 27 |
| 13. Example Time History for EMG Signal Processing; $Y_c = K_c/(s-2)$ | 30 |
| 14. Average Tension Versus Force for Rudder Pedals. | 31 |
| 15. Human Operator Describing Function, Y_p , Rudder Pedals, $Y_{c1} = 1/(s-1)$ | 39 |
| 16. Effects of Controlled Element Divergence on the Human Operator Describing Function, Y_p , Rudder Pedals, $Y_{c1} = \lambda_1(s-\lambda_1)$, $\lambda_1 = 0.25$ and 2.0 | 40 |
| 17. Muscle/Manipulator Describing Function, G_m , Rudder Pedals, $Y_{c1} = 0.25/(s-0.25)$ | 42 |
| 18. Muscle/Manipulator Describing Function, G_m , Rudder Pedals, $Y_{c1} = 1/(s-1)$ | 43 |
| 19. Muscle/Manipulator Describing Function, G_m , Rudder Pedals, $Y_{c1} = 2/(s-2)$ | 44 |

| | |
|---|----|
| 20. Tie-In of Mean-Square Tracking Error and Error Coherence with Previous Data (Ref. 11). | 47 |
| 21. Human Operator Describing Function, Y_p , for First- and Second-Order Tasks (Hand Manipulator) | 48 |
| 22. Effects of Controlled Elements Requiring Lead Generation on the Human Operator's Describing Function, Y_p (Hand Manipulator). | 51 |
| 23. Muscle/Manipulator Describing Function, G_m [Hand Manipulator, $Y_{c1} = 1/(s-1)$] | 53 |
| 24. Muscle/Manipulator Describing Function, G_m [Hand Manipulator, $Y_{c1} = 3/(s-3)$] | 54 |
| 25. Muscle/Manipulator Describing Function, G_m [Hand Manipulator, $Y_{c2} = 0.5/s(s-0.5)$] | 55 |
| 26. Muscle/Manipulator Describing Function, G_m [Hand Manipulator, $Y_{c3} = 0.3/s^3(s-0.3)$] | 56 |
| 27. Neuromuscular Subsystems for Free-Moving and Pressure Manipulators and Central Equalization for Rate Dynamics | 60 |
| 28. Example Describing Function Showing High-Frequency Peak | 62 |
| 29. Bode and Root Locus for Spindle Feedback (Some Effects of Joint Sensor Feedback Shown) | 64 |
| 30. Closed-Loop Neuromuscular System Model Fit to Y_p for Pressure and Free-Moving Manipulator (Ref. 20, $Y_c = 1/s$) | 65 |
| 31. Closed-Loop Neuromuscular System Model Fit to Y_p [Rudder Pedal, $Y_{c1} = 1/(s-1)$] | 68 |
| 32. Neuromuscular Subsystem for Pressure Manipulator and Central Equalization Form for First- and Second-Order Dynamics | 69 |
| 33. Precision Fit to Human Operator Describing Function, Y_p [Hand Manipulator, $Y_{c1} = 1/(s-1)$] | 71 |
| 34. Precision Fit to Human Operator Describing Function, Y_p/s [Hand Manipulator, $Y_{c2} = 0.5/s(s-0.5)$] | 72 |
| 35. Schematic Diagram of Muscle/Manipulator Elements | 74 |

TABLES

| | <u>Page</u> |
|---|-------------|
| I. Matrix of Experiments. | 22 |
| II. Rudder Pedal Forcing Function | 33 |
| III. Forcing Function Spectra (Hand Manipulator) | 34 |
| IV. Summary of Average Tension Effects | 45 |
| V. Error Performance Measures for Second-Order Tasks with Various Instability Values | 50 |
| VI. Error Performance Measures for Effects of Lead Generation. . | 50 |
| VII. Effective Time Delay Components | 73 |
| VIII. Effect of Spring Restraint on s^0 Term of Δ | 76 |

SYMBOLS

| | |
|-----------------------------|---|
| a_1 | Local linear acceleration |
| b_m | Equivalent damper for muscle system |
| $c(t)$ | Limb position; human operator output |
| C_f | Constant of proportionality for average motor nerve firing rate |
| dB | Decibel, $20 \log_{10} ()$ for amplitude ratio; $10 \log_{10} ()$ for power |
| e | Error |
| EMG | Electromyogram |
| $f_1()$, $f_2()$ | Functional dependence on () |
| Δf_α | Incremental alpha motor neuron firing rate |
| Δf_s | Static fiber perturbation firing rate |
| F | Muscle output force; also disturbance force |
| F_c | Control force |
| G_m or $G_m(\gamma_o)$ | Muscle/manipulator dynamics describing function |
| H_J | Effective joint feedback |
| $i(t)$ | Forcing function |
| I_a | Primary or annulospiral ending |
| j | $\sqrt{-1}$ |
| $j\omega$ | Imaginary part of the complex variable, $s = \sigma \pm j\omega$ |
| k_e | Series elastic component of muscle |
| k_F | Manipulator spring rate |
| k_I | Interface compliance |
| k_m | Equivalent spring gradient for muscle |
| k_T | Tendon and series elastic compliance |
| K | System gain |
| K_C | Controlled element gain |

| | |
|-------------------------------|---|
| K_J | Gain of effective joint feedback |
| K_{NM} | Gain of closed-loop neuromuscular system |
| K_p | Human pilot gain |
| K_{sp} | Spindle describing function gain |
| m | System output |
| m_F | Feel system inertia |
| m_L | Limb inertia |
| ms | Millisecond |
| n | Number of degrees of freedom |
| P_O | Operating point tension |
| P_{sp} | Spindle pole |
| q_1 | Local angular velocity at canals |
| $R_{xy}(\tau)$ | Cross correlation function |
| s | Complex variable, $s = \sigma \pm j\omega$; Laplace transform variable |
| t | Time |
| T_I | General lag time constant of human pilot describing function |
| T_K, T'_K | Lead and lag time constants in precision model of human pilot describing function |
| $1/aT_K$ | Open-loop spindle model pole |
| T_{lag_i} T_{lead_i} } | General lag and lead time constants |
| T_L | General lead time constant of human pilot describing function |
| T_m | Maximum lag time |
| T_N | First-order lag time constant approximation of the neuromuscular system |
| T_{N_1} | First-order lag time constant of the neuromuscular system |
| T_R | Run length |
| x_b | Bone position |

| | |
|--------------------|---|
| x_m | Spindle model length |
| x_m | Internal muscle length |
| $x(t)$ | Net effective actuation signal to muscle/manipulator dynamics |
| $Y_c(j\omega)$ | Controlled element transfer function |
| Y_p | Pilot describing function |
| Z_{sp} | Spindle lead break frequency |
| α | Low frequency phase approximation parameter |
| α', α | Alpha motor neuron signal to muscle (agonist, antagonist) |
| α_c | Alpha motor neuron command |
| α_v | Input to oculomotor nucleus |
| α_{vc} | Oculomotor command |
| γ | Gamma command following gamma motor neuron delay |
| γ_b | Gamma bias input due to γ_d |
| γ_c | Gamma command input |
| γ_o | Total gamma bias |
| Δ | Denominator of input-output response of model for G_m |
| $\Delta\phi_{low}$ | Incremental low frequency phase angle |
| ϵ_v | Eyeball position error |
| ζ_a | Damping ratio of second-order term in G_m |
| ζ_N | Closed-loop damping ratio of second-order neuromuscular system term |
| θ | Pitch attitude |
| θ_i | Pitch attitude command |
| λ_i | Controlled element unstable pole position |
| λ_v | Eyeball position |
| ρ^2 | Sample correlation coefficient |

| | |
|------------------|---|
| ρ_E^2 | Relative correlated error = $\sigma_{e_i}^2/\sigma_e^2$ |
| σ | Real axis of complex plane |
| σ_e^2 | Mean-square error |
| $\sigma_{e_i}^2$ | Mean-square error correlated with forcing function |
| $\sigma_{e_n}^2$ | Mean-square error not correlated with forcing function |
| σ_i | Root mean-square input |
| τ | Pure time delay |
| τ_a | Time delay in G_m |
| τ_c | Central time delay |
| τ_e | Effective time delay |
| τ_j | Time delay in joint angle feedback |
| τ_{NM} | Time delay of closed-loop neuromuscular system |
| τ_{sp} | Spindle time delay |
| τ_α | Net time delay in the alpha motor neuron pathway |
| τ_γ | Net time delay in the gamma motor neuron pathway |
| ϕ_m | Phase margin |
| ϕ_{ic} | Cross-spectra between i and c |
| ϕ_{ie} | Cross-spectra between i and e |
| ϕ_{ix} | Cross-spectra between i and x |
| ϕ_{xc} | Cross-spectra between x and c |
| ϕ_{xx} | Cross-spectra between x and x |
| ϕ_{xy} | Cross-spectra between x and y |
| ω | Angular frequency, rad/sec |
| ω_a | Natural frequency of second-order term in G_m |
| ω_c | Crossover frequency |
| ω_i | Forcing function bandwidth |

| | |
|--------------|--------------------|
| $ $ | Magnitude |
| Π | Product |
| \uparrow | Increase |
| \downarrow | Decrease |
| ∂ | Partial derivative |
| \angle | Phase angle |

SECTION I

INTRODUCTION

The general purpose of this report is to present data and interpretations for the human operator's major subsystems involved in tracking tasks. The main concerns will be the neuromuscular system and the central computing capabilities involved in low-frequency lead generation. For the neuromuscular system the tentative model underlying the experimental program is that advanced in Ref. 1 as a synthesis of the data and models of a great many workers. The experiments and data to be presented were planned in the context of this model; the experimental data thus provide either validation or bases for modification to the model. The low-frequency lead generation capabilities have nowhere near as solid a background in terms of models (Chapter IV of Ref. 2 contains simplified first approaches). This report will not attempt to validate any particular low-frequency lead generation model but rather will provide data and interpretation to the neuromuscular systems role when the human operator is generating this type of lead.

The introduction to Ref. 1 describes three aspects of our interest in engineering descriptions of the neuromuscular system. These are repeated below to facilitate referring to them later:

Manual control engineering—The basic dynamics of the human operator and the precision of manual control are critically limited by the properties of the neuromuscular system. A basic understanding of this system will have important practical ramifications in better appreciating these limitations, as well as in determining the likely effects of control system nonlinearities (e.g., hysteresis, backlash, Coulomb friction, preload) on pilot/vehicle system stability and performance. This, in turn, should ultimately lead to a better understanding of some kinds of pilot-induced oscillations, and to the establishment of necessary or sufficient conditions for their elimination.

Control theoretic—The neuromuscular system is an archetypical adaptive actuation system which, if understood operationally, might serve as the inspiration for analogous inanimate systems with similarly useful properties.

Physiological system description—Systems engineering descriptions are a natural language for integrating the rapidly expanding knowledge of biological servomechanisms, and serve to implement the interpretation of physiological data, construct and validate models of basic physiological processes, and suggest further experimentation.

The data and interpretations to be discussed in this report go a long way towards providing an understanding of load impedance on the neuromuscular system (manual control engineering). From time to time we shall comment on the control theoretic and physiological system description aspects.

The remainder of this Introduction is devoted to a review of background data and definitions for both the whole human and neuromuscular system. Included are interpretations of recent findings as well as reinterpretations of old findings.

A. REVIEW OF DATA BANK

Within the last fifteen years there has been a number of major experimental programs to determine random-input describing functions of the human operator in compensatory situations, e.g., Refs. 3-8. The general control situation is illustrated in Fig. 1. The key task variables are the manipulator load dynamics, the forcing function, and the controlled element characteristics. Much of the past work on overall human operator dynamics has been concerned with the effects of controlled element and forcing function with the manipulator characteristics held constant. For instance, in the comprehensive experimental and analytical study of human pilot dynamics (Ref. 6) the manipulator was eliminated as a task variable by using the same spring-restrained sidestick for all controlled element and input bandwidth combinations. In other series (Refs. 7 and 8) the manipulator was an important experimental variable. Reference 7 reports on a study of cases comparing human operator dynamics using free-moving, pressure (strain gauge), and spring-restrained sidesticks. Reference 8 treats an extremely wide range of spring and inertia manipulator restraint dynamics, used with pure gain and acceleration controlled-element dynamics.

All of the studies mentioned above provide some instances where high frequency dynamics suggestive of neuromuscular system modes are revealed; however these effects are not always found in a form that could be uniquely attributed to the neuromuscular system. Part of the problem is that the manipulator load interacts with muscle dynamics, i.e., muscles are not accurately described by a zero output impedance black box representation.

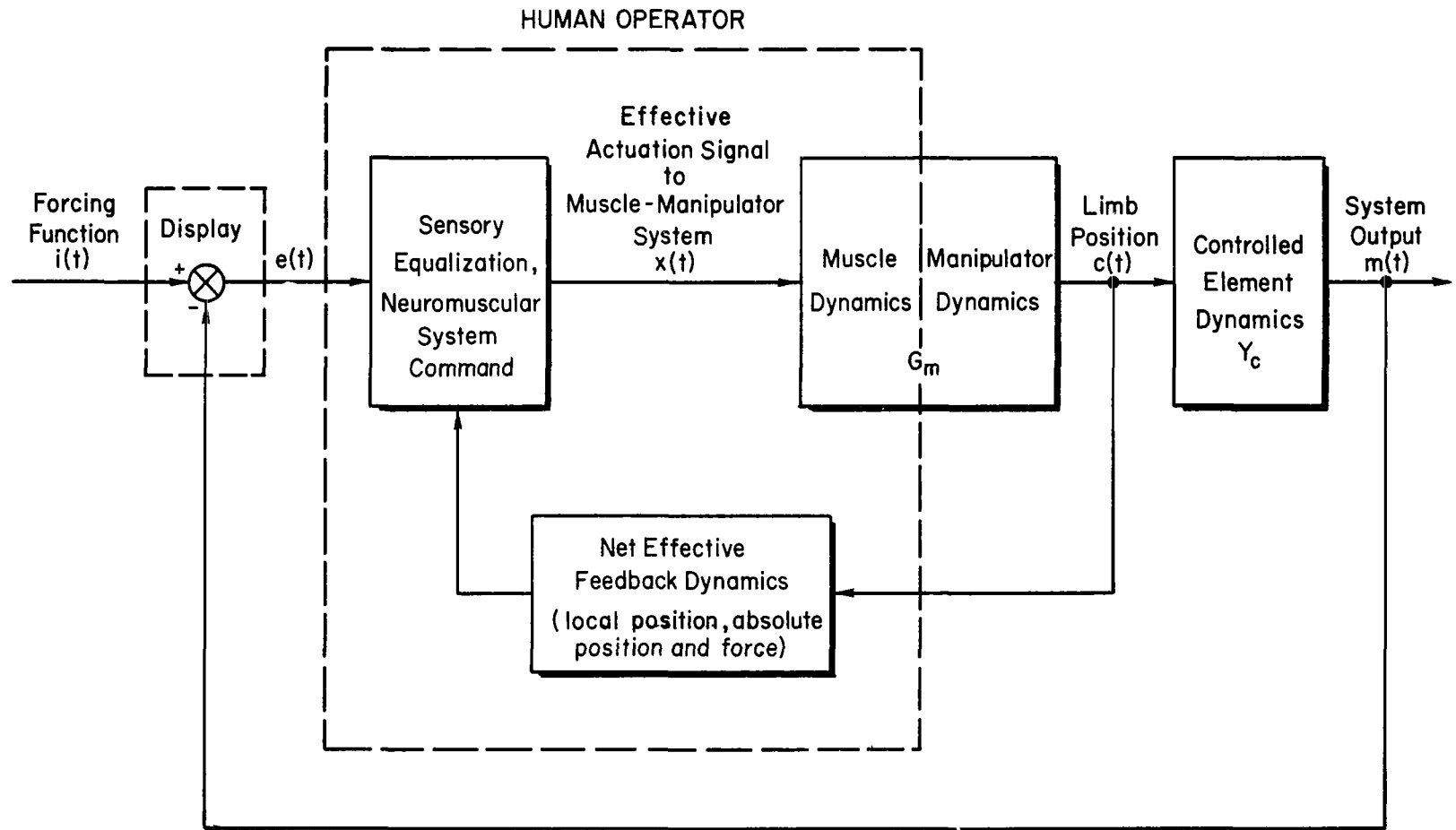


Figure 1. General Compensatory Control Situation and Basic Human Operator Subsystems

This is indicated in a general way in Fig. 1 which depicts the human operator's general subsystems. The muscle-manipulator dynamics describing function, G_m , produces the limb position, $c(t)$, in response to a net effective actuation signal, $x(t)$. (The details for obtaining $x(t)$ from processed electromyogram (EMG) signals are given in the next section.) As indicated in Fig. 1 the neuromuscular system describing function responds to both sensed visual inputs as well as to a net effective feedback. The latter may include information as to the load's local and absolute position as well as force.

References 9-11 used the Critical Task concept (control of a system with an unstable real root) to explore some of the pilot's limiting capabilities. Of most interest for the neuromuscular system and low-frequency lead generation are the first- and second-order critical tasks.* For these the critical values of the unstable real roots are associated with the pilot's effective time delay. In the first-order critical task, which exhibits little or no pilot equalization, a major portion of the effective time delay is connected with the neuromuscular system. For second-order tasks the time delay is larger than for first-order tasks. The time delay exhibits additional components due to the presence of the low-frequency lead equalization needed to provide system stability. Consequently, the difference between the first- and second-order effective time delay results can, at least partially, be attributed to the lead equalization. Besides these fundamental connections with neuromuscular dynamics and lead equalization the use of critical and subcritical tasks generally produces high quality data with low variability. Recently (Ref. 11) this concept has been refined and realized in terms of measurement and analysis equipment that gives high quality data even for some extremely difficult controlled elements requiring precise pilot equalization. This equipment was used for the experiments described in this report.

*A first-order subcritical task is $Y_c = \lambda_1 / (s - \lambda_1)$, a second-order is $\lambda_2 / s(s - \lambda_2)$ and a third-order is $\lambda_3 / s^2(s - \lambda_3)$. These tasks become "critical" for values of λ_i that the pilot can just stabilize.

B. REVIEW OF HUMAN OPERATOR DESCRIBING FUNCTION MODELS — EFFECTS OF FORCING FUNCTION AND CONTROLLED ELEMENT VARIATIONS

The extensive experimental series in Ref. 6 yielded an excellent data base for modeling the overall human operator describing function, and to a certain extent the various subsystems involved. For some configurations, the data were of such low variability that a relatively complex model form (Precision Model) was the minimum necessary to yield an adequate fit. This model plus the Approximate Model form are given below:

Precision Model

$$Y_p = \left[\begin{array}{c} \text{Equalization} \\ \text{and Gain} \end{array} \right] \left[\begin{array}{c} \text{Basic} \\ \text{Delays} \end{array} \right] \left\{ \underbrace{\left(\frac{T_K j\omega + 1}{T_K' j\omega + 1} \right)}_{e^{-j\alpha/\omega}} \underbrace{\frac{1}{(T_{N1} j\omega + 1) \left[\left(\frac{j\omega}{\omega_N} \right)^2 + \frac{2\zeta_N j\omega}{\omega_N} + 1 \right]}}_{(T_N j\omega + 1)^{-1} \text{ or } e^{-j\omega T_N}} \right\} \quad (1)$$

where

$$\alpha \doteq \frac{1}{T_K'} \pm \frac{1}{T_K}$$

where

$$T_N \doteq T_{N1} + \frac{2\zeta_N}{\omega_N}$$

Approximate Model

$$\begin{aligned} Y_p &= K_p \left(\frac{T_L j\omega + 1}{T_I j\omega + 1} \right) e^{-j\omega\tau} \left(\frac{e^{-j\alpha/\omega}}{T_N j\omega + 1} \right) \\ &\doteq K_p \left(\frac{T_L j\omega + 1}{T_I j\omega + 1} \right) e^{-j[\omega\tau_e + \alpha/\omega]} \end{aligned} \quad (2)$$

where $\tau_e = \tau + T_N$; the net effective time delay. The so-called Precision Model is a minimum form compatible with all the fine-detail, low-variability, data for random-appearing forcing functions and also compatible with such things as the dynamics of the movement component in step responses. The Approximate Model is a much simpler form in which the number of parameters

is reduced without too serious a degradation in the analytical description of the data for mid-frequencies. Both models exhibit the same gain, equalization, and basic delay elements. They differ in their neuromuscular system aspects. For these the high-frequency terms are third-order in the Precision Model. In the Approximate Model, the mid-frequency effects of these third-order terms are approximated by either a first-order lag (so-called neuromuscular lag) or a pure time delay. The latter can be summed with the basic latencies to give an overall time delay, τ_e .

The very-low-frequency characteristics appear in the data primarily as a phase lag. In the Precision Model these characteristics are represented by the lead/lag, $(T_K j\omega + 1)/(T'_K j\omega + 1)$, which is a minimum form suitable to characterize both amplitude ratio and phase data completely for the limited data of extremely high precision [primarily data for controlled element forms K_C , K_C/s , and $K_C/(s - \lambda)$]. For many other systems these low-frequency effects are not so precise, and more gross approximations are in order. If the low-frequency effects are modeled by transfer characteristics containing m lags and leads, then the incremental phase shift due to these will be

$$\Delta\phi_{\text{low}} = \sum_{i=1}^m \tan^{-1} (\omega T_{\text{lead}_i}) - \sum_{i=1}^m \tan^{-1} (\omega T_{\text{lag}_i}) \quad (3)$$

At frequencies well above the break frequencies of these lags and lead, i.e., $\omega > 1/T_{\text{lead}_i}$, $1/T_{\text{lag}_i}$, this can be approximated by

$$\begin{aligned} \Delta\phi_{\text{low}} &= \sum_{i=1}^m \left(\frac{\pi}{2} - \frac{1}{\omega T_{\text{lead}_i}} \right) - \sum_{i=1}^m \left(\frac{\pi}{2} - \frac{1}{\omega T_{\text{lag}_i}} \right) \quad (4) \\ &= -\frac{1}{\omega} \underbrace{\sum_{i=1}^m \left(\frac{1}{T_{\text{lead}_i}} - \frac{1}{T_{\text{lag}_i}} \right)}_{\alpha} \end{aligned}$$

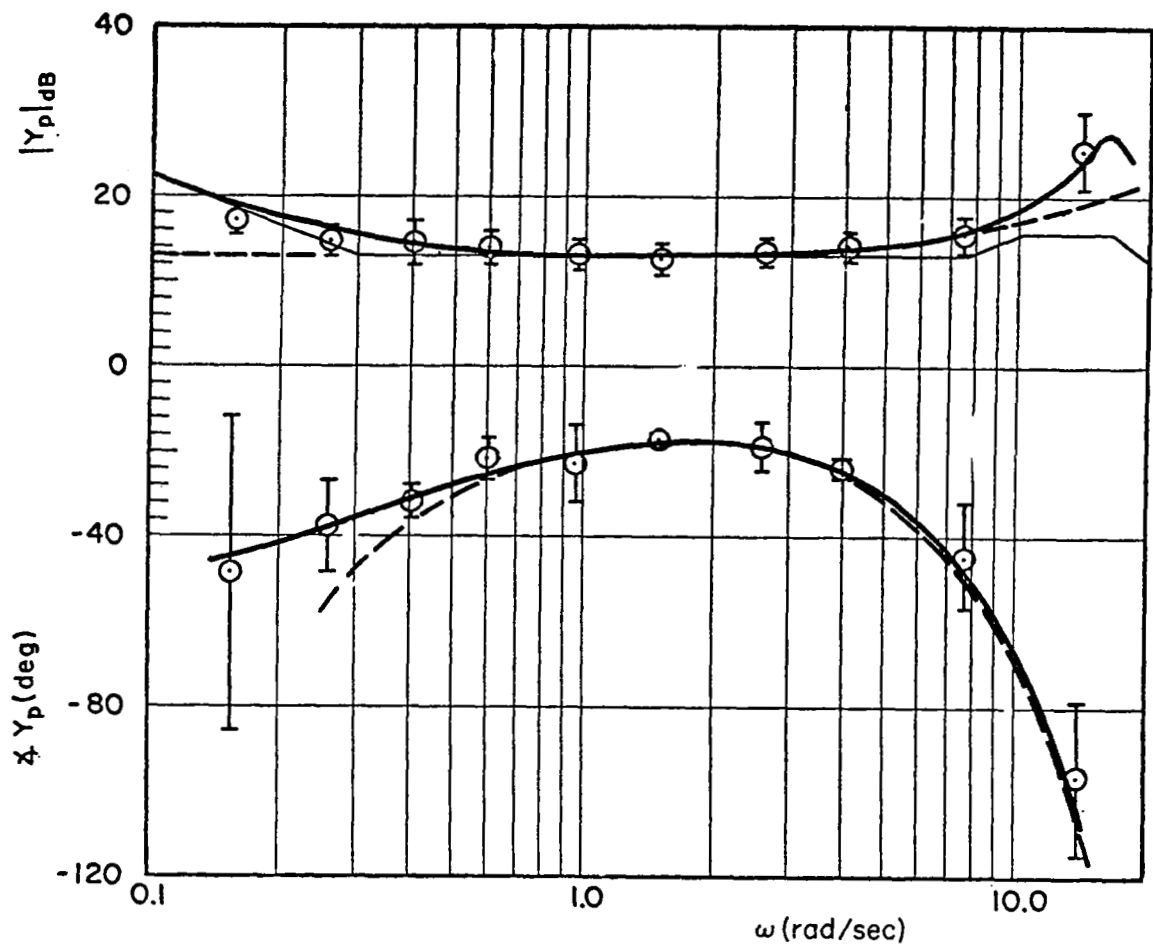
Thus, this $e^{-j\alpha/\omega}$ phase characteristic is convenient to approximate the effects at mid-frequencies of very-low-frequency leads and lags. The

emphasis here will be on the α and equivalent time delay quantities contained in the Approximate Model's exponential phase descriptor term, $e^{-j(\omega\tau_e + \alpha/\omega)}$.

Figure 2 illustrates the nature of typical pilot describing function data and the application of the previously given Precision and Approximate Model forms as descriptors of these data. The typical data shown are from a so-called subcritical task involving the control of a first-order divergence controlled element with $\lambda = 2$ rad/sec. The α and τ_e aspects do not affect the amplitude ratio at all, although they are clearly shown in the phase. The $\omega\tau_e$ phase due to time delay dominates the high frequencies, whereas the α/ω phase lag is the major low frequency effect. Their joint action tends to make the approximate phase look like an umbrella, with α controlling the left side and τ_e the right side, i.e., changes in τ_e shift the right side of the umbrella, while changes in α shift the left. Simultaneous increases or decreases in both α and $1/\tau_e$ shift the umbrella to the right or left, respectively. This "umbrella" description will be referred to later to aid in data interpretation.

C. HUMAN OPERATOR SUBSYSTEMS

Figure 3 (modified from Ref. 2) illustrates some of the human operator subsystems involved in visual-input, limb-output tracking tasks in control of a vehicle. The optics and retina sense the visual stimulus position, and possibly its velocity, as well as errors due to eyeball position changes. We shall presume that the latter are not important for the tasks contemplated in this report since our previous experience indicates that these tasks can be controlled with a stare mode. In the central nervous system the visual channel equalization is one source for the low-frequency lead equalization required for control of vehicle dynamics approximating $Y_c = K_c/s^2$. The other source of this lead is direct sensing of velocity. Reference 2 presents first cut models for direct sensing of velocity and for central computation of low-frequency lead. Both of these contain time delay increments involved in computing or sensing this low-frequency lead. Controlled elements approximating $Y_c = K/s^3$ will require both methods of lead computation. The output of the equalization for the visual



Precision Model (—)

$$Y_p = (25.1) \left(\frac{j\omega}{7.8} + 1 \right) e^{-0.09j\omega} \left\{ \left(\frac{\frac{j\omega}{0.3} + 1}{\frac{j\omega}{0.05} + 1} \right) \frac{1}{\left(\frac{j\omega}{10} + 1 \right) \left[\left(\frac{j\omega}{16.5} \right)^2 + \frac{2(0.12)}{16.5} j\omega + 1 \right]} \right\}$$

Approximate Model (---)

$$Y_p = (4.2) \left(\frac{j\omega}{7.8} + 1 \right) e^{-1[0.21\omega + (0.25/\omega)]}$$

Figure 2. Typical Pilot Describing Function Data and Models
 $[Y_c = K_c/(s-2); \omega_1 = 4.0 \text{ rad/sec}]$ (Ref. 6)

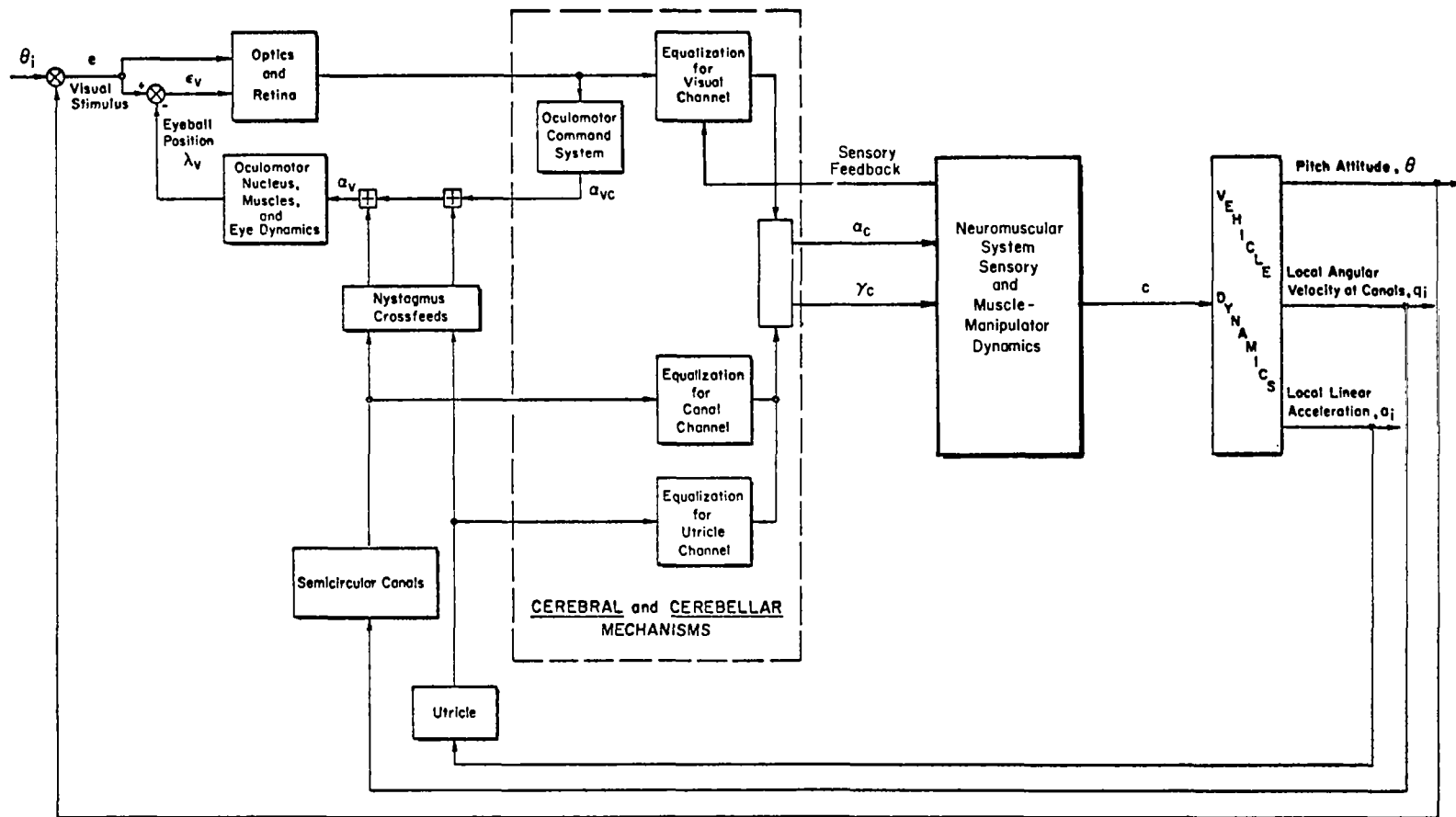


Figure 3. Pilot/Vehicle System for Head-Fixed Attitude Control Tasks

channel then feeds the neuromuscular system toward which a major portion of this report is devoted. The vestibular feedbacks and their crossfeeds to both eyeball dynamics and the direct drives to the neuromuscular system are included in Fig. 3 to complete the picture of the major subsystems, although they will not be covered in this report.

Figure 3 also shows the neuromuscular system output, c , in response to α , α_c , and γ , γ_c , command inputs (to be discussed shortly) as well as sensory feedback into the visual channel equalization. The tracking tasks considered in this report involve relatively small movements. At minimum there will be an agonist/antagonist muscle pair where each has an average tension (which does not appear across the load). Figure 4 shows such a pair for an idealized system. For motion to occur, one muscle must relax while the other contracts, and thus the tension levels must seesaw about the average.

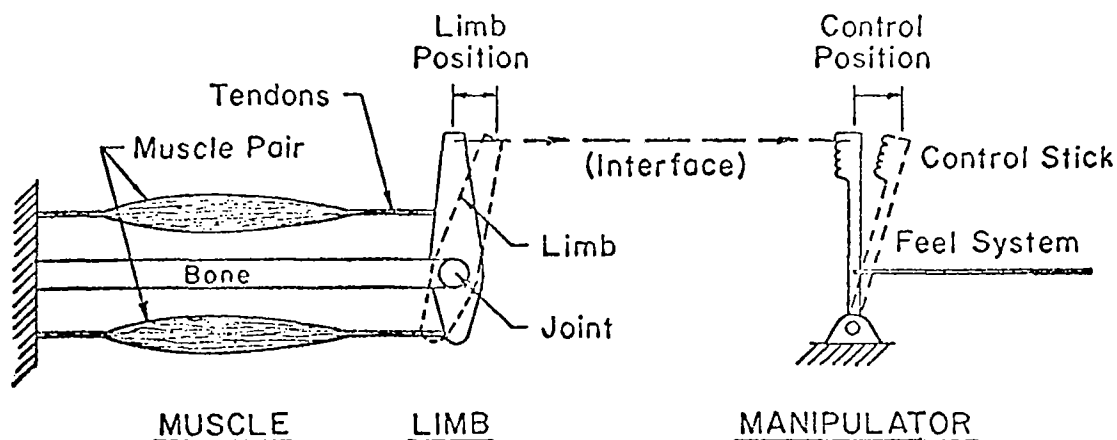


Figure 4. Idealized Agonist/Antagonist Muscle Pair

Figure 5 shows the functional diagram of the agonist/antagonist muscles. This diagram (taken from Ref. 1) shows the manipulator, peripheral sensing elements, peripheral muscle elements spinal cord region and supraspinal command paths. Reference 1 contains a detailed discussion of the elements in Fig. 5—our interest here is in the major interactions of these elements in tracking tasks. Looking at the lower half of this diagram note that the manipulator responds to

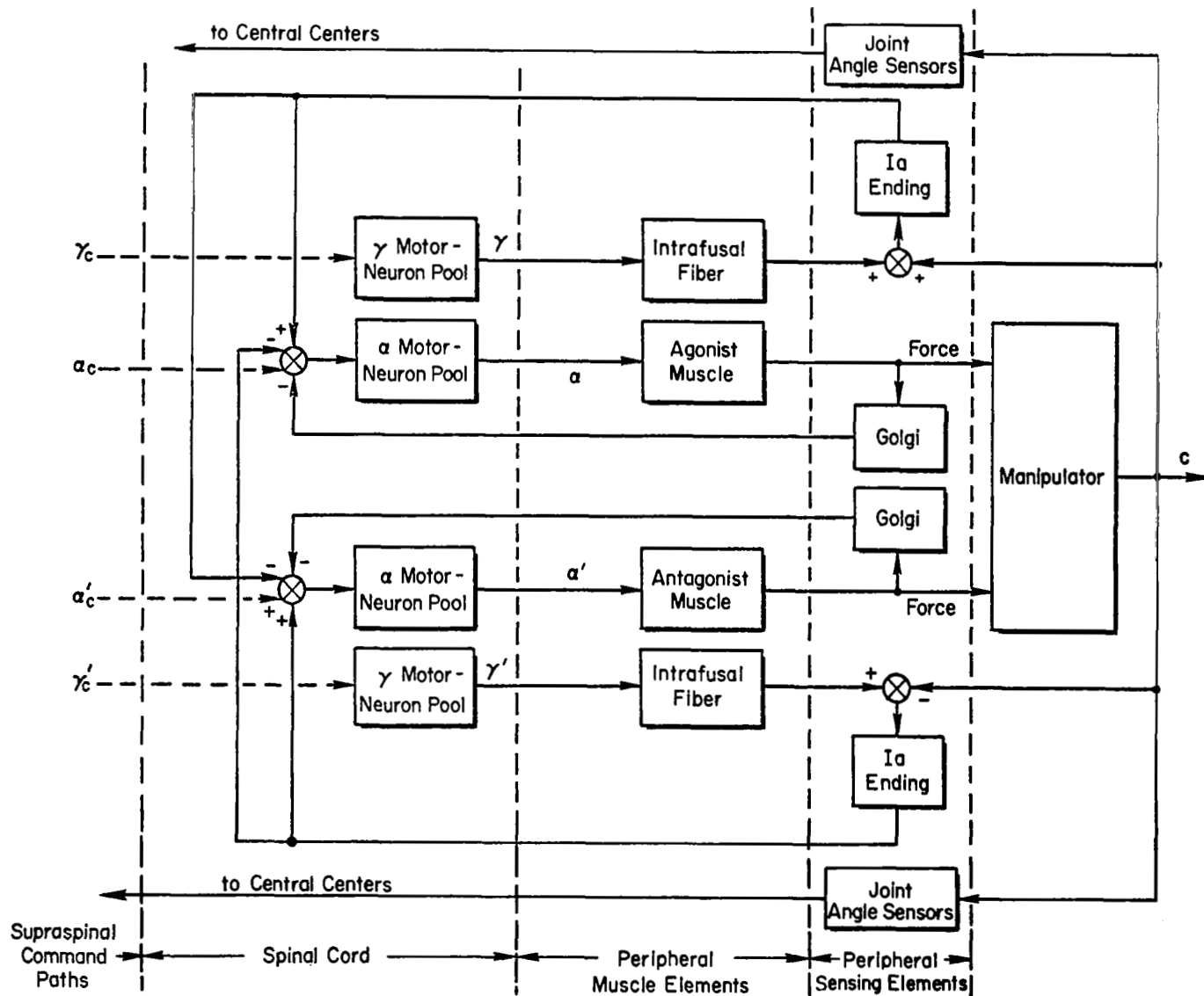


Figure 5. Functional Diagram of Agonist/Antagonist Neuromuscular System Elements Involved in Tracking

the force exerted by the antagonist muscle which responds to nerve firing rate stimulation arising from the α motor neuron pool located in the spinal cord. This in turn receives a variety of feedback, crossfeed and command signals.

The muscle spindle feedback signal arises from the I_a ending and makes a monosynaptic connection (Ref. 12) to the α motor neuron pool such that increased I_a firing rate causes α' to increase (hence the plus sign at the summing junction). The I_a ending produces an increased firing rate due to either a pull on the muscle (lengthening) or increased pull from the intrafusal fiber. The intrafusal fiber (many of which are buried within a muscle) is a small muscle system. It receives stimulation from the γ motor neuron pool which responds to commands, γ'_c . The muscle spindle functions as a negative feedback loop on muscle length in spite of the plus sign at the summing junction. The minus sign around the loop occurs in the muscle since an increase in α' produces increased force but a decrease in muscle length. Note also the crossfeed of spindle output over to the agonist muscle but with negative polarity. This aids the agonist/antagonist muscles in seesawing about the operating point.

The Golgi feedback senses muscle force and makes a disynaptic connection (Ref. 12) to the α motor neuron pool such that increased Golgi output will cause α' to decrease. This produces a negative feedback loop on muscle tension since increased α' produces increased muscle force which produces increased Golgi output. Note that this feedback can function as a protective device. Consider a large external force suddenly applied to a muscle already tense. The force increase produces increased Golgi output which reflexly causes a reduction of excitation to the alpha motor neuron pool. However this viewpoint has been reexamined (Refs. 14, 15). Quoting Ref. 15 on the role of the Golgi:

This reflex system has usually been regarded as a safety device which protects a muscle from overloads and consequent damage. Many tendon organs have a rather high threshold to passive stretch as Matthews (Ref. 16) demonstrated. For this reason it was believed that only when the tension in a muscle became very large would the tendon organs fire and reflexly inhibit the motor neurons. Recent evidence, however, indicates that, unlike the situation in passive

stretch, the tendon organs are very sensitive to the tensions produced by active contractions of the muscle (Refs. 14, 25). This finding suggests that the tendon organ does not function primarily as a protective mechanism against overloads, but, rather, that it is the transducer in a continuous feedback system which regulates muscle tension, just as the spindle receptor is the transducer in the system which regulates muscle length.

The joint position sensors (Ref. 13) sense absolute limb position and send this information to higher centers (principally the thalamus) such that a very fine sense of position is available. The muscle spindles sense local position since their operating point is subject to higher control via bias signals in the γ pathways. Finally the Golgi's sense muscle force. Thus there is a rich variety of feedback sensors to aid the muscles in contending with load dynamics.

1. Simplified Describing Function Model for Neuromuscular System

Although the details of the human operator's actuation system for even the simplest of motions are enormously complicated from a component standpoint, the actions of the overall system can still be modeled simply if component ensembles are used. The connections between these ensembles will depend greatly on the type of motions involved. Here we are concerned primarily with neuromuscular system operations in which the command inputs are random and the motion outputs are exerted on spring-restrained low-inertia manipulators. Thus both the agonist and antagonist muscles will be active in setting up the operating point muscle tension in each muscle around which perturbations take place during the tracking task.

The block diagram of Fig. 6 shows the effective describing functions for the perturbation operations about steady-state operating points for the muscles and spindle elements and the joint feedbacks to higher centers (the role of the Golgi's, not shown in Fig. 6, will be discussed shortly).

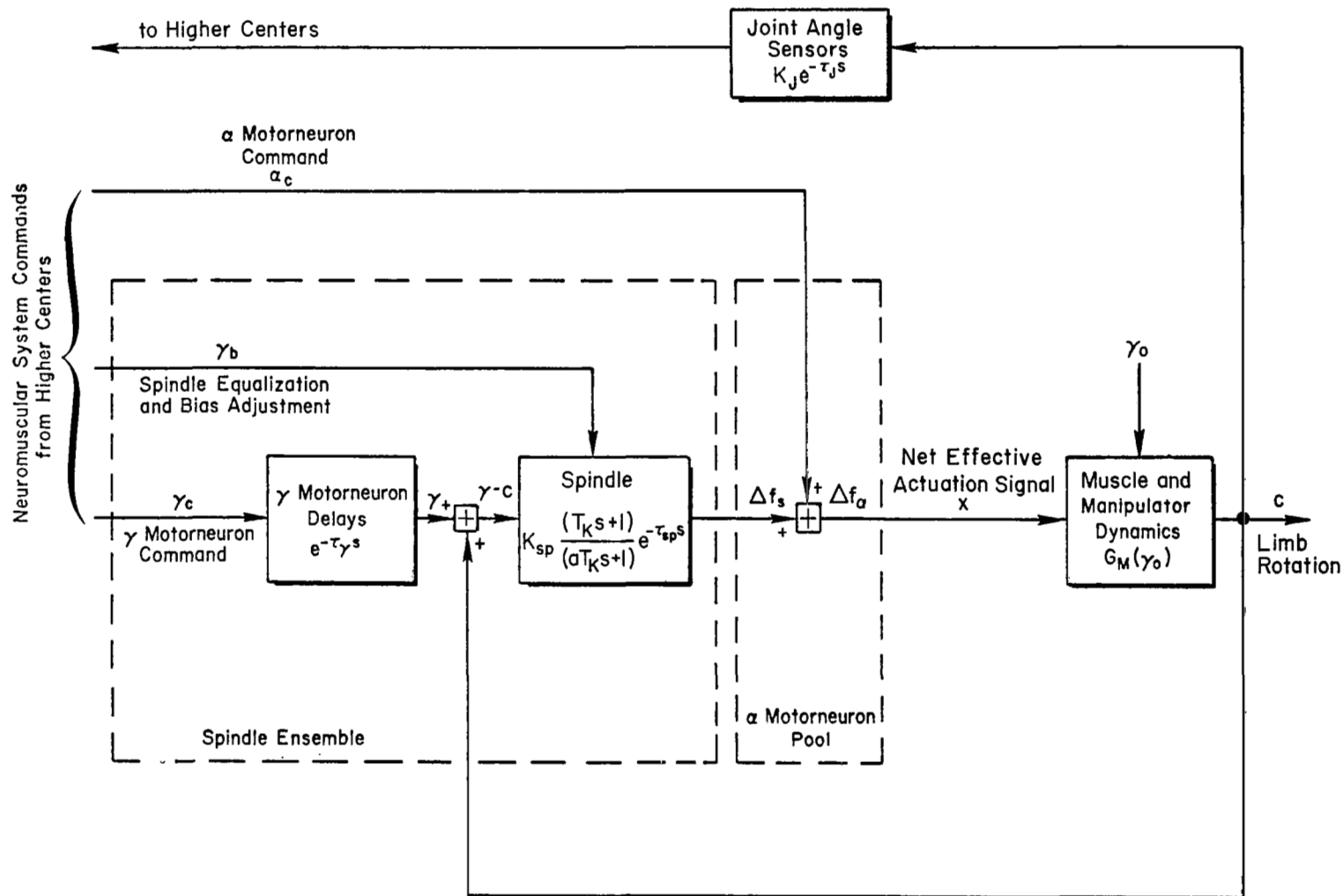


Figure 6. Simplified Neuromuscular System Model

The spindle ensemble provides in one entity (1) the feedback of c ; (2) some series equalization, $K_{sp}(T_K s + 1)/(aT_K s + 1)$; (3) the source of one command to the system, γ_c ; and (4) a signal, γ_p , for adjustment of the spindle equalization, gain, and steady-state output, γ_o [the latter sets up the operating point conditions for $G_m(\gamma_o)$]. The spindle output differential firing rate, Δf_s , is summed with an alpha motor neuron command, α_c , resulting in an incremental alpha motor neuron firing rate, Δf_α . This in turn operates the muscles and manipulators, giving rise to the limb rotation which is then sensed by the spindle ensemble. The spindle lag is a high-frequency effect, i.e., $a \ll 1$, while the lead is the dominant part of the loop equalization. The γ motor neuron command provides one means of actuating the neuromuscular system. For inputs requiring faster signal processing, the α motor neuron command from higher centers provides the dominant signal to the neuromuscular system. As shown in Fig. 6, this is a second way to actuate the neuromuscular system.

The describing function for the Golgi ensemble can be interpreted from transient response data in Ref. 14. Examination of this data for the Golgi response to force reveals that the amplitude and phase increase with frequency but not as much as for the spindle describing function. However for any particular operating point condition a lead-lag term can approximate the net effect of both the spindle and the Golgi ensemble over the mid- and high-frequency regions. Thus in Fig. 6 the spindle describing function serves to account for both these feedbacks as they affect the output of the α motor neuron pool. This simplified account of these feedbacks will be adequate to describe the closed-loop neuromuscular response if the α motor neuron command, α_c , is the basic command input and the gamma system inputs merely set up operating point conditions. If the γ motor neuron command, γ_c , is the basic command input then a separate block for the Golgi describing function should be used. However in later sections of this report we shall assume that the α motor neuron command is the command input and thus the spindle block is meant to subsume both spindle and Golgi feedback describing functions.

The joint angle sensors describing function can be inferred from transient response data in Ref. 13. This data indicate that this response is also lead-lag but at very low frequencies such that at mid- and high-frequencies (the region of interest) a gain and time delay is the appropriate description.

In Ref. 1 the model in Fig. 6 was used to explain some trends in the whole human describing function phase characteristics. Assuming that the spindle lead as well as a real pole from G_m appear at low frequency it was shown that an increase in the average muscle tension causes a shift in the phase umbrella (Fig. 2) to the right; that is, the effective time delay, τ_e , decreases and the low frequency parameter, α , increases. Direct measurement of G_m will validate or provide a basis for modification of these assumptions.

This section has reviewed data and models indicative of neuromuscular system effects. At this point we must note some caveats:

- a. A high-frequency peak in the human operator describing function has not always been well defined (or perhaps not within the data band) for second-order controlled elements where low frequency lead is required. The second-order subcritical task cases in Ref. 10 suffered from data scatter. This situation has been rectified now with the experiments reported in Ref. 11, where revised forcing function shapes plus more precise measurement equipment has produced low variability data. This same equipment was used for some key experiments in this report, with similar quality data resulting.
- b. That the high-frequency peak is due to some aspect of the neuromuscular system has always seemed to be a reasonable assumption but has never been directly validated in a tracking situation.
- c. It is not clear if other limb-manipulator combinations (e.g., rudder pedals) have similar dynamics as that for hand manipulators.

The above considerations plus the ability to obtain direct measurements of muscle/manipulator dynamics led to the following purposes.

D. PURPOSES AND OUTLINE OF REPORT

The general purpose of the experiments described later is to obtain describing function data for the muscle/manipulator actuation element, G_m , and the whole human, Y_p , for two manipulator types (hand manipulator and rudder pedals). The specific purposes (within categories) are:

Muscle-Manipulator Dynamics

1. Via direct measurement determine the muscle-manipulator dynamics while tracking. This will provide a basis for selecting model parameters for other restraints including control stick nonlinearities.
2. Determine these dynamics for other limb groups.
3. To determine if these dynamics are task dependent; specifically, do they change for controlled elements where low-frequency lead equalization is required.

Human Operator Dynamics

1. To relate closed-loop neuromuscular system properties to the high-frequency peaks often observed.
2. To validate that in tracking tasks the pilot's effective time delay decreases when the average tension in the muscle increases.
3. To find the effects of different limb groups on the pilot's describing function, e.g., legs versus hands.
4. To determine the role of the neuromuscular system for controlled elements requiring low-frequency lead equalization.

To achieve these purposes experimental data form the core of this report. Section II describes the experimental single-loop control situation and the processing methods on the EMG signal used to get direct measurements of the neuromuscular system's involvement in tracking operation. The matrix of experiments selected to investigate both rudder pedal and hand manipulator is presented, and the specialized equipment used is also described

in Section II. In Section III we present some selected data comparisons for both rudder pedal and hand manipulators which illustrate the effects on the pilot's describing function as well as direct measurements of the neuromuscular system describing function. Finally, Section IV presents our data interpretation and precise curve fits from which we infer conclusions as to the specific purposes discussed in the previous paragraph. These conclusions are summarized in Section V.

SECTION II

EXPERIMENTAL PLAN, APPARATUS AND MEASUREMENT TECHNIQUES

This section describes the experimental single-loop control situation and the processing methods on the EMG signals used to get direct measurements of the neuromuscular system's involvement in tracking operations to fulfill the purposes discussed at the end of the last section. The matrix of experiments selected to investigate both rudder pedal and hand manipulator is presented, and the specialized equipment used is also described.

In aircraft applications hand manipulators are generally more demanding than leg manipulators. However a rudder pedal manipulator was used initially. This manipulator has a special advantage for experimental purposes, namely, that the agonist and antagonist muscles (Fig. 4) are inherently a balanced set in terms of function and geometry. This proved useful in validating the EMG signal processing, interpretation and subsequent development of digital data reduction procedures. Then the bulk of the experiments were carried out using a hand manipulator.

Figure 7 shows the general arrangement of the specialized equipment used to measure the human operator's performance in controlling the single-loop compensatory situation. The forcing function, i , error, e , human operator output, c , and system output, m , are shown scaled in centimeters of display deflection. How this is done will be subsequently discussed. The forcing function i is a sum of sine waves as indicated by the sine wave generator. Within the human operator block is shown the muscle manipulator actuation dynamics, G_m , and its effective input, x . If x and c are available then G_m can be computed even though x may be a complicated result of the net feedback signal and the displayed error. A measure of the signal x is obtained from the EMG electrodes which then go into the EMG sensing and signal conditioning block. The output is an estimate of x as well as a measure of the average tension. In addition the various processed EMG signals are sent to an FM recorder along with i , e , c , and m . In the lower part of Fig. 7 is shown an on-line Fourier coefficient analyzer operating off of i , e , and c .

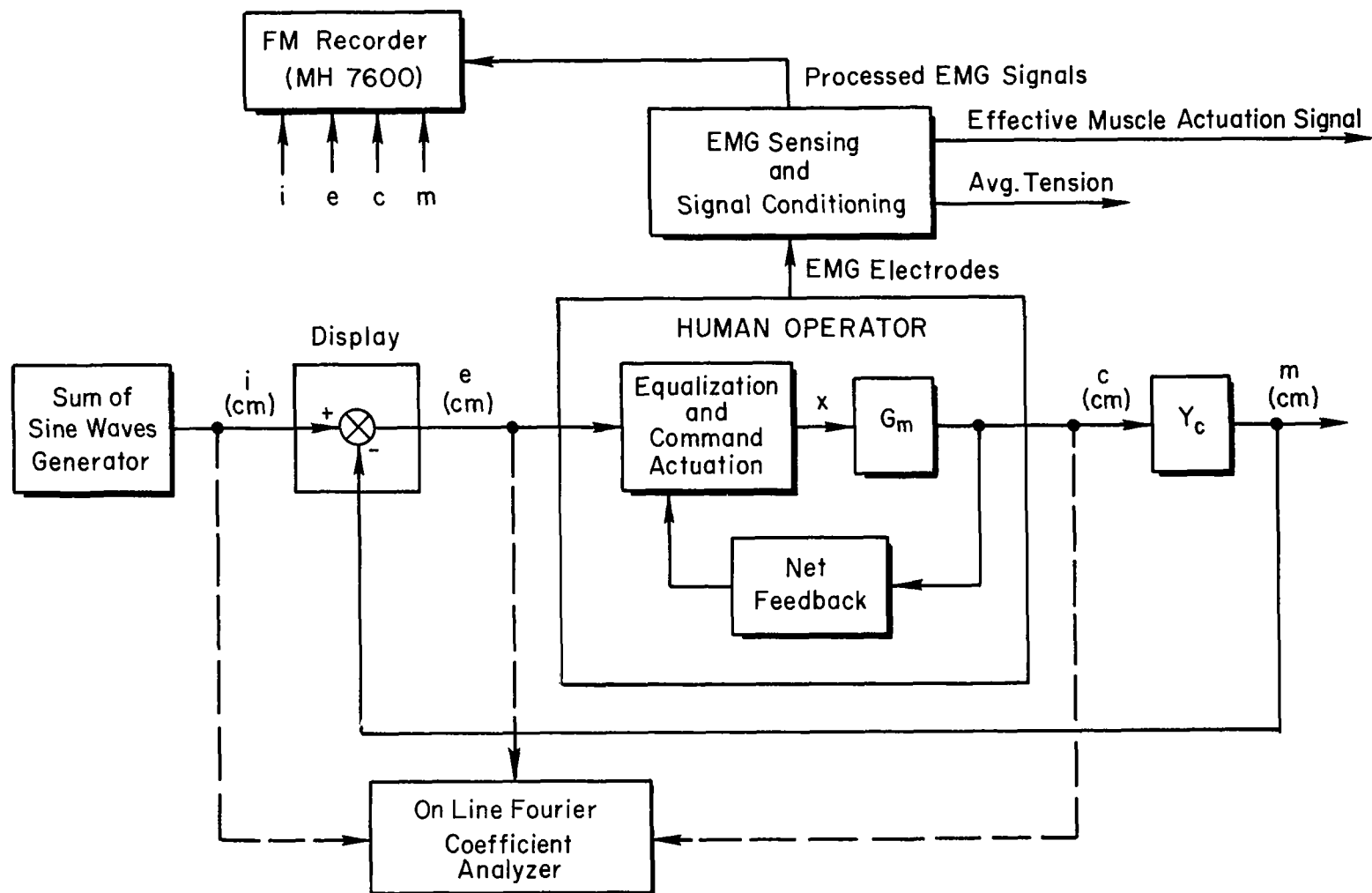


Figure 7. General Arrangement of Equipment

The remainder of this section discusses the details of the experimental equipment which was generally different for the rudder pedal and hand manipulator experiments. The matrix of experiments is discussed next, followed by the details of the muscle groups used for each manipulator. The EMG sensing and signal conditioning is then discussed followed by the rudder pedal and hand manipulator feel system characteristics and control sensitivities. The forcing functions and their intimate relationships to the data reduction procedures are next discussed for both sets of experiments as well as the digital data reduction methods used. Finally this section concludes with a brief biography of the subjects used.

A. MATRIX OF EXPERIMENTS

Table I shows the matrix of experiments for the two manipulator types (rudder pedals and hand manipulator) as well as tie-in configurations with Ref. 11. The three controlled elements shown in Table I are first-, second-, and third-order subcritical tasks designated respectively Y_{c1} , Y_{c2} , and Y_{c3} . Under each manipulator configuration are shown values of the λ_1 , λ_2 , or λ_3 that were used as well as ω_1 , the forcing function bandwidth.

The rudder pedal experiments were performed first. After a series of preliminary experiments, three values of λ_1 were selected. The purpose was to induce a tension increase with increasing λ_1 so as to investigate the effects of average tension in the muscles while tracking on the pilot's overall describing function. The hand manipulator, rather than the rudder pedal, was used with all three controlled elements. Briefly, the reason was that these experiments used the more precise and versatile Ref. 11 equipment to simulate the controlled element, form the forcing functions and perform the on-line data reduction for getting describing functions to aid in configuration selection and also guide the final digital data reduction. As indicated in Table I the Ref. 11 experiments are the tie-in configurations.

TABLE I
MATRIX OF EXPERIMENTS

| CONTROLLED ELEMENT | MANIPULATOR | | TIE-IN CONFIGURATIONS (REF. 11) (HAND MANIPULATOR ONLY) |
|--|--|--|---|
| | RUDDER PEDALS | HAND | |
| $Y_{c1} = \frac{K_c^*}{s - \lambda_1}$ | $\lambda_1 = 0.25, 1, 2$ $\omega_1 = 1.2$ | $\lambda_1 = 1, 2, 3$ $\omega_1 = 2$ | $\lambda_1 = 2$ $\omega_1 = 2$ |
| $Y_{c2} = \frac{\lambda_2}{s(s - \lambda_2)}$ | | $\lambda_2 = 0.5, 2$ $\omega_1 = 1$ ($\omega_1 = 2$ for one run with $\lambda_2 = 2$) | $\lambda_2 = 1.25$ $\omega_1 = 1.25$ |
| $Y_{c3} = \frac{\lambda_3}{s^2(s - \lambda_3)}$ | | $\lambda_3 = 0.3$ $\omega_1 = 0.3$ | $\lambda_3 = 0.3$ $\omega_1 = 0.3$ |
| * $K_c = 1.5$ for rudder pedals; otherwise $K_c = \lambda_1$. Two runs per configuration. | | | |

B. RUDDER PEDAL MUSCLE GROUPS

The rudder pedal tracking apparatus, Fig. 8, requires motion of the leg about the hip and knee to produce the horizontal motion as shown in the idealized diagram in Fig. 9.

The spring restraint resists the push indicated by the "line of motion" (Fig. 9) and thus requires both leg and thigh extension. Extension of the leg (rotation about the knee joint) is performed by the quadriceps (Ref. 17), i.e., Rectus femoris, Vastus lateralis, Vastus medialis and Vastus intermedius (Fig. 10 taken from Ref. 17). The largest and most active is the Vastus lateralis on which the EMG electrodes were placed (Fig. 10). Although the Rectus femoris is part of this group it may flex the thigh when the muscle is acting as an extensor at the knee (Ref. 17). Other primary thigh flexors include the Tensor fasciae and the Sartorius.

Flexion of the leg is performed by the posterior femoral muscles (hamstrings) the most prominent of which is the Bicep femoris. This muscle group is not involved in the task since the pedal has no rearward force constraint. From



Figure 8. Subject Using Rudder Pedals and EMG Electrodes

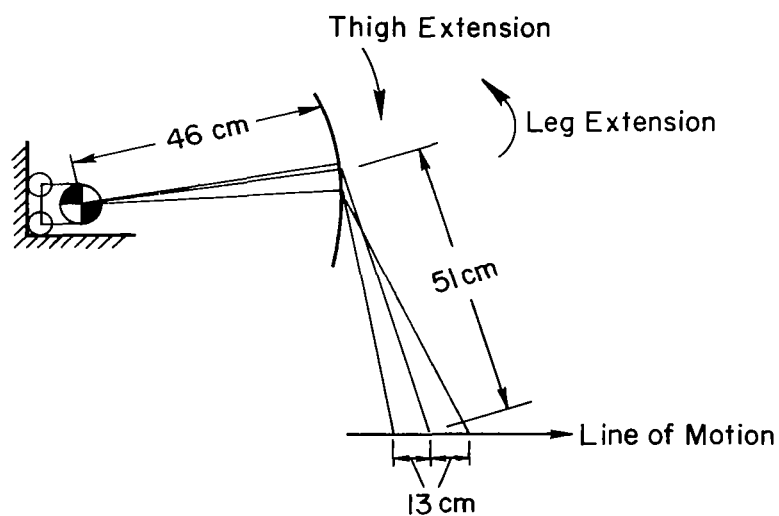


Figure 9. Thigh and Leg Geometry for ± 13 cm Movement

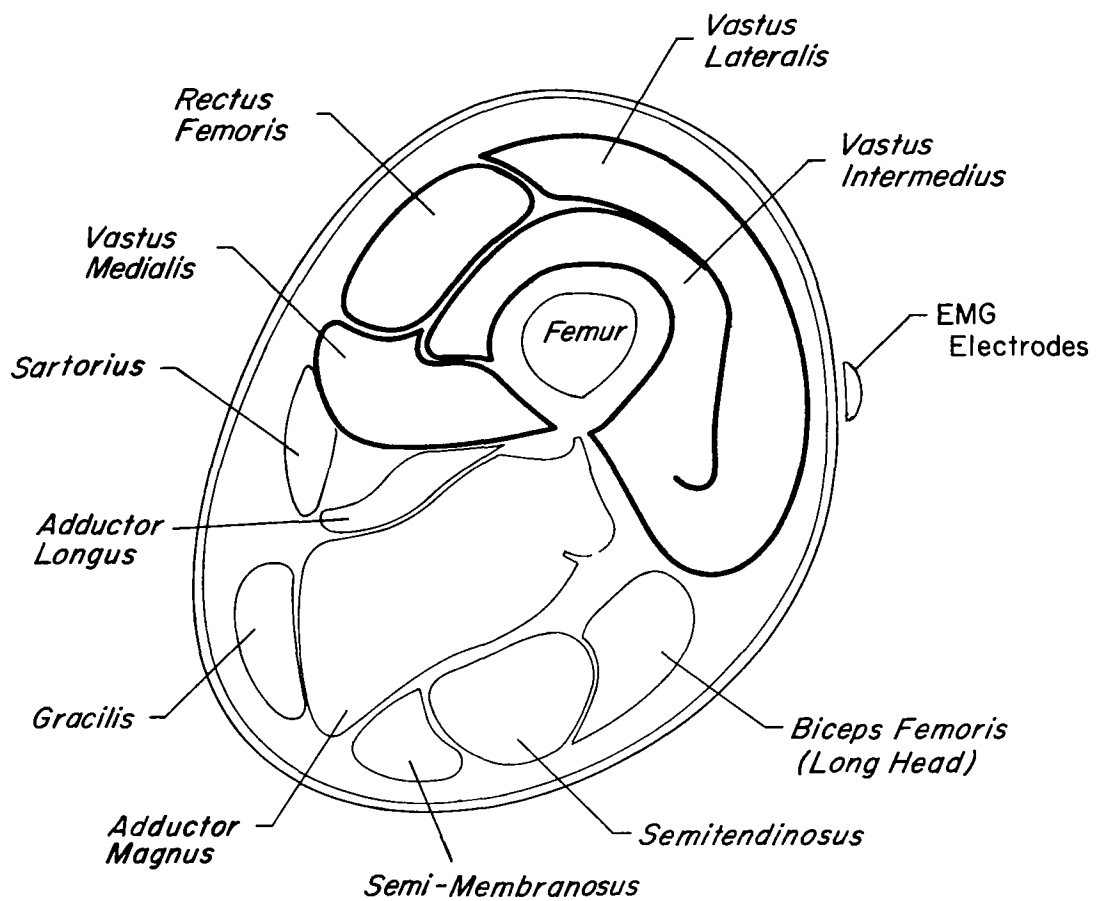
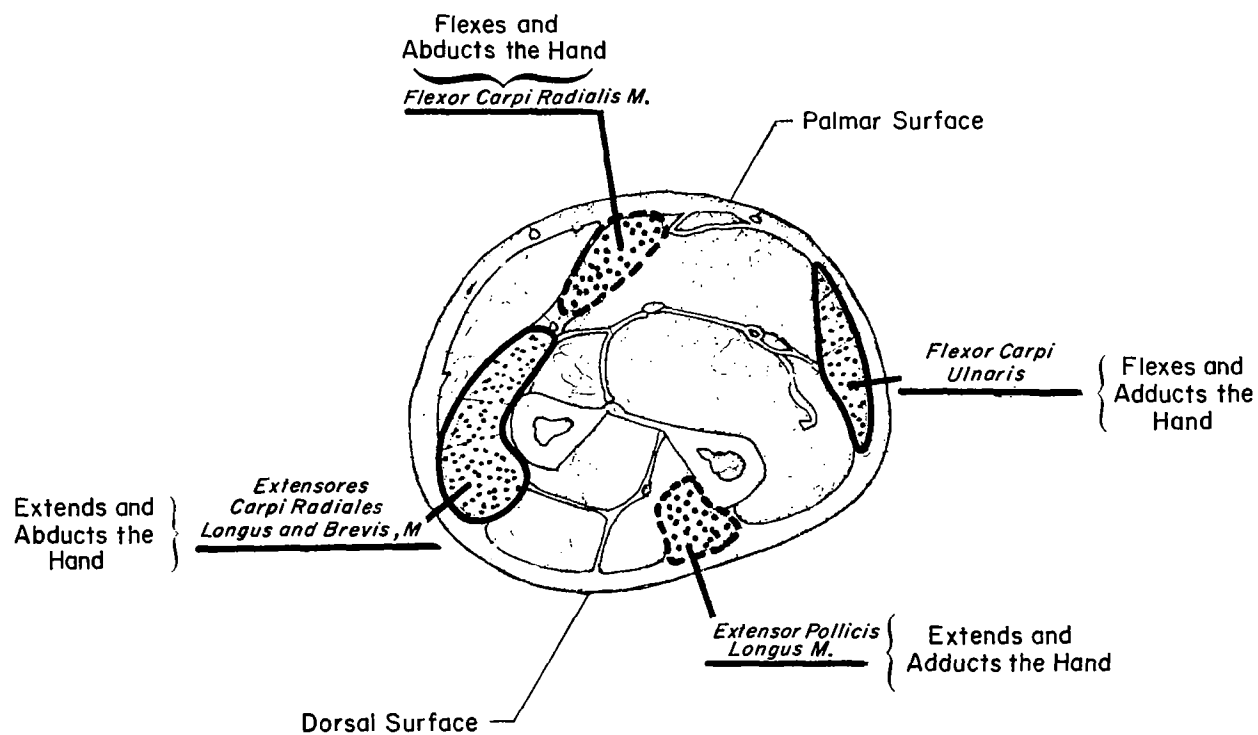


Figure 10. Cross Section Through the Middle of the Thigh
Looking Toward the Body. Four-fifths
of Natural Size.

the photo of the subject seated in the tracking position it can be seen that there is nearly a right angle between the thigh and lower leg. Since the pedals only move horizontally any downward force would have only a small horizontal component. That the primary muscle used is the leg extensor was verified by taking an EMG of the Gluteus maximus muscle (thigh extension) in which no significant activity was observed while tracking yet the Vastus lateralis was quite active. Thus the Vastus lateralis was the dominant muscle and the agonist/antagonist pair consisted of this muscle located in opposite thighs.

C. HAND MANIPULATOR MUSCLE GROUPS

The hand manipulator (isometric) was actuated in the vertical plane. The subject grips the manipulator between the thumb and the forefinger (using the first two fingers) with the forearm resting on special splints in a horizontal position with the wrist axis inclined from the vertical approximately 45 deg towards the body. In this situation, lifting the manipulator requires extension of the hand and abduction about the wrist joint. Figure 11 shows a cross section of the right forearm looking towards the body and illustrates the location of the muscles involved in this tracking task as well as their function. (This figure is taken from Ref. 17.) The two muscles in heavy outline (the Extensor carpi radialis longus and the Flexor carpi ulnaris) are the primary agonist-antagonist muscles. (Note that lifting the manipulator involves both functions of the Extensor carpi radialis.) The two muscles shown in dotted outline, the Flexor carpi radialis and the Extensor carpi ulnaris are also involved in this tracking task but they have mixed effects, e.g., lifting the manipulator involves the former because of hand abduction and the latter because of hand extension. The Extensor carpi radialis longus and the Flexor carpi ulnaris were found to be the dominant agonist-antagonist pair. This was successful as far as the general function of the actuation elements involved in the task. However, the intermittent participation of the muscles shown in dotted outline in Fig. 11 during some of the static calibration tests somewhat clouded the results (at least as far as the absolute magnitude of the force contributed to the task is concerned). However, the phasing or timing of the dominant muscles participation in



Cross Section of the Right Forearm Looking Towards the Body
(Adapted from Gray's Anatomy, 1966)

Figure 11. Primary Wrist-Manipulator Actuation Muscles

the task is still valid and the data presented in the next section will be concerned with this aspect of the NM system.

D. EMG SIGNAL CONDITIONING

Figure 12 illustrates the procedure for processing the EMG signals obtained from surface electrodes from an agonist and an antagonist muscle. In tracking tasks with random-appearing inputs each muscle typically executes moderate tension excursions about an average tension level. In Fig. 12 the objective is to obtain two analog signals; one proportional to the average firing rate that produced the average tension level and the other proportional to the perturbation firing rate about the average. The latter is the effective perturbation input, $x(t)$, to the muscle-load combination (Fig. 1). The electrical activity picked

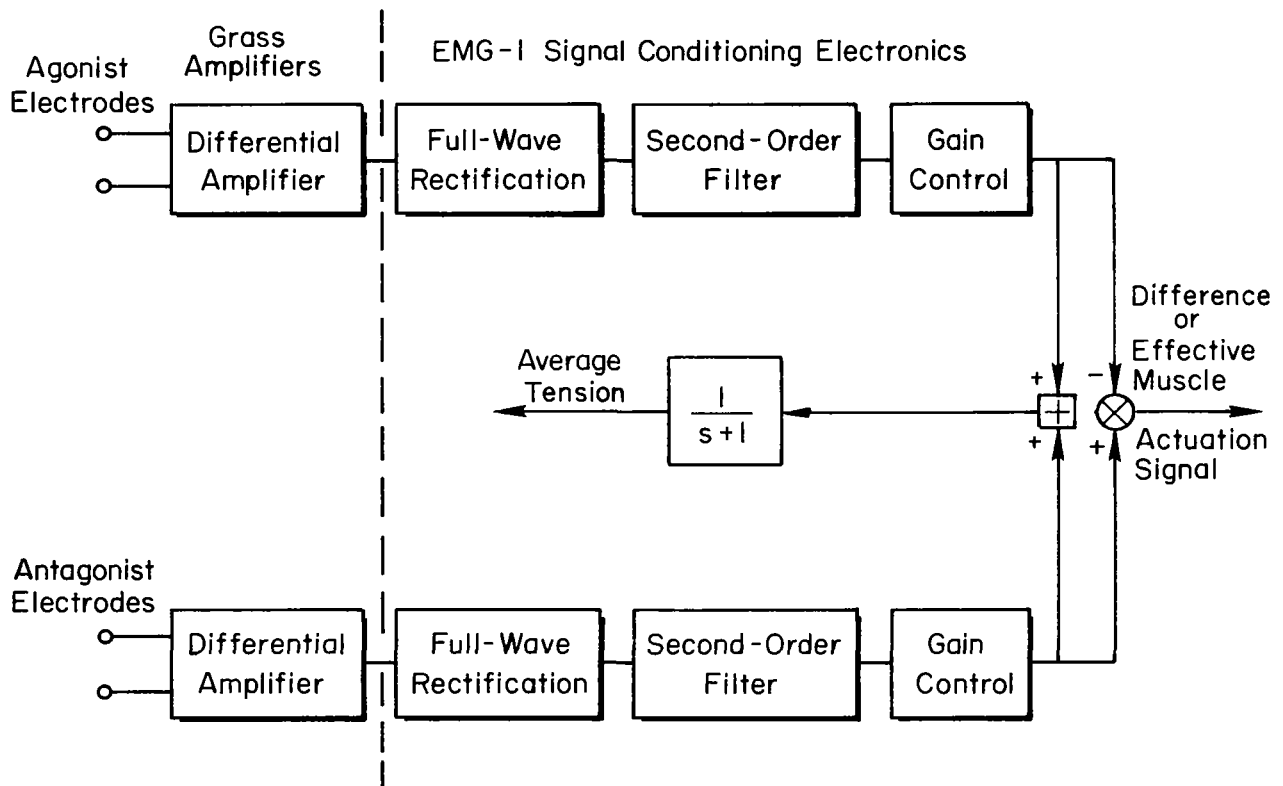


Figure 12. Muscle Action Potential (EMG) Processing to Obtain Effective Muscle Actuation Signal and Average Tension

up by the electrodes is representative of that from a moderate volume of muscle (containing many motor units, each of which contains many muscle fibers).

To describe the general process, consider one motor unit. When excited by a signal from an α motor neuron this fiber discharges, producing a bipolar voltage pulse a few milliseconds in duration. Under isometric conditions a steady firing rate produces a steady chain of pulses, which, in turn, cause tension in the muscle fibers associated with the particular motor unit. This tension increases as firing rate increases, with an approximately linear relation holding below tetanus. The voltage pulses recorded by the electrodes are essentially constant in amplitude and shape. Consequently an analog signal proportional to firing frequency can be obtained by full wave rectifying the pulses and then low-pass filtering with a time constant which is long relative to the interpulse interval. (The undamped natural frequency of the second-order filter shown in Fig. 12 is adjustable between 10 and 100 rad/sec, with a range of damping ratios.) Finally note that the analog signal can "track" a time-varying firing rate if the bandwidth of these time variations is small relative to the bandwidth of the second-order filter.

There is additional "smoothing" in that the electrodes are sensing a number of motor units and most of these will be active but each with a different firing rate. This amounts to an ensemble averaging across many motor units. Thus increased tension can be produced by increasing the firing rate of one motor unit or by recruiting additional units, with either case or the combination yielding an increased output from the full wave rectifier.

In Fig. 12 the gain control is used to compensate for different muscle action potential magnitudes (due to differences in muscle functional leverage and/or electrode placement) so that the two signals have the same average value before the difference is taken to yield the effective muscle actuation signal. For the rudder pedal experiments the agonist muscle (Vastus lateralis) is the same as the antagonist muscle but in the opposite leg. This simplifies electrode placement for equal signal strength and gain scaling. The second-order filters in Fig. 12 were

set for a natural frequency of 31.4 rad/sec (5 Hz) and a damping ratio of 0.715 for the rudder pedal experiments. For the hand manipulator experiments the natural frequency was set at 100 rad/sec (\approx 16 Hz) and the damping ratio was 0.5.

The Grass amplifiers indicated in Fig. 12 were AC preamplifiers (Model P511-DR) plus high impedance probes (20,000 megohms input impedance!). The low-frequency filter setting was 10 Hz and the high-frequency rolloff was 1 KC for all experiments. The signal channel gains were in the range 20K to 100K with the larger values used for some of the nondominant muscles in the hand manipulator experiments.

Beckman Biopotential Skin electrodes, adhesive collar and Offner paste were used. These electrodes and paste combinations yield low impedance levels (\approx 300 Ω). Spacing was 3 cm center to center.

All equipment was grounded to the Grass amplifiers as was the subject via a mouth ground (tinned wire gripped in mouth). This plus a fine wire mesh screen room (1.4 mm spacing) resulted in very low noise levels.

Figure 13 illustrates the timing relations in a tracking run for $Y_c = K_c/(s-2)$. The first time history at the top shows the pedal position. The signal labeled difference is the effective muscle actuation signal in Fig. 12 [note this signal corresponds to the signal $x(t)$ in Fig. 1]. The signal labeled "Smoothed Difference" used a first-order lag at 15 rad/sec to remove some of the high frequency power in the Difference to facilitate a visual comparison with the pedal position. The last trace shows average tension (Fig. 12). The Smoothed Difference signal contains all the "lumps and bumps" that the pedal position is undergoing in this tracking task and at essentially the same time. Of course the true muscle activity precedes the pedal response and this is found by taking out the filtering dynamics in the data reduction process.

Figure 14 presents static calibration curves of average tension versus force for left and right legs measured one leg at a time. Each of these curves are generally linear over a large range. There is about 25-30 percent slope asymmetry between legs. In subsequent digital data reduction each rectified and filtered EMG signal was analyzed and gain corrected

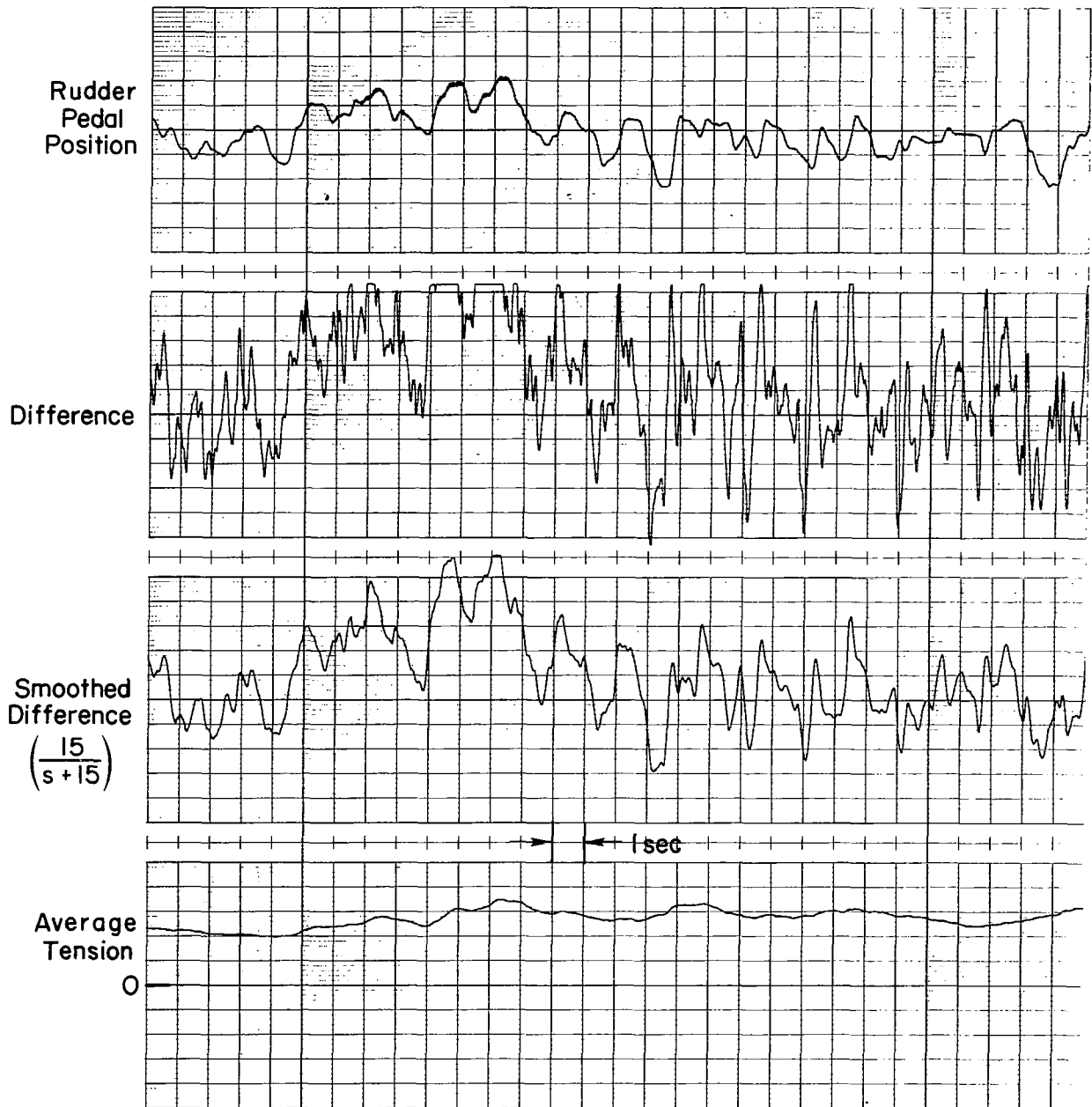


Figure 13. Example Time History for EMG Signal Processing;
 $Y_c = K_c/(s-2)$

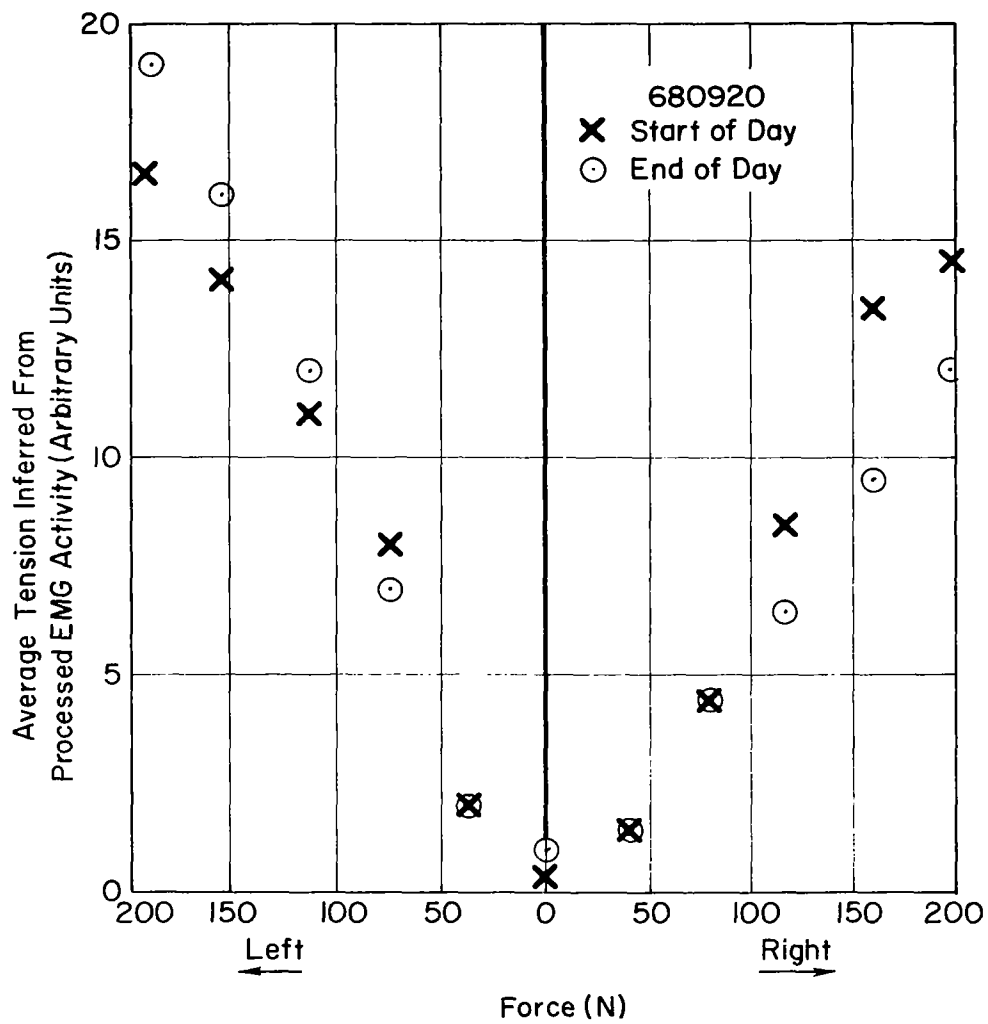


Figure 14. Average Tension Versus Force for Rudder Pedals

prior to taking the difference to obtain the effective muscle actuation signal shown in Fig. 12.

For the hand manipulator a limited number of runs were analyzed for each muscles participation in the task prior to taking the difference (details in Section III). The results show that the phasing is quite close in the agonist and antagonist muscles.

E. MANIPULATOR CHARACTERISTICS

The spring restrained rudder pedals effective characteristics at the center of foot pressure are:

| | |
|------------------|--|
| Spring rate | 108 N/cm |
| Mass | 0.87 kg — pedals alone |
| | 4.8 kg — pedals plus subject's legs taped to pedals |
| Coulomb friction | 7.5N |

The Coulomb friction was not noticeable to the subject as the rms control forces for the tracking tasks were greater than 25 newtons.

The rudder pedal sensitivity in controlling the task was 0.375 cm (scope) per cm (pedals). This is the sensitivity that would result if the controlled element (Fig. 7 and Table I) was a pure gain equal to one.

The hand manipulator was an isometric stick with following sensitivities of scope displacement in response to force for the three controlled element forms:

| | |
|----------|------------------------|
| 0.7 cm/N | First-order, Y_{c1} |
| 1.4 cm/N | Second-order, Y_{c2} |
| 3.5 cm/N | Third-order, Y_{c3} |

Again these are the sensitivities that would result if the controlled element were unity.

F. FORCING FUNCTIONS

The forcing function used for the rudder pedal experiments was a weighted sum of nine sine waves with a bandwidth of 1.2 rad/sec. A 100 sec run length was used. The relative scalings are:

TABLE II
RUDDER PEDAL FORCING FUNCTION

| CYCLES PER RUN LENGTH | ω (RAD/SEC) | SINE WAVE AMPLITUDE |
|--------------------------|--------------------|------------------------|
| 5 | 0.314 | 1 |
| 8 | 0.5 | 1 |
| 12 | 0.75 | 0.95 |
| 19 | 1.2 | 0.707 |
| 31 | 1.95 | 0.35 |
| 51 | 3.2 | 0.15 |
| 82 | 5.15 | 0.1 |
| 131 | 8.2 | 0.1 |
| 209 | 13.1 | 0.1 |

Here the last three frequencies represent a "shelf" so as to get high frequency measurements. The mean-square input as seen on the display was 1.65 cm^2 .

The forcing function spectra for the hand manipulator experiments were the sum of five sine waves as shown in Table III for the three controlled element forms.

G. DATA REDUCTION EQUIPMENT

The rudder pedal experiments used the Watthour Meter Analyzer (Ref. 6) to get on-line describing functions for Y_p and G_m to aid in configuration selection. These were computed from (see Fig. 7)

TABLE III
FORCING FUNCTION SPECTRA (HAND MANIPULATOR)

| CONTROLLED ELEMENT | | $Y_{c1} = \frac{\lambda_1}{s - \lambda_1}$ | $Y_{c2} = \frac{\lambda_2}{s(s - \lambda_2)}$ | $Y_{c3} = \frac{\lambda_3}{s^2(s - \lambda_3)}$ |
|--|------------------------|--|---|---|
| FORCING FUNCTION BANDWIDTH, ω_1 | | 2 | 1 | 0.3 |
| Frequency | Cycles per 100 sec run | Sine Wave Amplitudes* (cm) | | |
| $\omega_0 = 0.1884$ rad/sec | 3 | — | — | 0.666 |
| $\omega_1 = 0.502$ rad/sec | 8 | 0.494 | 0.612 | 0.236 |
| $\omega_2 = 1.256$ rad/sec | 20 | 0.460 | 0.342 | 0.0436 |
| $\omega_3 = 3.015$ rad/sec | 48 | 0.204 | 0.0708 | 0.0160 |
| $\omega_4 = 6.282$ rad/sec | 100 | 0.0543 | 0.0229 | 0.0143 |
| $\omega_5 = 10.46$ rad/sec | 166.67 | 0.0306 | 0.0166 | — |
| *Amplitudes scaled to give mean square = 0.25 cm^2 . | | | | |

$$Y_p = \frac{C}{E} \quad (5)$$

$$G_m = \frac{C}{X} \quad (6)$$

where C, E, and X are finite run length Fourier coefficients. The sine wave generator was the same as in Ref. 6 while the controlled element was simulated on an EAI 16-31R analog computer.

For the hand manipulator the experimental setup used was that used in Ref. 11. This equipment consists of a describing function analyzer (DFA) and Critical Task Tester consisting of a Controlled Element Computer (CEC) and display and isometric manipulator. With this setup on-line describing functions between the forcing function and the error is obtained from Fourier coefficients. Both the pilot and the total system describing function as well as the mean-square error and the relative correlated error are computed.

For both experimental configurations the formal data runs were recorded on a Honeywell 7600 14 track FM recorder. Subsequently digital data reduction was used to get the neuromuscular system describing function.

H. DIGITAL DATA REDUCTION

The describing functions Y_p and G_m were also calculated from ratios of cross-spectra from data digitized at 70 sps for the rudder pedal experiments and 60 sps for the hand manipulator experiments. The formulas used are:

$$Y_p = \frac{\Phi_{ic}}{\Phi_{ie}} \quad (7)$$

$$G_m = \frac{\Phi_{ic}}{\Phi_{ix}} \quad ; \quad \text{at forcing function frequencies} \quad (8)$$

$$G_m = \frac{\Phi_{xc}}{\Phi_{xx}} \quad ; \quad \text{at all frequencies, especially very high frequencies} \quad (9)$$

The Tukey method (Ref. 22) was implemented using the BOMM program (Ref. 24). The cross correlation is computed for a limited number of lags as

$$R_{xy}(\tau) = \frac{1}{T_R} \int_0^{T_R-\tau} x(t)y(t+\tau)dt \quad ; \quad |\tau| \leq T_m \quad (10)$$

where T_R = run length
 T_m = maximum lag time

The cross spectra is then computed as

$$\Phi_{xy}(j\omega) = \int_{-T_m}^{T_m} D(\tau)R_{xy}(\tau)e^{-j\omega\tau} d\tau \quad (11)$$

where the function $D(\tau)$ is selected so that the values of Φ_{xy} computed represent the power in a finite bandwidth about each value.

Two forms for $D(\tau)$ were used, Hanning for the rudder pedal experiments, and Parzen for the hand manipulator. These are:

Hanning

$$\begin{aligned} & \frac{1}{2} \left(1 + \frac{\cos \pi \tau}{T_m} \right) & ; & \quad |\tau| \leq T_m \\ & 0 & & \text{Otherwise} \end{aligned} \quad (12)$$

Parzen

$$\begin{aligned} & 1 - 6 \left(\frac{\tau}{T_m} \right)^2 + 6 \left| \frac{\tau}{T_m} \right|^3 & ; & \quad |\tau| \leq \frac{T_m}{2} \\ & 2 \left(1 - \left| \frac{\tau}{T_m} \right| \right)^3 & ; & \quad \frac{T_m}{2} \leq |\tau| \leq T_m \\ & 0 & ; & \quad \text{Otherwise} \end{aligned} \quad (13)$$

Subsequently the data reduction methods will be referred to as Tukey-Hanning or Tukey-Parzen. For Φ_{ic}/Φ_{ie} and Φ_{ic}/Φ_{ix} the value of T_m was 20 sec while for Φ_{xc}/Φ_{xx} the value of T_m was 2 sec.

For the Hanning window it can be shown that, in the frequency domain, its bandwidth is $2\pi/T_m$ rad/sec and that this is the bandwidth of each value of the cross spectra computed from Eq. 11. For the Parzen window the bandwidth is slightly larger.

The digital processing of the EMG signals for the hand manipulator was substantially the same as that for the rudder pedals described in Fig. 12. However since the hand manipulator muscles are not a balanced set the output of the second-order filters was processed to remove the mean and then normalized to unit variance. Then the difference between the agonist and antagonist signals is taken.

I. SUBJECTS

Both subjects had participated in current and earlier tracking tasks. WA (rudder pedal experiments) was a nonpilot with considerable previous experience in laboratory tracking tasks. RH (hand manipulator experiments) was a private pilot with commercial, instructor, and instrument ratings. He had some moving-base aircraft simulation experience and considerable previous laboratory tracking experience. He also participated in the Ref. 11 experiments.

SECTION III

EXPERIMENTAL DESCRIBING FUNCTION COMPARISONS — NEUROMUSCULAR SYSTEM AND WHOLE HUMAN

This section presents measurements of the pilot's overall describing function as well as the muscle/manipulator dynamics for both rudder pedal and hand manipulator experiments. Generally single run data are given since in nearly every instance repeat run scatter was very low. The rudder pedal data reveal the effects of average muscle tension while the hand manipulator experiments illustrate the effects of low frequency lead generation. The various measurement techniques and data processing methods (discussed in the previous section) are used to provide an extremely wide measurement bandwidth for the muscle/manipulator dynamics data.

A. RUDDER PEDAL DATA

As indicated in the previous section describing function measurements intended to emphasize neuromuscular system effects were taken with the rudder pedal manipulator operating the first-order subcritical task. Three different values of λ_1 were used, namely 0.25, 1 and 2. The measurements of the pilot's overall describing function Y_p are shown in Figs. 15 and 16. Figure 15 also compares describing functions obtained from Fourier coefficients (only three of the nine frequencies were analyzed) with that from the Tukey-Hanning method. As can be seen the agreement is quite good indicating that the larger effective bandwidth with the Tukey-Hanning method does not degrade the measurements. The data in this figure will be used further in a later comparison in the section on data interpretation. For now, note that the results are similar to those in Fig. 2 in the Introduction as well as those available in Refs. 9, 10, and 11. That is, the amplitude ratio consists of a flat midband gain region followed by a high frequency rise possibly indicating neuromuscular system modes, and the phase characteristic indicates an effective time delay as well as some low frequency droop.

Figure 16 shows a comparison with the two extreme values of the divergence mode used, $\lambda_1 = .25$ and 2. For the larger value the pilot increased his gain and decreased his effective time delay, as indicated

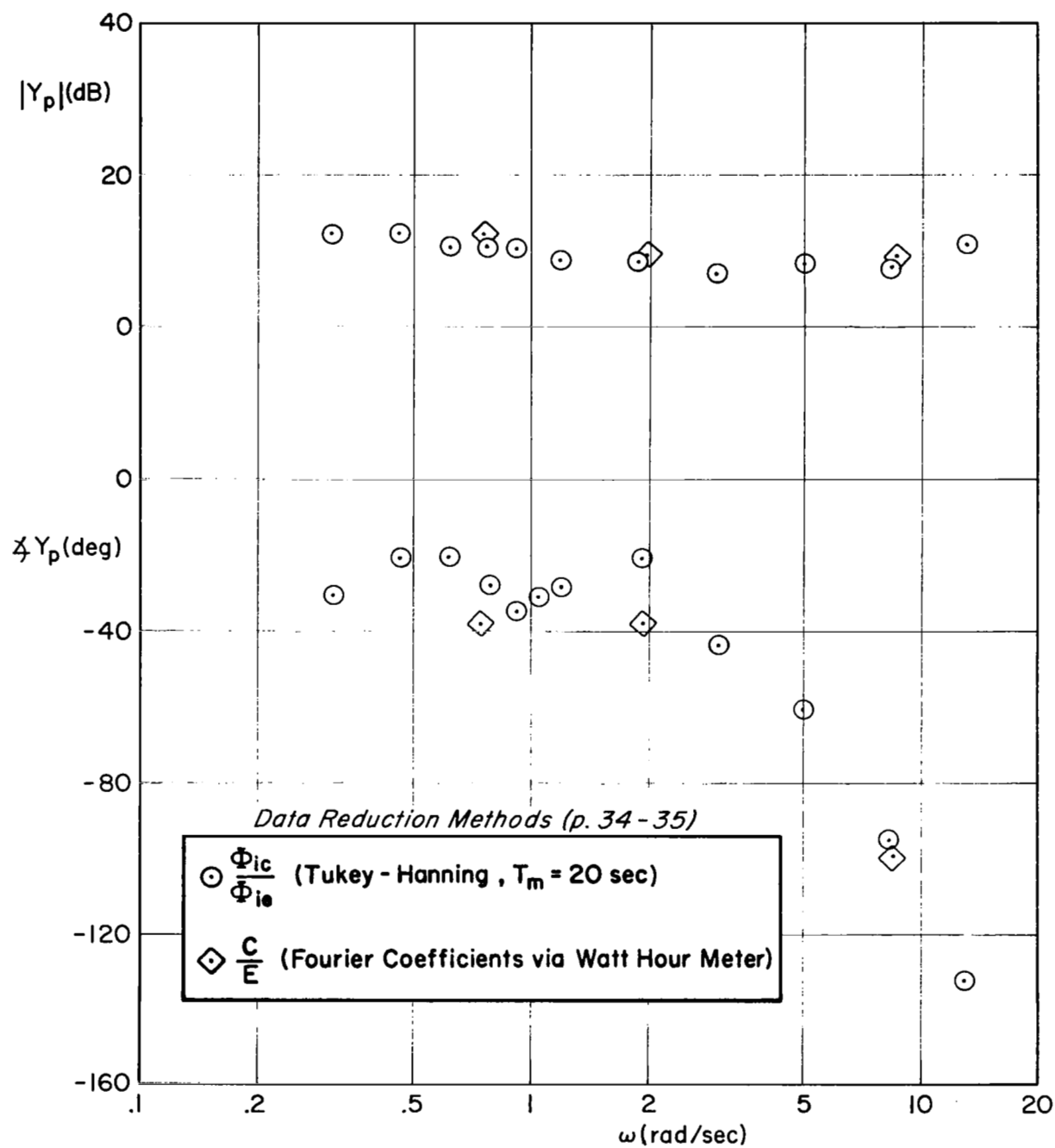


Figure 15. Human Operator Describing Function, Y_p ,
Rudder Pedals, $Y_{c1} = 1/(s-1)$

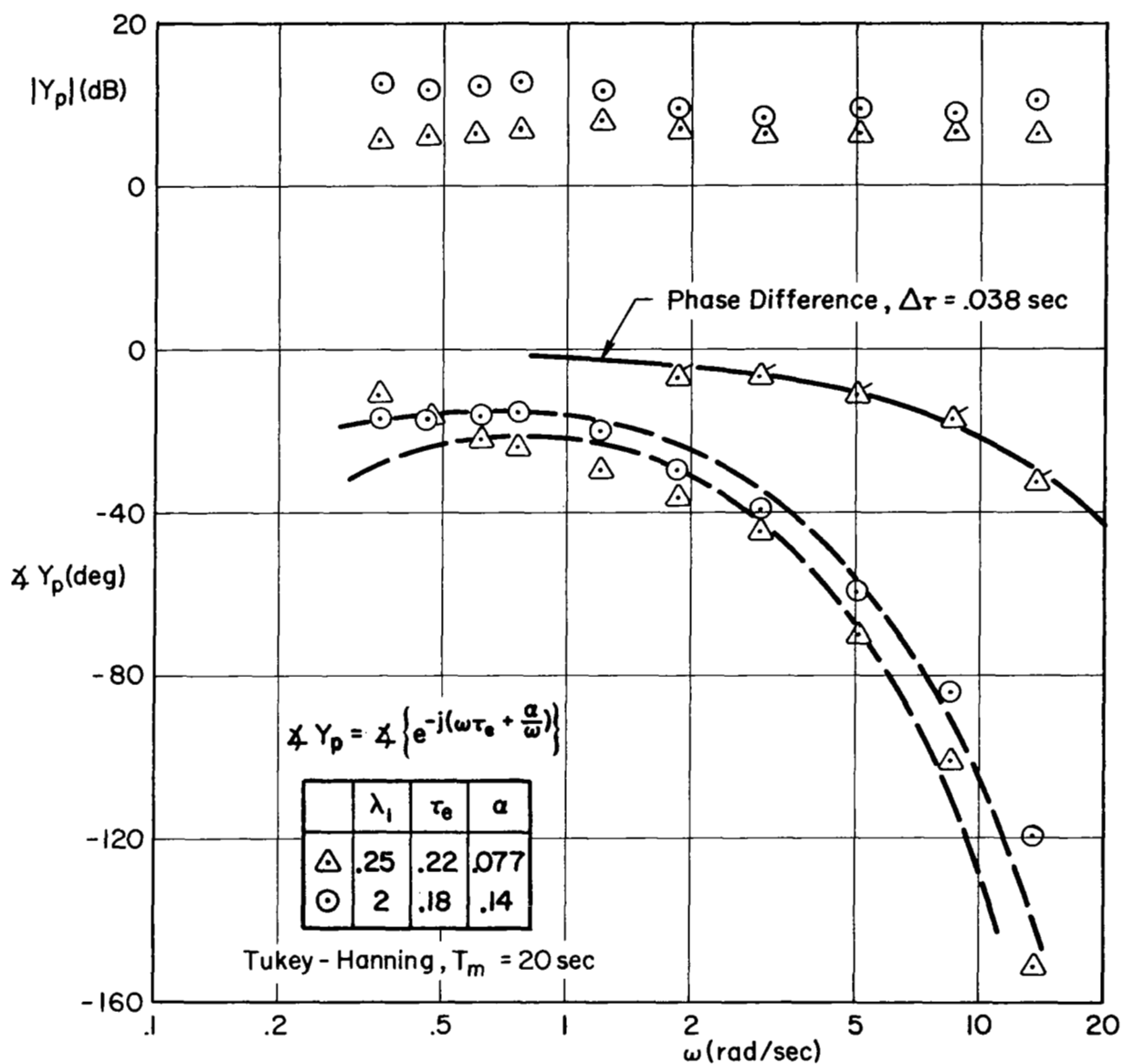


Figure 16. Effects of Controlled Element Divergence on the Human Operator Describing Function, Y_p , Rudder Pedals, $Y_{C1} = \lambda_1(s - \lambda_1)$, $\lambda_1 = 0.25$ and 2.0

by less high frequency phase lag. (The phase difference between these two curves is also shown plotted in Fig. 16.) As can be seen this phase difference implies a difference in effective time delay of about 38 milliseconds. Also shown with the phase data of Fig. 16 are approximate model fits involving both high and low frequency phase parameters, τ_e and α , from the form $Y_p = K_p e^{-j(\omega\tau_e + \alpha/\omega)}$. These approximate model curve fits are good fits in the crossover frequency region in the neighborhood of 3.5 to 5 rad/sec, although they do miss the highest frequency data points.

Some typical data for the portion of the effective neuromuscular actuation system denoted as G_M on Fig. 1 is shown in Figs. 17-19 for $\lambda_1 = .25, 1$, and 2 , respectively. Generally, all three are very similar in both amplitude and phase. Fig. 18 shows that the various measurement methods give essentially the same results at forcing function frequencies when the input, x , and output, c , of G_M is correlated against forcing function, i , or against x . These two methods give the same result in spite of a 10 to 1 difference in the effective measurement filter bandwidth. Finally, Figs. 18 and 19 present watt-hour meter measurements of the phase of G_M and these data points generally lie within the scatter of the Tukey-Hanning measurements.

The signal x also contains high frequency power which passes through G_M and is called "remnant" at c . Interpreting this remnant as a test signal into G_M power spectral density measurements of x were found to be fairly flat at high frequency, i.e., essentially white. Thus confidence interval limits can be calculated for these measurements. Fig. 18 shows, at some of the frequencies above 12 rad/sec, an indication of the 95 percent confidence limits calculated from n , the number of degrees of freedom, and the sample correlation coefficient ρ^2 (page 234, of Ref. 18). Generally, the data look quite reliable out to 30 rad/sec and reasonable out to 50 rad/sec thus validating the use of remnant as a test signal at high frequencies beyond the forcing function frequencies.

Fig. 18 also illustrates a curve fit, in this case third order dynamics and a pure time delay. Here the complex second order dynamics occur at 11 rad/sec with a damping ratio of 0.8. There is also a real root at 40 rad/sec and about 7 milliseconds time delay. This curve gives an

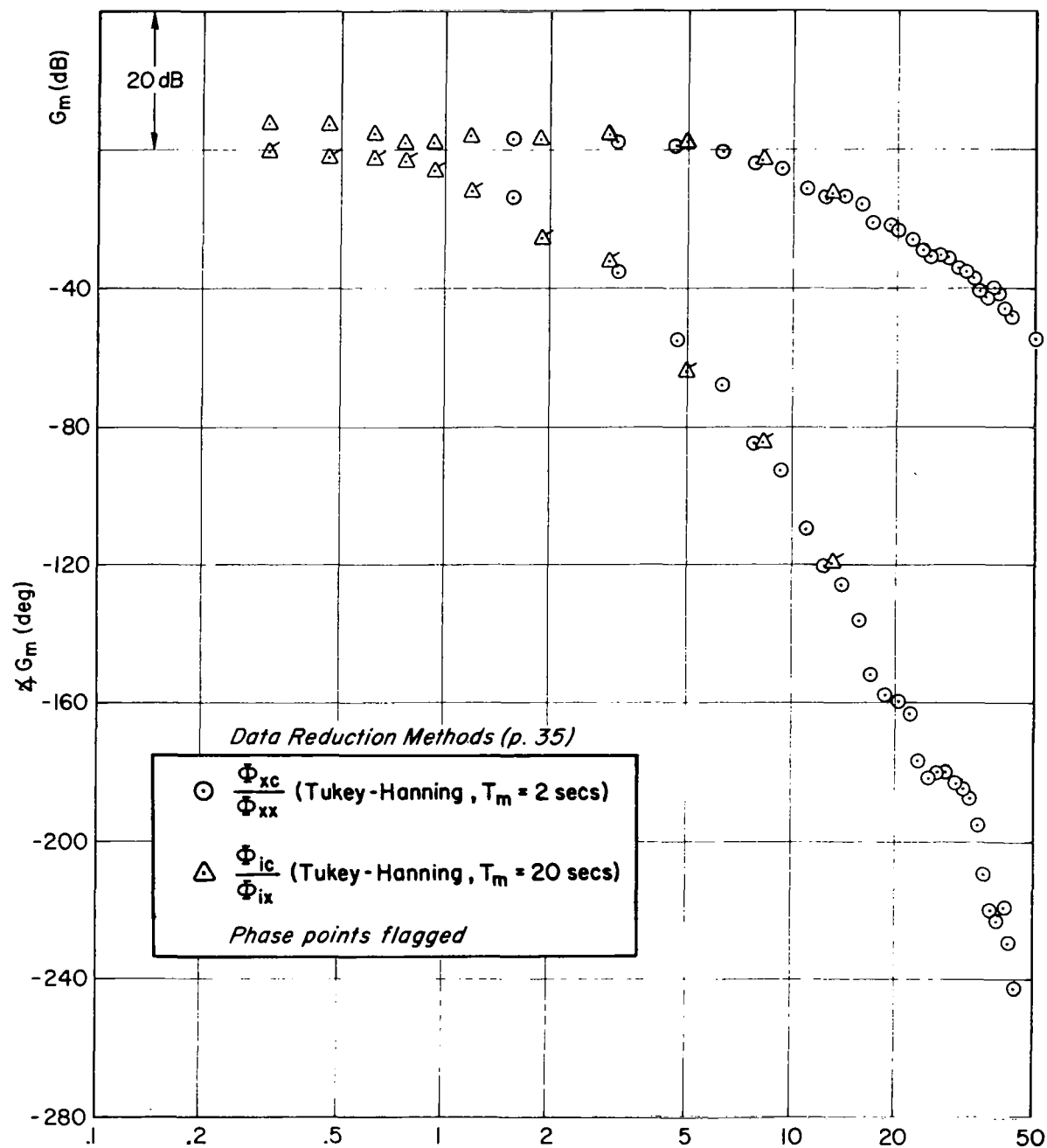


Figure 17. Muscle/Manipulator Describing Function, G_m ,
Rudder Pedals, $Y_{c1} = 0.25 / (s - 0.25)$

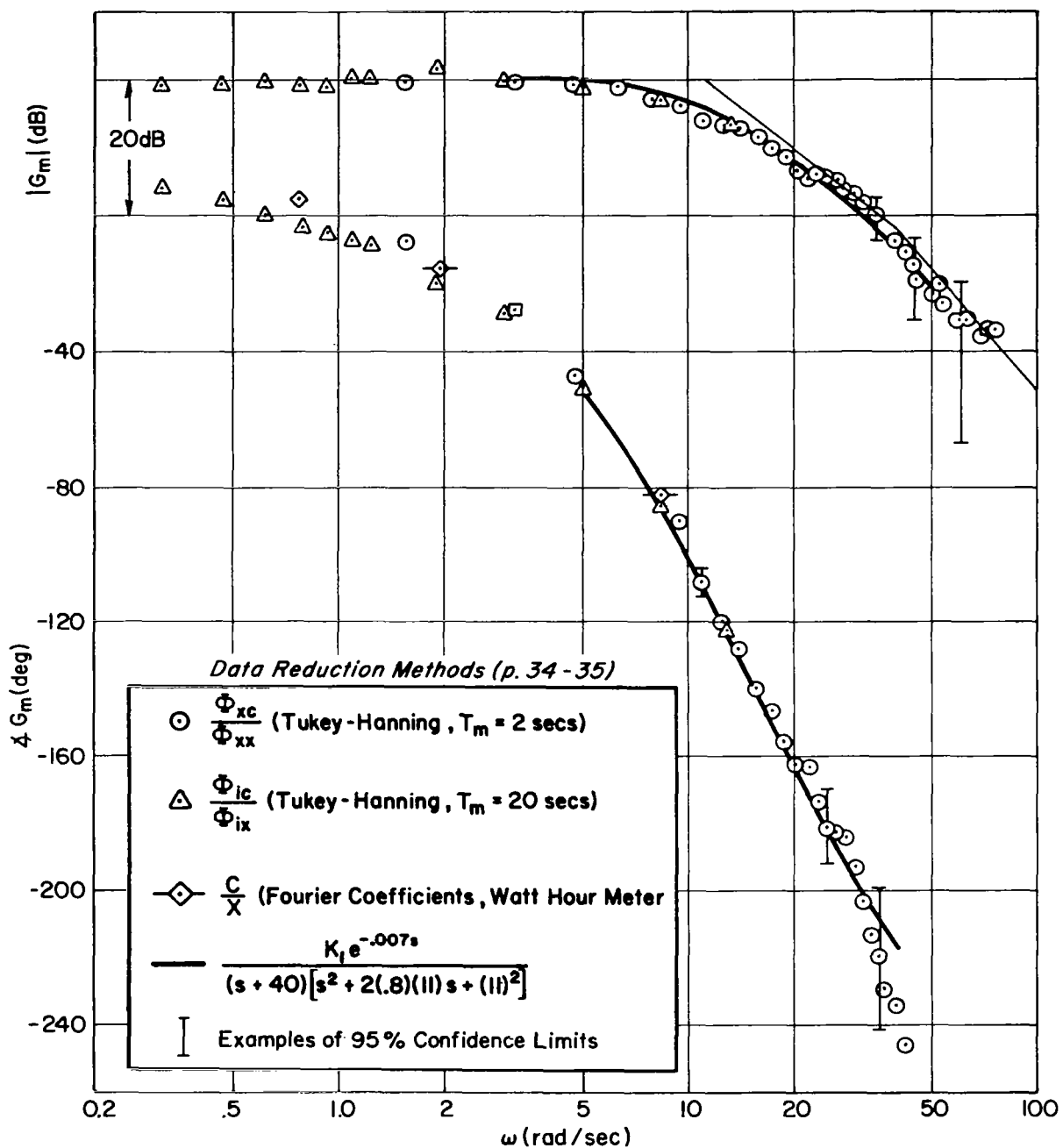


Figure 18. Muscle/Manipulator Describing Function, G_m ,
Rudder Pedals, $Y_{c1} = 1/(s-1)$

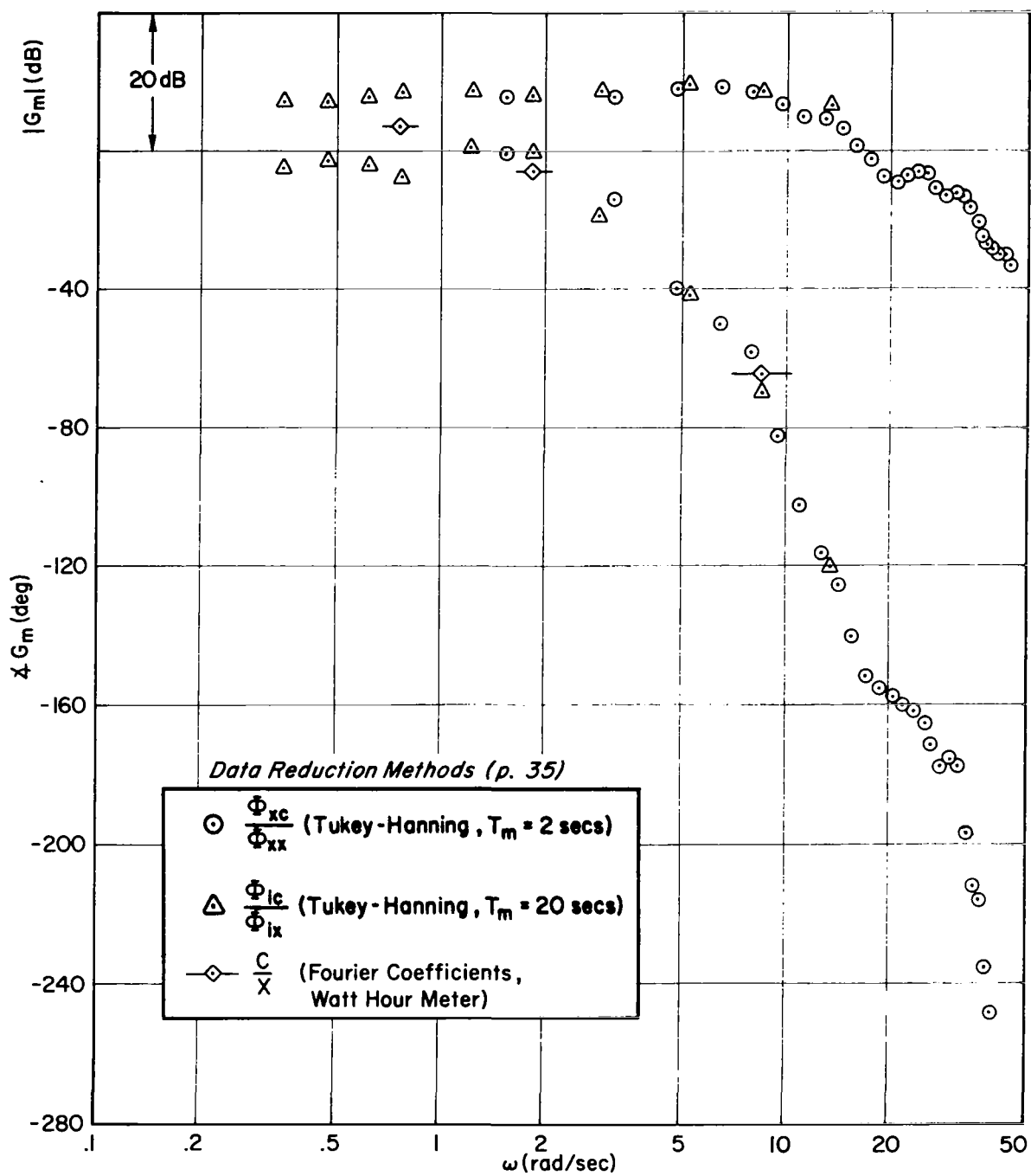


Figure 19. Muscle/Manipulator Describing Function, G_m ,
Rudder Pedals, $Y_{C_1} = 2/(s-2)$

excellent fit to the data and will be used in later figures for comparison purposes.

Table IV is a summary of the effects of average tension (in newtons) on the pilot's performance, crossover frequency, phase margin and the approximate model parameters (τ_e , α) for the three values of λ_1 .

TABLE IV
SUMMARY OF AVERAGE TENSION EFFECTS

| CONFIGURATION | ERROR PERFORMANCE | PILOT LOOP CLOSURE AND MODEL PARAMETERS | | | | AVERAGE TENSION |
|---------------|---------------------|---|-------------------|-------------------|----------------------------------|-----------------|
| λ_1 | σ_e/σ_i | ω_c (rad/sec) | ϕ_m (deg) | τ_e (sec) | α (sec ⁻¹) | (N) |
| 0.25 | 0.32 | 3.2 | 38 | 0.22 | 0.077 | 20-35 |
| 1.0 | 0.42 | 3.7 | 26 | 0.19 | 0.13 | 55.5 |
| 2.0 | 0.71 | 3.8 | 16 | 0.18 | 0.14 | 124.5 |

Error performance shows the typical increase with increasing task difficulty due to increasing λ_1 (Ref. 9). The crossover frequency increased slightly and the phase margin decreased considerably as λ increased. The τ_e and α values change for increases in average tension such that the "phase umbrella" (Fig. 2) moves to the right as λ_1 increases. Note that the effective time delay, τ_e , decreases as average tension increases thus providing the first direct measurement of this oft stated interpretation (Refs. 1, 19).

B. HAND MANIPULATOR DATA COMPARISONS

As discussed in the previous section, there are four muscles involved for the hand manipulator. The dominant muscle pair is adequate for finding the describing function, G_m , however, use of this pair alone does not give a clear indication of average tension effects, because of the partial involvement of the other two muscles. Consequently the dynamics of Y_p and G_m will be the major concern here.

Figure 20 shows a comparison of mean-square tracking error and overall coherence between the results obtained on this program and those obtained from Ref. 11 for the same subject and forcing function.* Generally the results obtained in this study either check very nicely with those for the same configurations or are disposed about them for cases where different instability values were used. For the Y_{c1} and Y_{c2} cases, the performance measures and error coherence are reasonably disposed about the actual values used in Ref. 11. For the Y_{c3} case the data falls generally within that obtained in Ref. 11 for the same instability value. Thus the data ties in very well with that for the same subject in an earlier study.

Figure 21 presents comparisons of pilot describing functions for various values of λ for the first and second-order subcritical tasks. For first order tasks (Fig. 21a), increasing λ_1 from 1 to 3 has essentially no effect on the amplitude ratio. However, the phase umbrella does tend to move to the right much as for the rudder pedal cases where there was also an increase in average tension.

Figure 21b shows the comparison of the pilot's describing function for the second order critical task for various values of λ_2 . Included is data for $\lambda_2 = 1.25$, the tie-in case from Ref. 11. The pilot's describing function data has been plotted with the free s taken out, that is, a pure lead is subtracted from the Y_p data. Having done this, the effective controlled element with respect to the modified pilot describing function, Y_p/s , in Fig. 21b is then $\lambda_2/s - \lambda_2$. The data plotted there is quite similar to that in Fig. 21a, that is, it is flat in the midband range and peaks up at the high frequency end indicating essentially the same dynamics in spite of the pilot's generating low frequency lead.

The fairings in Fig. 21b help highlight the similarities and dissimilarities in the pilot's describing function. For all values of λ_2 and ω_1 the amplitude ratio at the high frequency end is essentially the same in shape, indicating quite similar dynamics there. At the low frequency end the amplitude ratio for the $\lambda_2 = 0.5$ and 1.25 cases shows a rise indicating

*The exception is the $\lambda_2 = 2$, $\omega_1 = 2$ case since all the other second order controlled elements in Fig. 20 used $\omega_1 = 1$.

◇ Data from experiments discussed in this report, replications are tagged.
All other data from Ref. 11.

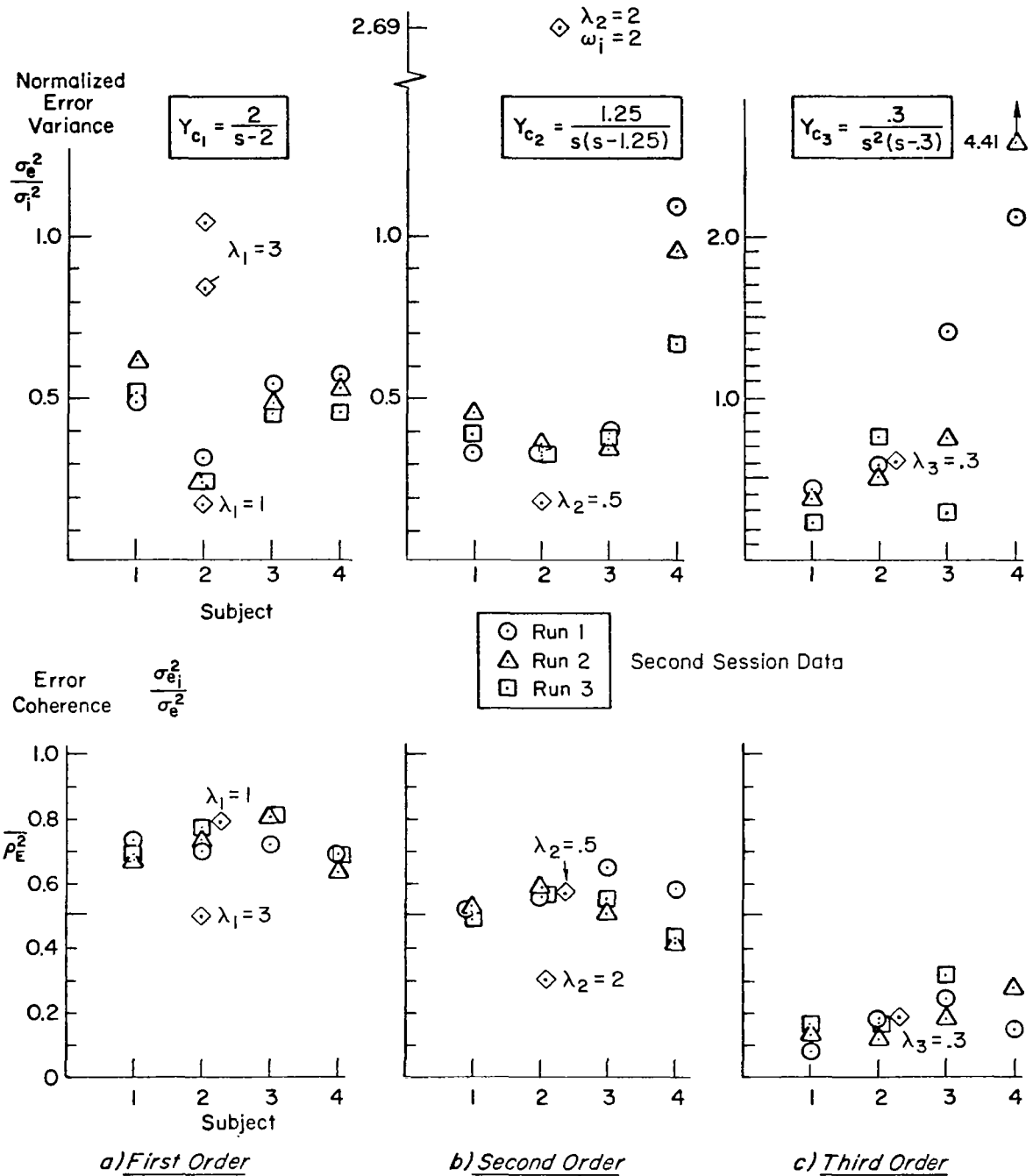
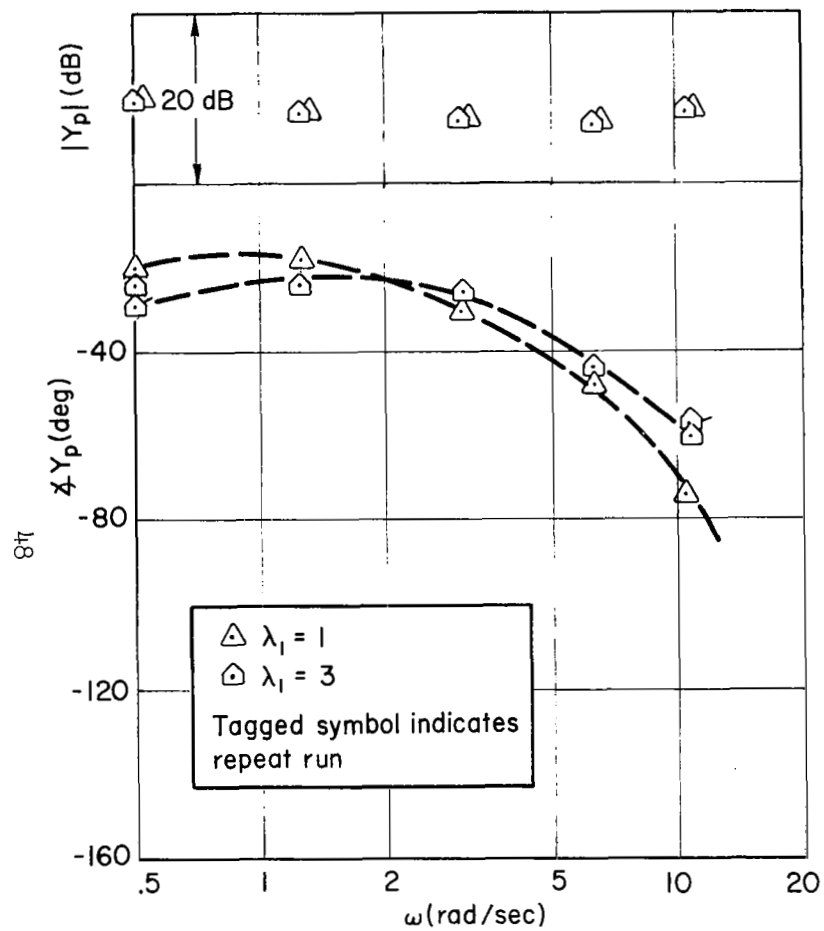
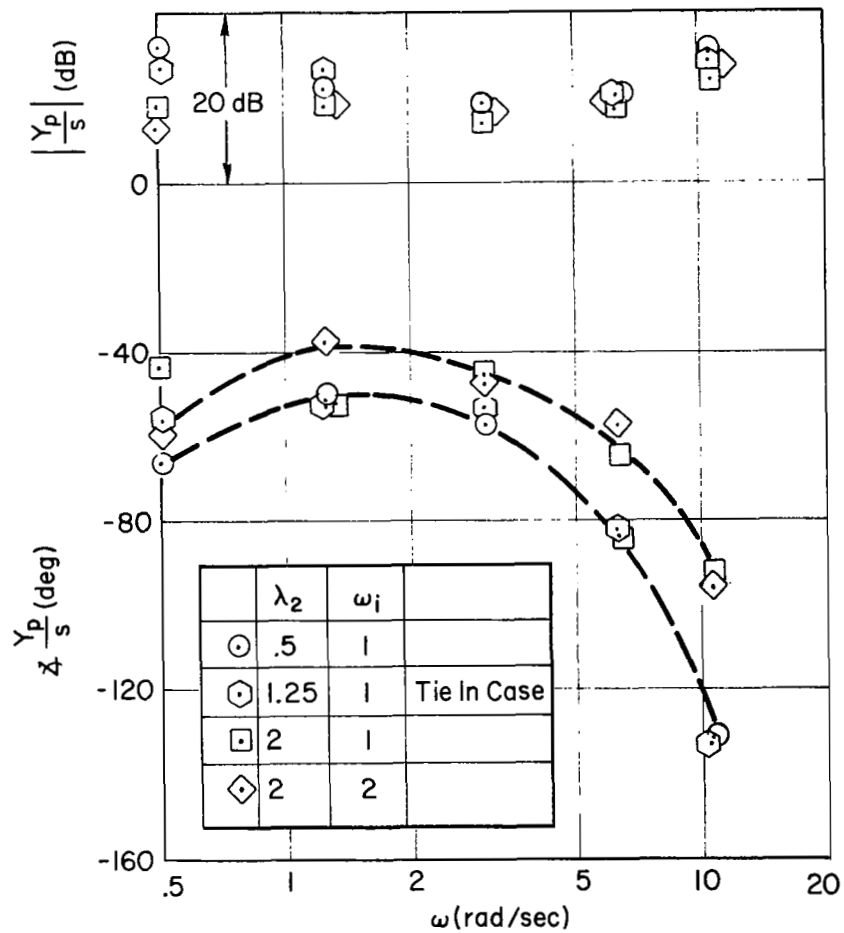


Figure 20. Tie-In of Mean-Square Tracking Error and Error Coherence with Previous Data (Ref. 11)



$$a) Y_{c1} = \frac{\lambda_1}{s - \lambda_1}$$



$$b) Y_{c2} = \frac{\lambda_2}{s(s - \lambda_2)}$$

Figure 21. Human Operator Describing Function, Y_p , for First- and Second-Order Tasks (Hand Manipulator)

the low frequency lead that the pilot has adopted to control this task. For the $\lambda_2 = 2$ cases, this lead appears to be at much lower frequencies, well below the measurement band. In addition these two cases had lower error coherence (larger remnant) and much larger relative mean-square error (Table V). These relatively noisier cases also have more scatter at the lowest frequency phase point than for $\lambda_2 = 0.5$ and 1.25. The phase data show significantly more phase lag at all frequencies for $\lambda_2 = 0.5$ and 1.25 compared with the $\lambda_2 = 2$ cases. The pilot's smaller phase lag for the $\lambda_2 = 2$ cases is essential for stability margin since the controlled element has more phase lag. If he had retained the phase lag for $\lambda_2 = 0.5$ there would be no stability margin at all. Thus the pilot appears to have the ability to modify his phase characteristics significantly without a large effect in his amplitude ratio, particularly at midband and higher frequencies.

Figure 22 shows the effects of controlled elements requiring lead generation on the pilot's describing function (first, second and third order tracking tasks require none, first order, and second order lead respectively). The smallest values of the controlled element instability frequencies are used in this comparison since these gave the most stable and lowest variability data. The plotting convention for the amplitude ratio is the same as that in Fig. 21b, with one free s taken out of the pilot's describing function for second order cases and two free s 's for the third order task. Further, the amplitude ratio data are plotted by arbitrarily lining up the midband region. The key effect at the high frequency end is that going from first to second order tasks produced a higher peaking up at a lower frequency thus indicating a difference in dynamics involved in the pilot's necessary task of generating increased low-frequency lead to stabilize the task. There is a very strong effect in the phase characteristics which indicate an increased effective time delay as a penalty for generating successively none, first and second order leads. If the pilot had generated the required lead perfectly, all the phase characteristics would line up, yet there is increased phase lag for second and third order tracking cases.

The performance measure comparison in Table VI shows that the first and second order tasks had essentially the same mean squared error, but the second order task had much more remnant leading to a lower ρ_E^2 . The much

TABLE V

ERROR PERFORMANCE MEASURES FOR SECOND ORDER TASKS
WITH VARIOUS INSTABILITY VALUES

$$Y_c = \frac{\lambda_2}{s(s-\lambda_2)}$$

| Run | λ_2 | ω_i | Relative Mean Square Error | | | Error Coherence |
|--------------------------|-------------|------------|---------------------------------|-------------------------------------|-------------------------------------|--|
| | | | Total | Correlated | Remnant | $\rho_E^2 = \frac{\sigma_{e_i}^2}{\sigma_e^2}$ |
| | | | $\frac{\sigma_e^2}{\sigma_i^2}$ | $\frac{\sigma_{e_i}^2}{\sigma_i^2}$ | $\frac{\sigma_{e_n}^2}{\sigma_i^2}$ | |
| 690521-7 | 0.5 | 1 | 0.193 | 0.103 | 0.090 | 0.534 |
| 690501-10/2 (Ref. 11) | 1.25 | 1 | 0.363 | 0.212 | 0.151 | 0.586 |
| 690521-5 | 2 | 1 | 1.15 | 0.348 | 0.805 | 0.302 |
| 690521-9 | 2 | 2 | 2.29 | 0.884 | 1.41 | 0.386 |

TABLE VI

ERROR PERFORMANCE MEASURES FOR EFFECTS OF LEAD GENERATION

| Run No. | Configuration | Relative Mean Square Error | | | Error Coherence | Low Frequency Lead Required |
|-----------|---------------------------------------|---------------------------------|-------------------------------------|-------------------------------------|-----------------|-----------------------------|
| | | Total | Correlated | Remnant | | |
| | | $\frac{\sigma_e^2}{\sigma_i^2}$ | $\frac{\sigma_{e_i}^2}{\sigma_i^2}$ | $\frac{\sigma_{e_n}^2}{\sigma_i^2}$ | ρ_E^2 | |
| 690521-12 | $\lambda_1 = 1.0$ $\omega_1 = 1$ | 0.187 | 0.148 | 0.039 | 0.79 | None |
| 690521-7 | $\lambda_2 = 0.5$ $\omega_1 = 1$ | 0.193 | 0.103 | 0.09 | 0.534 | First Order |
| 690524-9 | $\lambda_3 = 0.3$ $\omega_1 = 0.3$ | 0.624 | 0.121 | 0.503 | 0.194 | Second Order |

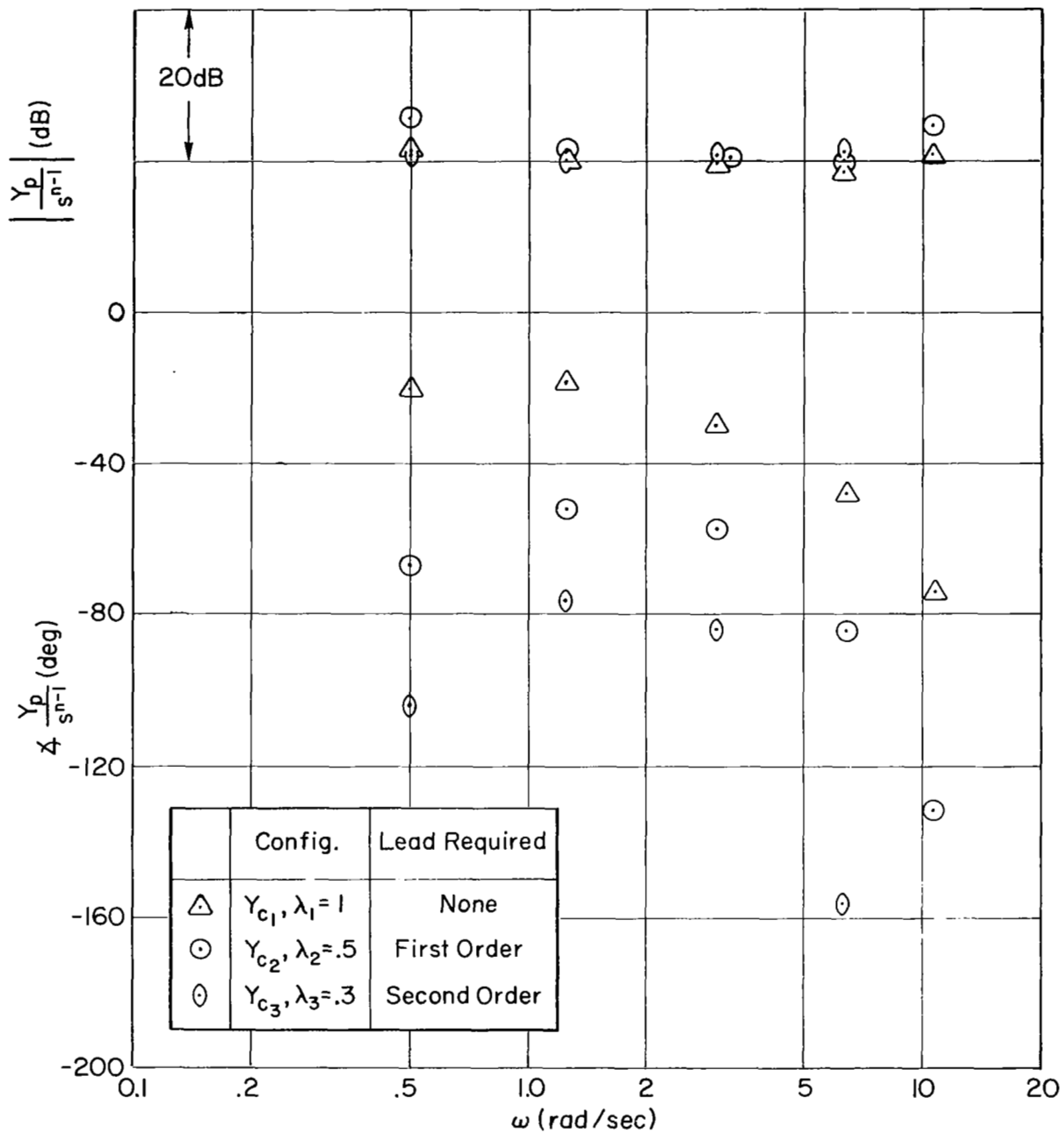


Figure 22. Effects of Controlled Elements Requiring Lead Generation on the Human Operator's Describing Function, Y_p (Hand Manipulator)

more difficult third order task had a very low ρ_E^2 , consistent with the pilot's very small phase margin and difficulty in tracking this task.

Figures 23-26 present measurements of G_m for cases of $\lambda_1 = 1, 3$, $\lambda_2 = .5$ and $\lambda_3 = .3$ respectively. The pilot's describing function for the corresponding cases can be found in Figs. 21 and 22. For each of the cases in Figs. 23-26 values of G_m measured at all frequencies are compared with those measured at forcing function frequencies. In addition, each of these figures contains a reference curve which is the curve fit to the data in Fig. 18 for the rudder pedal, $\lambda_1 = 1$ case, thus providing a ready comparison. Finally, in Figs. 24 and 26 results obtained using a single muscle (Extensor carpi radialis) are presented to compare with the dominant agonist/antagonist pair (for clarity the single muscle amplitude ratio results are arbitrarily displaced). The purpose here is to gain insight into the nature of the agonist/antagonist cooperation.

Figure 23 for $\lambda_1 = 1$ shows that measurements at all frequencies and at forcing function frequencies are essentially the same. The measurements at forcing function frequencies are in excellent agreement with the reference curve obtained for the rudder pedal case, and the all frequency measurements are in fair agreement. Generally, both the hand and the rudder pedal data give substantially the same measured dynamics for G_m . The data for $\lambda_1 = 3$, Fig. 24, is substantially similar to that for $\lambda_1 = 1$ in Fig. 23. However, in this case, the measurements at forcing function frequencies seem to bear out the all frequency measurements as to the presence of the high frequency rise just above 10 rad/sec. It is not entirely clear what the significance of this rise is since the phase characteristics that go with it are essentially the same as the rudder pedal reference curve phase whose amplitude ratio lacks this rise. It was suspected that the agonist/antagonist muscle combinations for this task may produce this effect since the muscles are not as well balanced a set as for the rudder pedal case. Therefore, G_m was computed for a few cases using the EMG from a single muscle of the agonist/antagonist pair, (Extensor carpi radialis). The data in Fig. 24 indicate that the single muscle results were substantially the same in amplitude ratio shape and phase as for the dominant agonist/antagonist muscle pair. This same comment applies to the data in Fig. 26 for the third order task. Thus

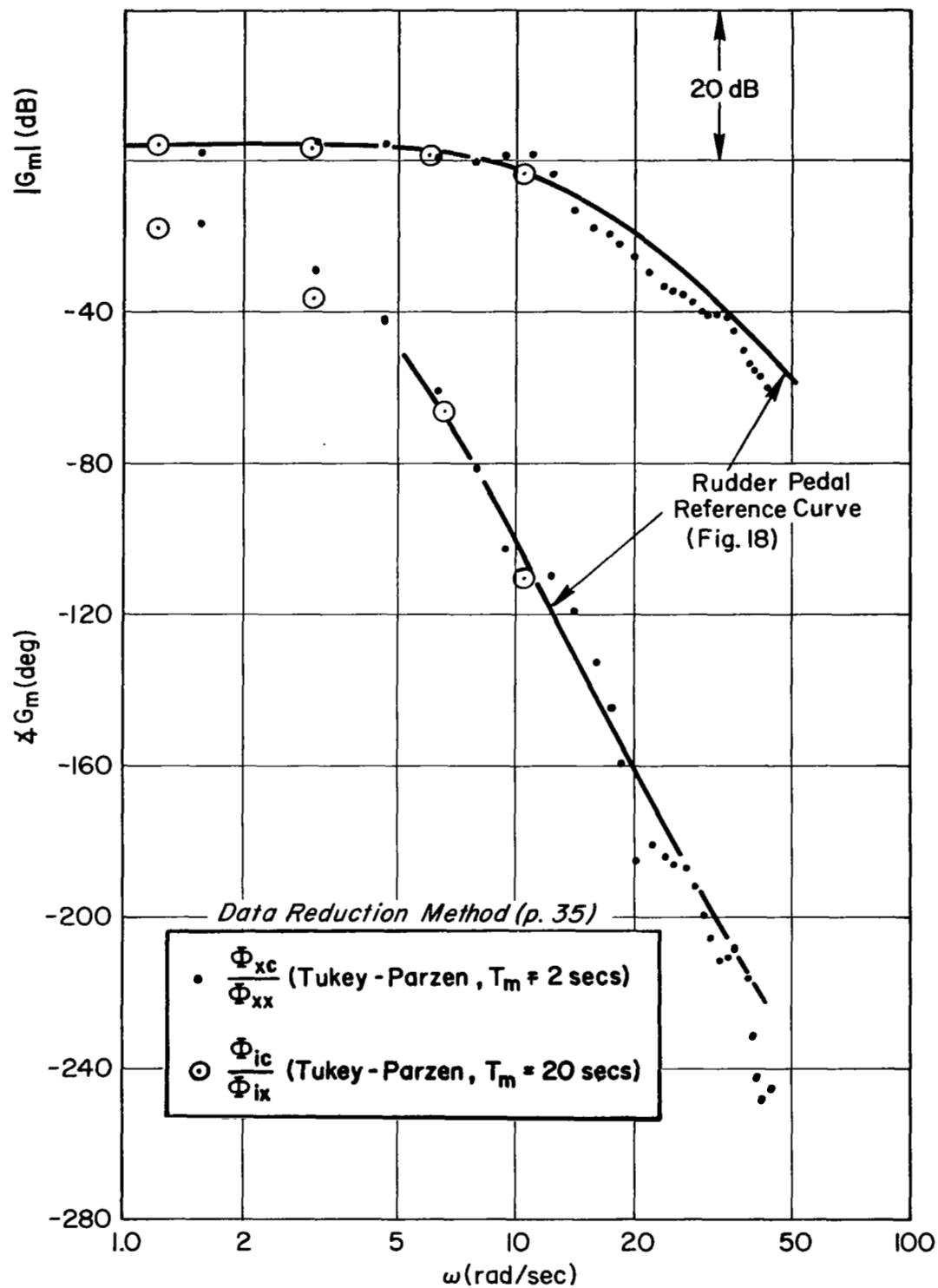


Figure 23. Muscle/Manipulator Describing Function, G_m
 [Hand Manipulator, $Y_{c1} = 1/(s-1)$]

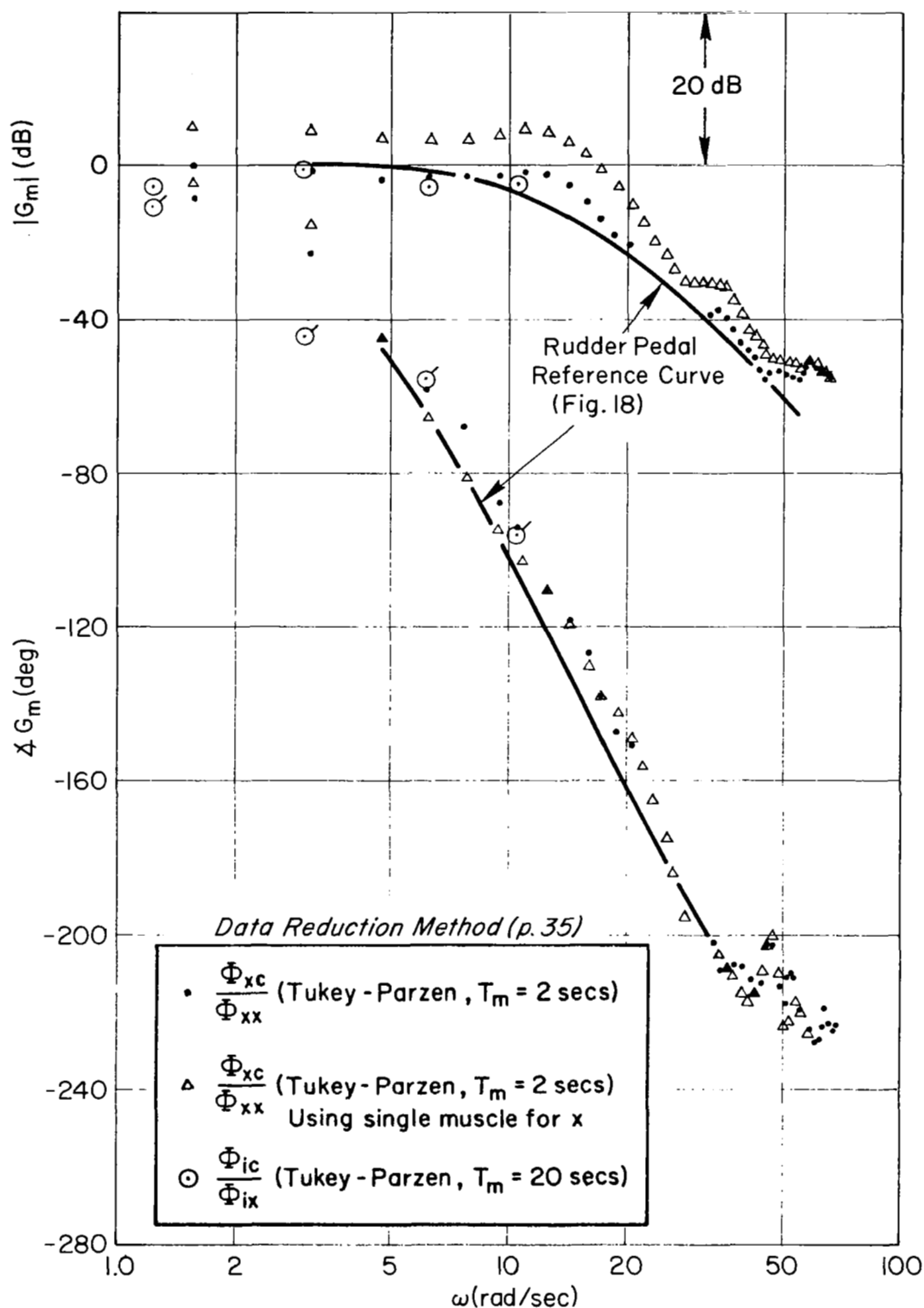


Figure 24. Muscle/Manipulator Describing Function, G_m
 [Hand Manipulator, $Y_{C1} = 3/(s-3)$]

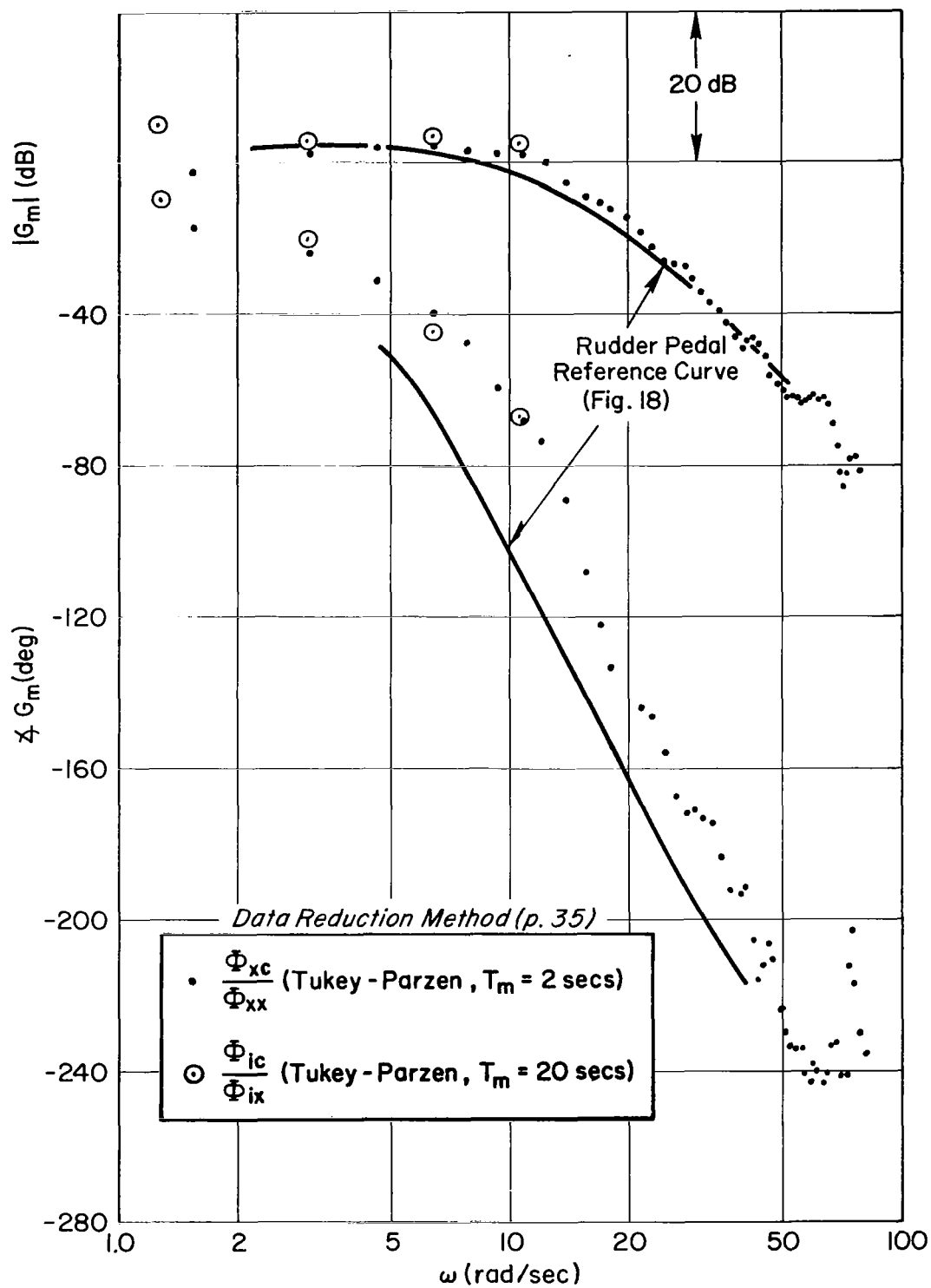


Figure 25. Muscle/Manipulator Describing Function, G_m
 [Hand Manipulator, $Y_{c2} = 0.5/s(s-0.5)$]

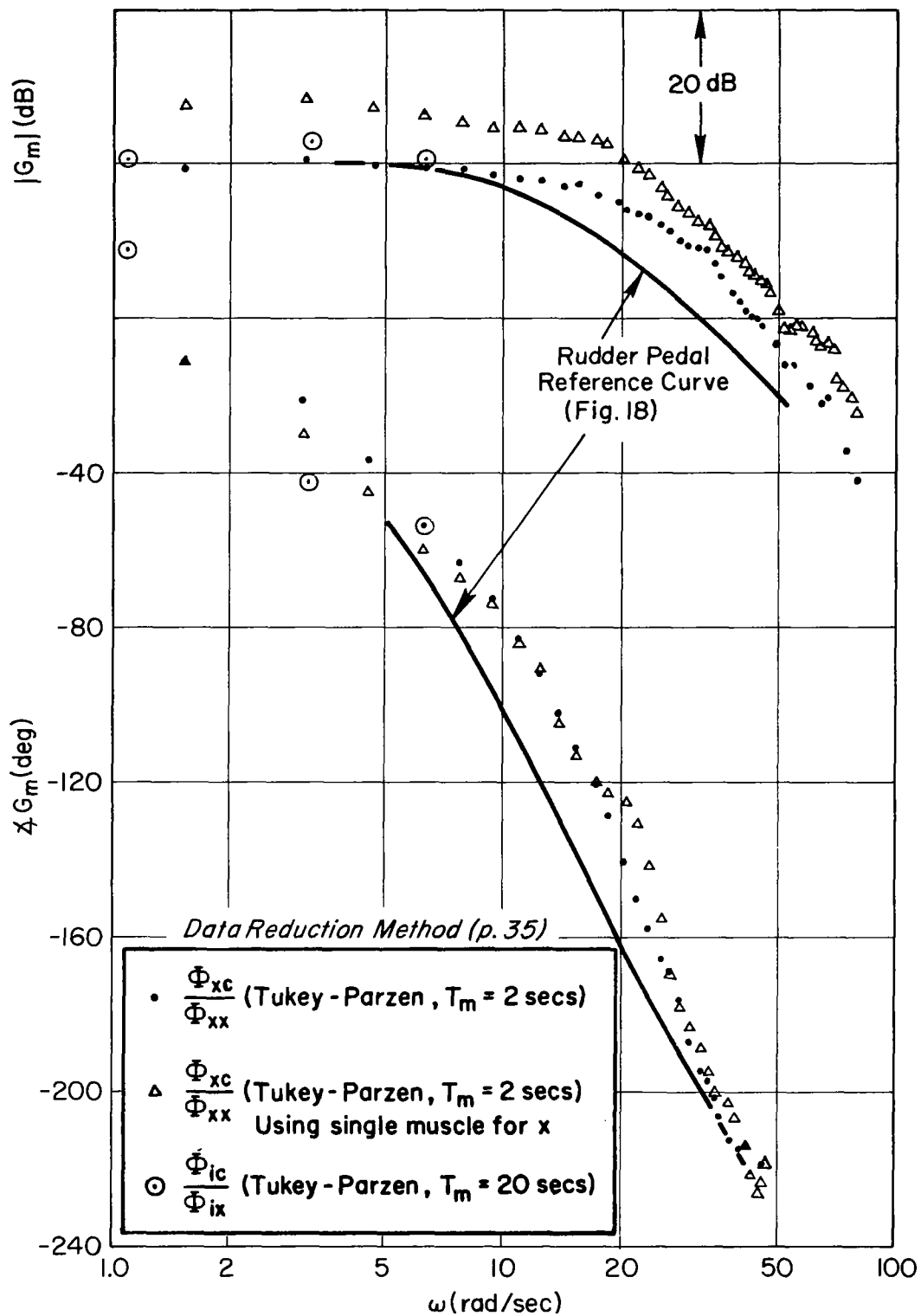


Figure 26. Muscle/Manipulator Describing Function, G_m
 [Hand Manipulator, $Y_{c3} = 0.3/s^3(s - 0.3)$]

although the agonist and antagonist muscles participate in the task with different sensitivities (EMG signal strength) the basic dynamics are very close in amplitude ratio and phasing.

Comparing Figs. 23, 25 and 26 shows that the need to generate none, first and second order lead respectively has relatively little effect on G_m , i.e., it is basically a low pass system with essentially the same high frequency rolloff rate. There are some differences in bandwidth and phase but these may reflect the participation of the other two of the four muscles involved in this task. As discussed in Section II these other muscles participate in the task but not in a pure agonist/antagonist cooperation and thus may contribute anomalous effects.

C. CONCLUSIONS

The inherently balanced agonist/antagonist muscle set involved in the rudder pedal experiments yielded high quality data for the average tension and all the describing functions taken. This data shows that the pilot's effective time delay decreased as average tension increased. This is the first direct proof of this relationship. The hand manipulator data demonstrated the relative invariance of the muscle/manipulator dynamics for controlled elements requiring a wide range of low frequency lead equalization. The more specific conclusions are:

1. Measurement Techniques and Data Processing
 - a. Agonist/antagonist muscles participate in push-pull fashion and each has a quasi-linear response thus validating the EMG signal processing method.
 - b. Forcing function frequencies show up in EMG signals well up out of the noise. At high frequencies the remnant was used as a test input to identify the muscle/manipulator system dynamics, such that at these frequencies measurements of G_m obtained from Fourier coefficients gave the same results as the classical Tukey method where the latter used both a narrow and a wide bandwidth filter.
 - c. High fidelity measurements of muscle/manipulator dynamics were obtained for the rudder pedals (balanced muscle groups).

2. Direct Measurements of Muscle/Manipulator Dynamics, G_m

- a. For the rudder pedals G_m is closely described by a third order system plus time delay. All modes appear at high frequency, thus the Ref. 1 assumption that one real pole of G_m appeared at low frequency is no longer valid. Thus the loop closure to describe the effects of the closed loop neuromuscular system on the pilot's high frequency dynamics must be revised (see next section).
- b. For the hand manipulator G_m was basically unchanged for first, second and third order subcritical tasks requiring none, first and second order lead respectively.
- c. G_m for rudder pedals and hand manipulator was quite similar in form and close in bandwidth despite the difference in limb size and function.

SECTION IV

DESCRIBING FUNCTION DATA INTERPRETATION AND MODEL REVISION

This section presents interpretations of key features in both the data from this program and some data available in the recent literature. The effects of a wide range of spring restraints on the neuromuscular systems' contributions to the pilot's overall dynamic response will be presented. The role of the neuromuscular system in lead generation situations will be considered next. Finally model revisions suggested by the data will be drawn.

A. NEUROMUSCULAR SYSTEM MODEL

Figure 27 shows the neuromuscular system model interpretation of Fig. 6 to be used in this section to explain the experimental data in the previous section plus some data from the literature. [While the retinal and central equalization shown in Fig. 27 is for rate dynamics ($Y_c = K/s$) this block will change for other controlled elements.] The muscle/manipulator actuation dynamics, G_m , consists of a third order system (one real root and a quadratic pair) and a time delay. This form is consistent with the measured results in Fig. 18 of Section III. For reasons that will become clear later the alpha motor neuron command, α_c , (rather than the gamma motor neuron command, γ_c) is used as the command input from higher centers down to the spinal cord. The effects of the gamma bias signal, γ_b , while not shown explicitly in Fig. 27, is used to set up the spindle feedback operating point equalization.* As discussed in the Introduction, the effective joint sensor feedback is a gain and time delay for the frequency region of interest. In addition this feedback goes to higher centers—in Fig. 27 this is shown as a simple feedback plus a possible change in central time delay, τ_c , as shown by the dotted line.

*The spindle feedback block also serves as an approximation of the Golgi force feedbacks as discussed in the Introduction.

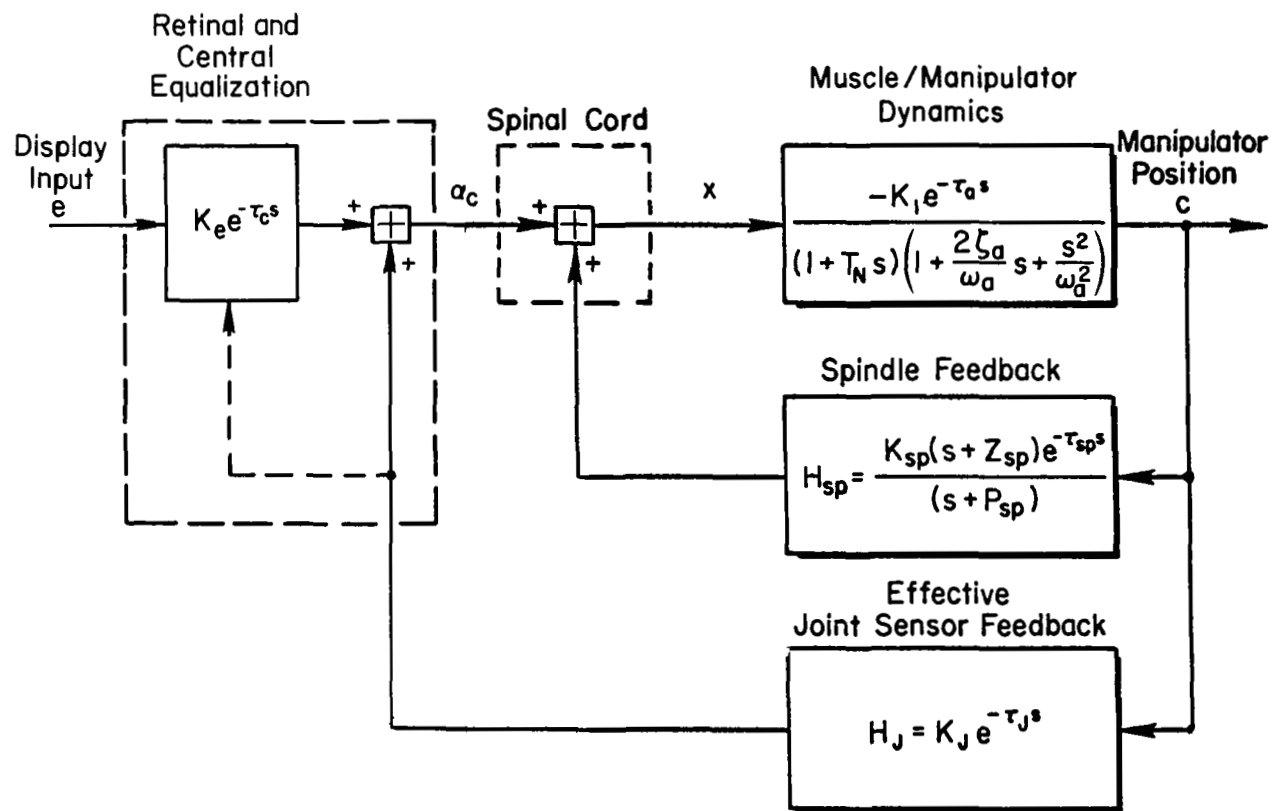


Figure 27. Neuromuscular Subsystems for Free-Moving and Pressure Manipulators and Central Equalization for Rate Dynamics

B. CLOSED LOOP NEUROMUSCULAR SYSTEM FOR VARIOUS MANIPULATOR RESTRAINTS

References 7 and 8 presented the effects of manipulator restraints on human operator dynamics. In particular these were the first to note that with an isometric manipulator the subjects had a smaller effective time delay than with an isotonic manipulator. Recently Ref. 20, using revised forcing function spectral shapes, has also obtained describing function data for these manipulator extremes. Figure 28 is an example showing a high frequency peak in the human operator describing function. Here a free-moving (isotonic) manipulator was used to control rate dynamics ($Y_c = K/s$).^{*} That this peak is due to the closed-loop neuromuscular system will be shown using the measured results for G_m and reasonable assumptions about the feedback elements in Fig. 27. Model implications from the curve fits to the data for both pressure and free sticks (Ref. 20) will be used to guide the curve fit to the rudder pedal data given in Section III.

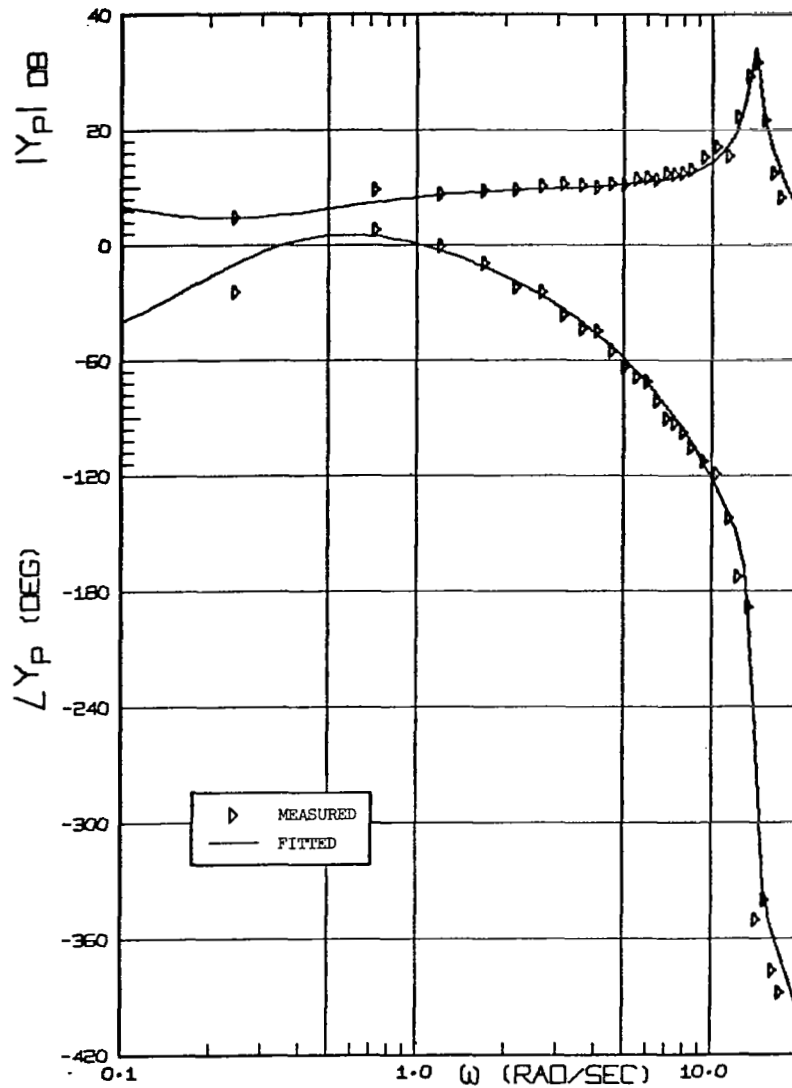
1. Neuromuscular System Closure for Isometric Manipulator

Data for a pressure stick from Ref. 20 will be fit with the model in Fig. 27 using the following values and assumptions:

$$\begin{array}{l} \text{Muscle/Manipulator} \\ \text{Dynamics} \\ G_m \end{array} \left\{ \begin{array}{l} \frac{1}{T_N} = 30 \text{ rad/sec} \\ \zeta_a = 0.8 \\ \omega_a = 10 \text{ rad/sec} \\ \tau_a = 0.017 \text{ sec} \end{array} \right.$$

$$\begin{array}{l} \text{Spindle} \\ \text{Feedback} \end{array} \left\{ \begin{array}{l} Z_{sp} = 11 \text{ rad/sec} \\ P_{sp} = 40 \text{ rad/sec} \\ \tau_{sp} = 0.023 \text{ sec} \end{array} \right.$$

^{*}The forcing function bandwidth is stated as 4 rad/sec although the half power point in the spectral envelope is closer to 2.5 rad/sec.



RUN 4079. SUBJECT LR. $\omega_1 = 4.0$ RAD/SEC. FREE-MOVING MANIPULATOR.

Figure 28. Example Describing Function Showing High Frequency Peak
(Taken from Gorden-Smith, Ref. 20)

Joint Sensor
Feedback

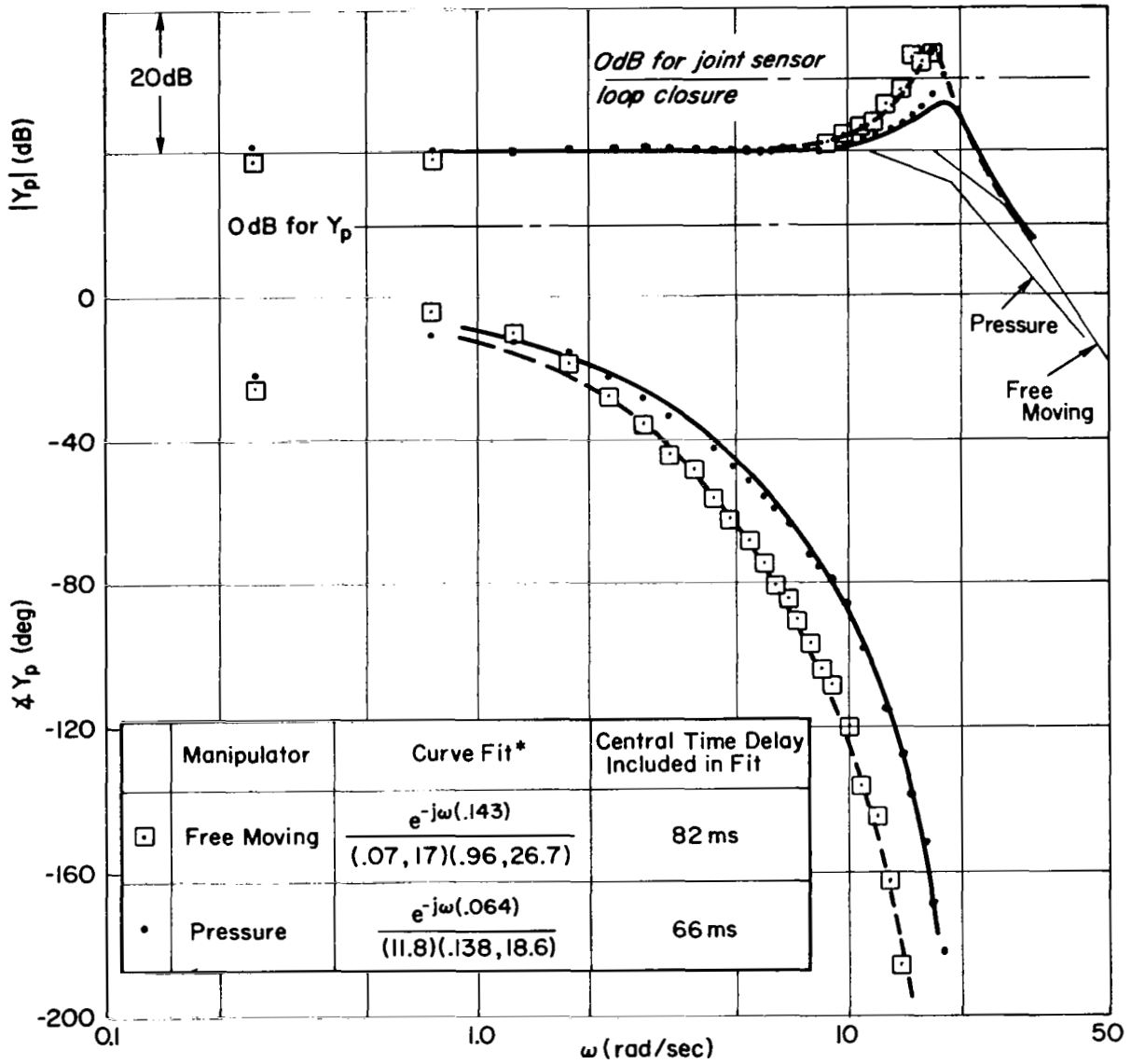
$K_J \doteq 0$ i.e., assume that this feedback has no significant effect for pressure manipulators due to the minute position excursions. This feedback will be invoked later to explain the free moving stick data.

The above values for G_m are very close to those for the reference curve fit in Fig. 18 for rudder pedal. The parameter values assumed for the spindle feedback are consistent with Ref. 21 for the approximately 4 to 1 lead-lag ratio and with Fig. 44 of Ref. 1 for the frequency location.

Figure 29 shows the Bode and root locus diagrams for the neuromuscular system closure. In the root locus as the loop gain increases, the quadratic mode moves up and eventually goes unstable just above 20 rad/sec. For the loop gain selected, the closed-loop quadratic roots are indicated by (ζ_N, ω_N) . Further, the open loop real root, $1/T_N$, has been driven very close to the spindle zero and its closed-loop value is indicated by $1/T_{N_1}$. A pole starts from the spindle pole, P_{sp} , moves out toward higher frequency as loop gain is increased and combines with the loop time delay forming very high frequency roots (not shown). In the Bode plot the loop gain selected gives a crossover frequency at 15 rad/sec and a phase margin of 36° . The gain margin is 4 dB. The dotted line in the amplitude ratio plot is the locus of the natural frequency of the quadratic as a function of loop gain. The locus of the real root is very steep indicating that this root is insensitive to loop gain.

The uppermost part of the Bode plot shows the closed-loop response, c/α_c , (labeled A) as well as for loop gains 2.1 dB higher and 1.4 dB lower than the nominal. Note that these gain changes merely change the amount of peaking up in the range 16 to 20 rad/sec and that the amplitude rise up to 15 rad/sec is essentially invariant. This partly reflects the invariance of the real root, $1/T_{N_1}$, to loop gain. Finally the spindle pole, P_{sp} , appears as a zero in the closed loop response.

Figure 30 shows the human operator describing function for rate control dynamics for the extremes of pressure and free moving manipulators (Ref. 20).



*Note: To simplify the notation, $(s^2 + 2\zeta\omega s + \omega^2)$ is written (ζ, ω) and $(s + a)$ is written (a) .

Figure 30. Closed-Loop Neuromuscular System Model Fit to Y_p for Pressure and Free-Moving Manipulator (Ref. 20, $Y_c = 1/s$)

This data is the average of eight subjects with four runs on each manipulator. The pressure case is fit* by curve A for c/α_c in Fig. 29 plus a central time delay of 0.066 sec. Over most of the frequency range this is an excellent fit.

2. Neuromuscular System Closure for Isotonic Manipulator

For the free moving stick, the hand motions involved generate a joint sensor feedback signal in controlling the task (Fig. 27). To simplify the analysis the same muscle/manipulator and spindle feedback characteristics as used for the pressure manipulator was used for the free moving manipulator. Thus the effective actuation block for the joint sensor feedback (Fig. 27) is c/α_c which can be obtained from the curve fit to the pressure manipulator (Fig. 30) by removing the effects of the central time delay of 66 ms.

A value for the joint sensor feedback time delay of $\tau_J = .086$ secs was used along with a loop gain that is indicated by the "0 dB for joint sensor loop closure" on Fig. 30, i.e., the solid line curve fit relative to this 0 dB line indicates the magnitude of the joint sensor loop closure gain used. The effects of this loop closure on the lightly damped neuromuscular system quadratic mode can be seen in the root locus (Fig. 29) as well as the amplitude ratio curve fit to the free moving manipulator data (Fig. 30). The phase curve fit to the free moving manipulator data contains a larger central time delay (82 ms) than for pressure manipulator (66 ms) reflecting longer transmission and processing time. Thus a relatively low gain joint sensor feedback gives an excellent fit to the free moving manipulator data.

3. Neuromuscular System Closure for Rudder Pedal Manipulator

The neuromuscular system closure has also been applied to Y_p (rudder pedal) given in Fig. 15 using the curve fit to the direct measurements of G_m given in Fig. 18. For this fairly stiff spring-restrained case (nearly isometric) the same assumptions as in fitting the pressure stick data in

*Very high frequency modes in curve A have been lumped into the equivalent time delay term.

Fig. 30 are made, that is, spindle feedback only. The same lead-lag spindle equalization is used, except in this case the spindle time delay, τ_{sp} is taken as 43 ms. This larger value is consistent with the longer pathways involved in leg muscles. Using the actual measured muscle/manipulator actuation dynamics given in Fig. 18, the resulting curve fit is given in Fig. 31. A central time delay of 126 ms was used as well as a low frequency lag-lead (Eq. 1) to fit the low frequency data. A very good fit to the data results.

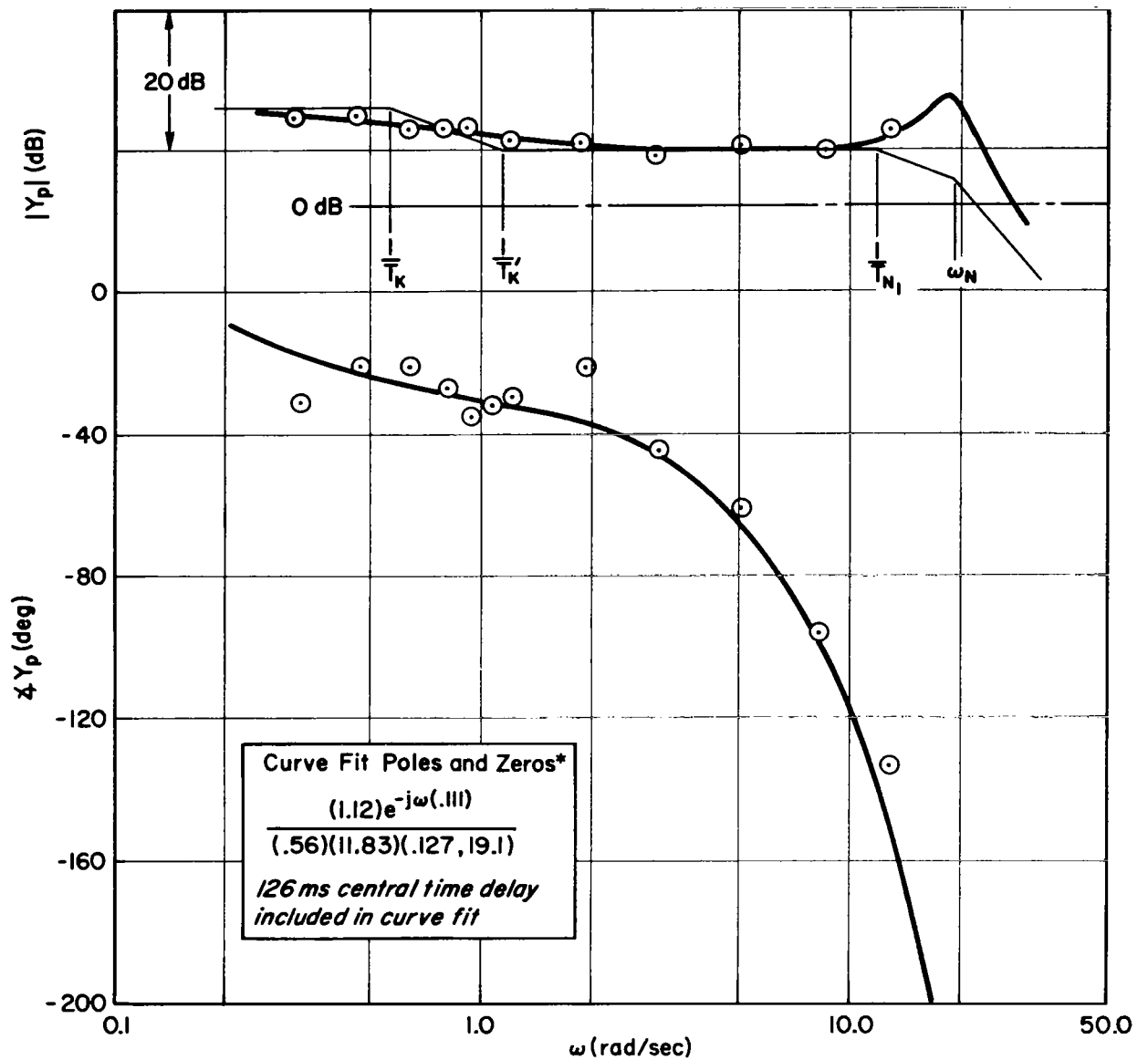
Thus, a straightforward application of the neuromuscular system model involving direct measurements of the muscle actuation path and some simple but quite reasonable assumptions about the feedback path yields a closed-loop neuromuscular system which gives an excellent fit to the high frequency peak in the human operators describing function data for a wide range of limb groups and manipulator restraints.

The models, data and curve fits presented in this section indicate that the alpha motor neuron command, α_c , is the major command input since if the gamma motor neuron command, γ_c , were dominant then the spindle lead would appear in the forward loop portion of the neuromuscular system (Fig. 6) and this would nearly cancel the closed loop pole, $1/T_{N1}$, which is very close to the spindle lead (Fig. 29).

A feature to be noted from Figs. 27-31 is that the spindle feedback pole, P_{sp} , will appear in the closed loop response of c/α_c as a zero, thus providing phase lead in the closed loop neuromuscular system at the higher frequency end. For the two curve fits presented this is in the region of 30-40 rad/sec. This feature is utilized in some precision curve fits in the next subsection for the key data involved in determining the effects of generating low frequency lead equalization.

C. EFFECTS OF LOW FREQUENCY LEAD GENERATION ON Y_p

The high-quality low-variability data indicating effects of lead generation was compared in Fig. 23. For the first- and second-order cases precision curve fits of the human operator describing function data will be presented. The model shown in Fig. 32 incorporates the qualitative effects of the neuromuscular system modes just discussed. The closed loop neuromuscular



*Note: To simplify the notation, $(s^2 + 2\zeta\omega s + \omega^2)$ is written (ζ, ω) and $(s + a)$ is written (a) .

Figure 31. Closed-Loop Neuromuscular System Model Fit to Y_p [Rudder Pedal, $Y_{c1} = 1/(s-1)$]

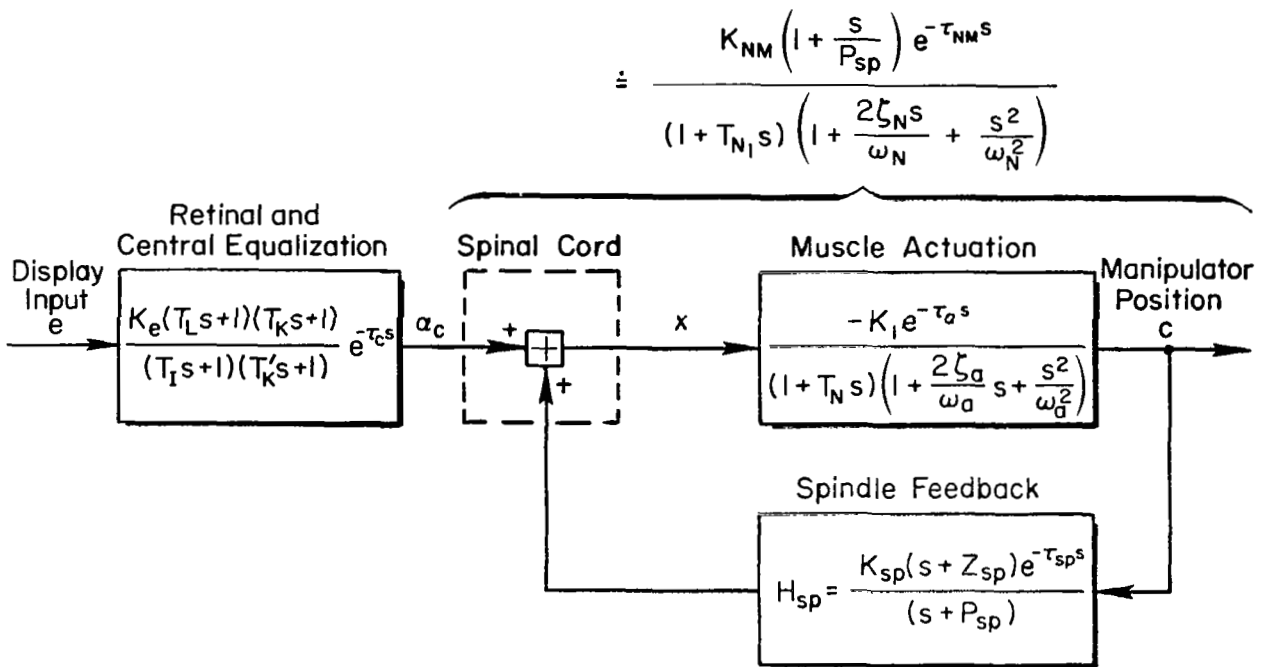


Figure 32. Neuromuscular Subsystem for Pressure Manipulator and Central Equalization Form for First- and Second-Order Dynamics

system has third order dynamics plus a zero due to the spindle pole in the feedback loop. The retinal and central equalization contain terms for lead and lag equalization (T_L , T_I), low frequency phase effects (T_K , T'_K) and time delay, τ_c . These curve fits are shown in Figs. 33 and 34 for the first and second order tasks, respectively. In both figures the neuromuscular modes show up as a real root, a lightly damped quadratic, and a real zero at relatively high frequencies (due to the spindle pole in the feedback path). Note that the neuromuscular modes* show up very clearly in both Fig. 33 and 34. However for the second order task all modes are at lower frequency than their counterparts for the first order task. In addition the lightly damped quadratic is more lightly damped for the second order task than for first-order tasks. This indicates that the neuromuscular system has been closed in a tighter fashion in an attempt to reduce the effective time delays due to these quadratic modes. That is, reducing damping reduces the phase lag at frequencies much less than the undamped natural frequency. The lower position for the neuromuscular system real root, $1/T_{N1}$, for the second order task indicates that the spindle lead-lag must have been at a lower frequency. Refer back to Fig. 29, which illustrates that the closed-loop root, $1/T_{N1}$, is driven very close to the spindle lead break frequency for a wide range of loop gains.

In addition to the precision model fits to the first- and second-order task data the effective time delay for the approximate model fit is given in Figs. 33, 34. The effective time delay due to the high frequency neuromuscular modes is given in literal terms as

$$\tau_e = \tau_c + \underbrace{T_{N1} + \frac{2\zeta_N}{\omega_N} - \frac{1}{P_{sp}}}_{\text{Neuromuscular Components}} \quad (14)$$

*For constant muscle-spindle loop gain the lightly damped neuromuscular modes do not control the tracking loop system stability, i.e., if the pilot should adopt too large a gain (in Y_p) the system would go unstable in the crossover frequency region (3-5 rad/sec).

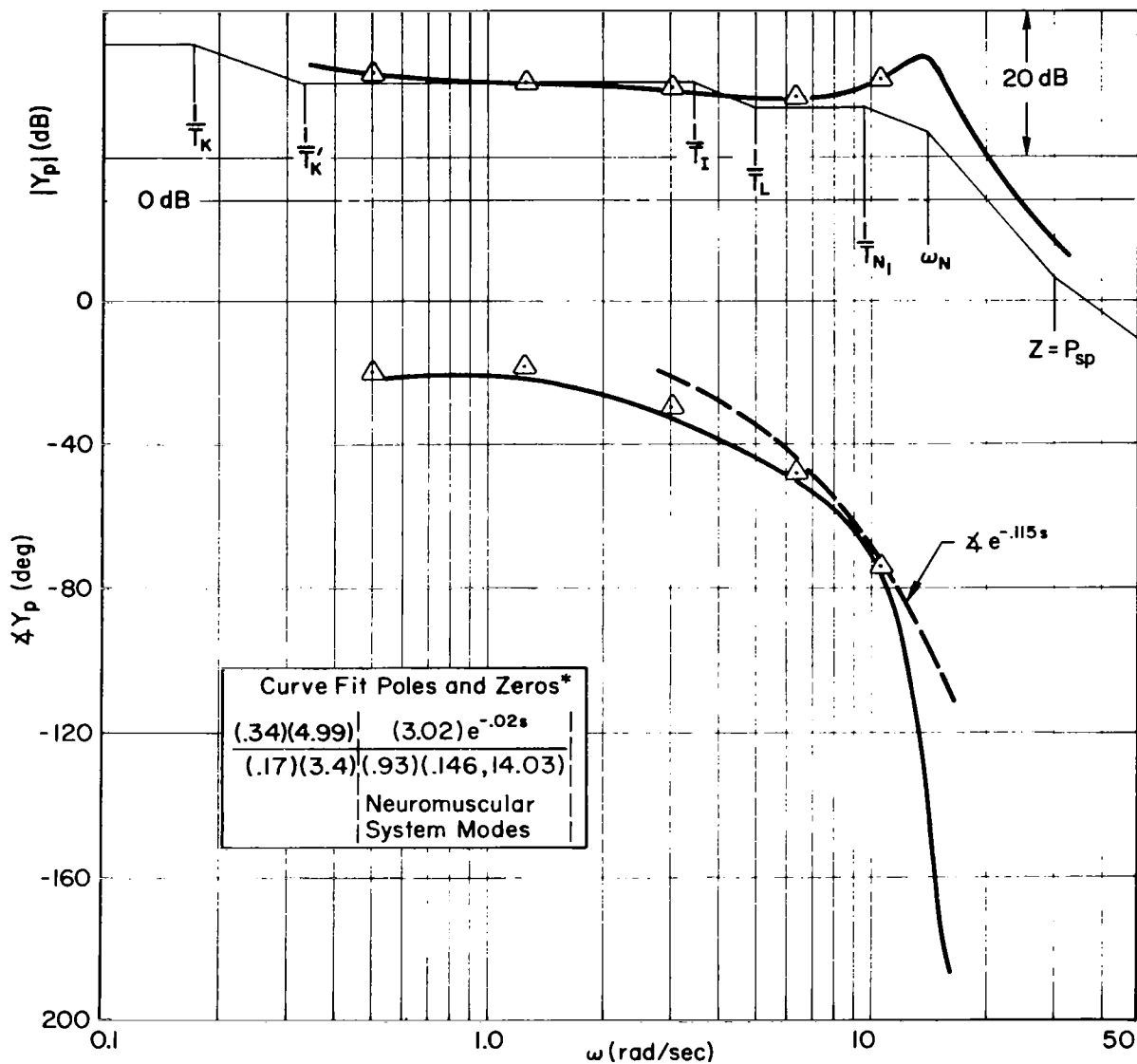
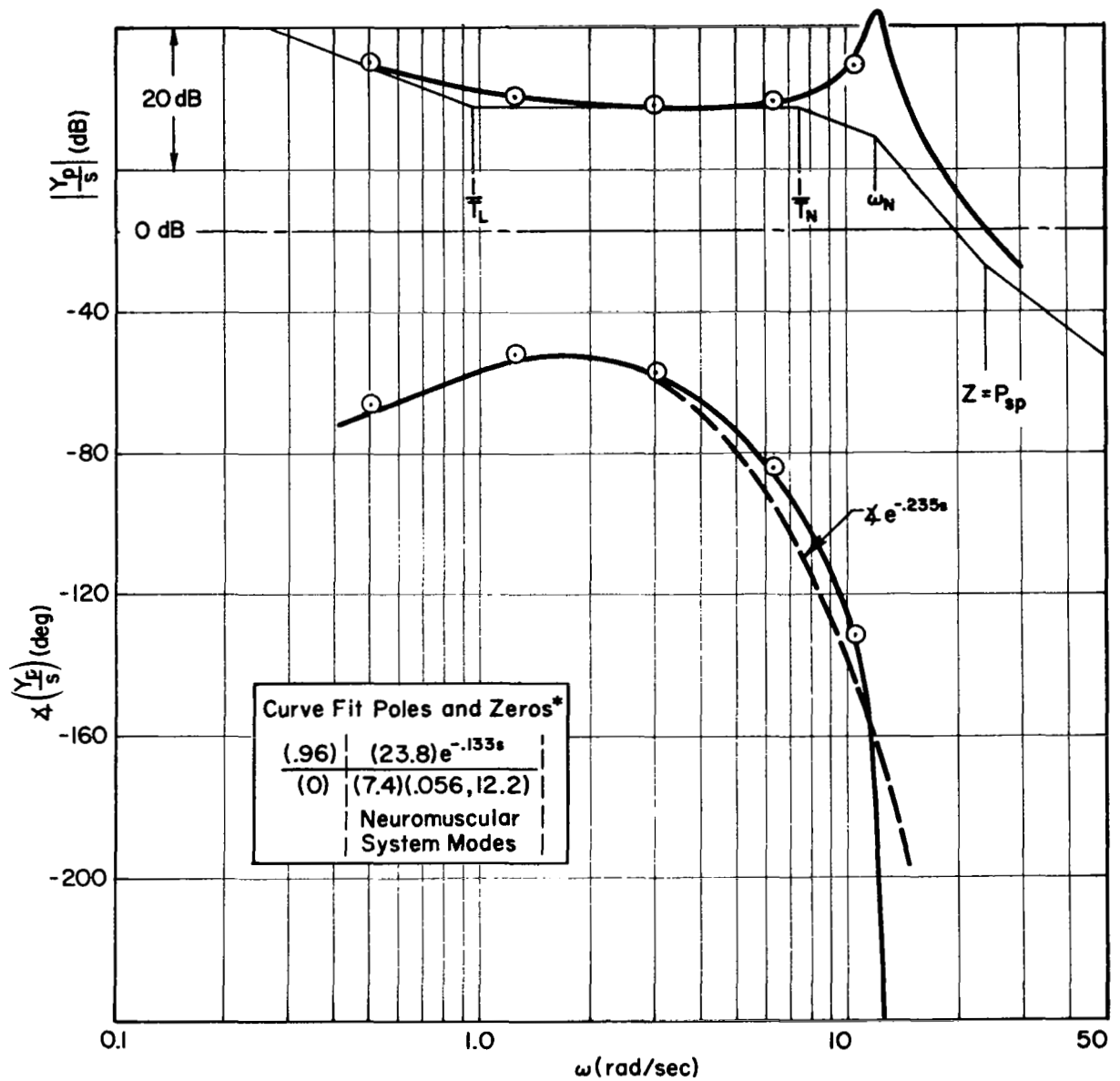


Figure 33. Precision Fit to Human Operator Describing Function, Y_p
[Hand Manipulator, $Y_{c1} = 1/(s-1)$]



*Note: To simplify the notation, $(s^2 + 2\zeta\omega s + \omega^2)$ is written (ζ, ω) and $(s + a)$ is written (a) .

Figure 34. Precision Fit to Human Operator Describing Function, Y_p/s
[Hand Manipulator, $Y_{c2} = 0.5/s(s - 0.5)$]

Table VII shows the contributions to τ_e from central and neuromuscular systems. The contributions to τ_e due to neuromuscular system modes are relatively invariant between first- and second-order tasks. The difference in τ_e (0.12 sec) is almost entirely due to central effects. This is the time delay penalty involved in establishing the low-frequency lead required in a second-order task. Thus the neuromuscular system is relatively unchanged by the need to establish low-frequency lead indicating that this lead is generated centrally.

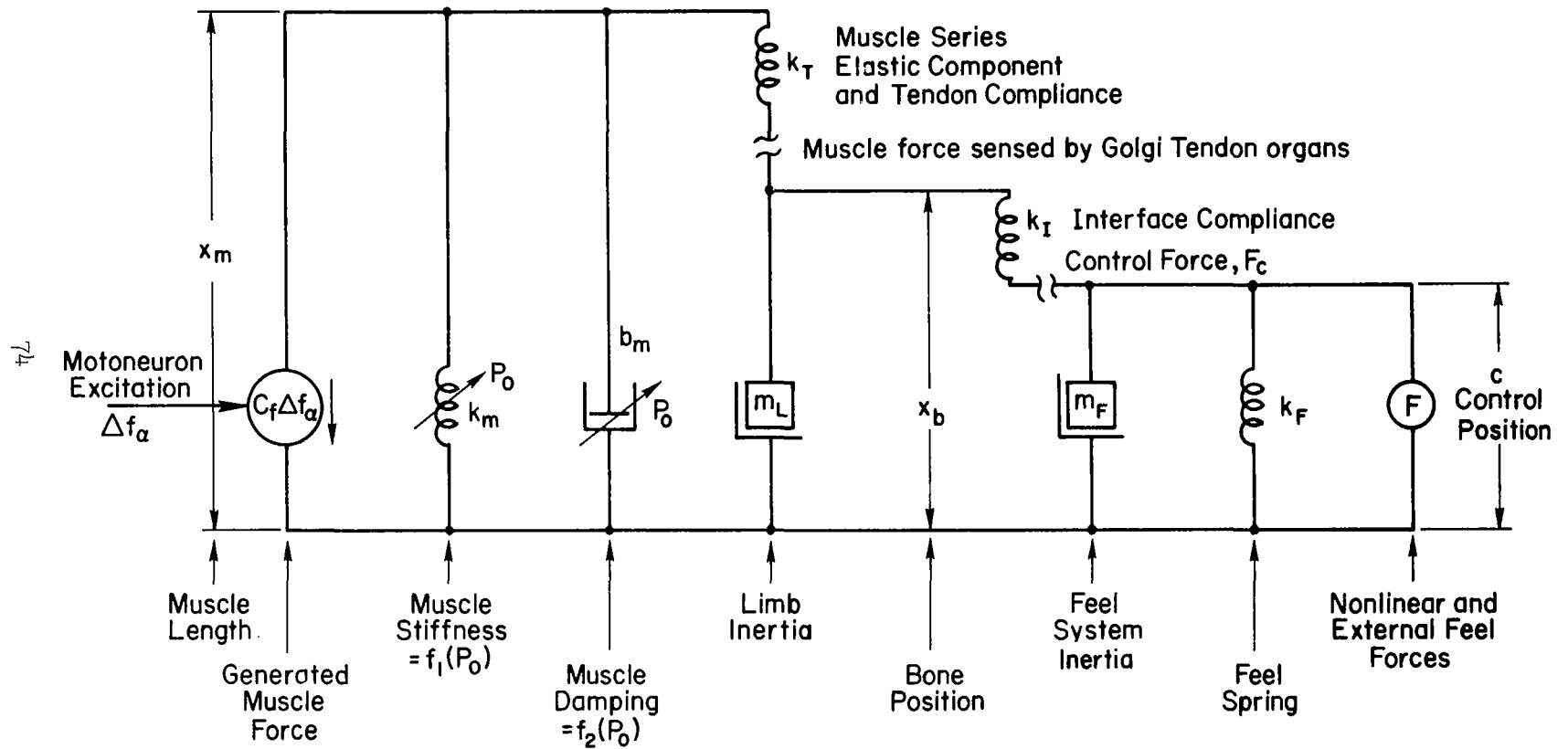
TABLE VII
EFFECTIVE TIME DELAY COMPONENTS

| Y_c | τ_c | τ_{NM} terms | τ_e |
|------------------------|----------|-------------------|----------|
| $\frac{1}{s-1}$ | 0.02 | 0.095 | 0.115 |
| $\frac{0.5}{s(s-0.5)}$ | 0.133 | 0.102 | 0.235 |

D. REVISED MUSCLE/MANIPULATOR DYNAMICS MODEL

The data presented in Section III and earlier in this section suggest revisions to the muscle/manipulator dynamics model (Ref. 1). Figure 35 shows a revised diagram of the muscle/manipulator elements. The muscle characteristics consist of a force source plus spring and damper where the latter two tend to increase with operating point tension, P_o . The muscle model also has a series elastic component (Ref. 23) which has been lumped into, k_T , the tendon compliance. The tendon compliance is connected to the limb inertia, m_L , and to, k_I , the interface compliance between the bone and the manipulator handle. The manipulator or feel system load is shown as an inertia and spring plus a force source to account for external disturbance forces and/or nonlinear feel system properties.

The major difference over the model in Ref. 1 is the addition of the interface compliance which will be used to explain the relative invariance of the neuromuscular peak for the extreme range of spring restraints



Note: $\Delta f_\alpha \propto x$ the measured effective actuation input to muscle/manipulator dynamics

Figure 35. Schematic Diagram of Muscle/Manipulator Elements

represented by the pressure and free-moving manipulator. Generally the tendon and interface compliances are large relative to k_m , the muscle stiffness.

The equations of motion for the muscle/manipulator dynamics can be found by setting the total force at c , x_b , and x_m equal to zero. In terms of Laplace transforms and written in matrix form these are:

$$\begin{bmatrix} (m_F s^2 + k_F + k_I) & -k_I & 0 \\ -k_I & (m_L s^2 + k_T + k_I) & -k_T \\ 0 & -k_T & (b_m s + k_m + k_T) \end{bmatrix} \begin{bmatrix} c \\ x_b \\ x_m \end{bmatrix} = \begin{bmatrix} F \\ 0 \\ -C_F \Delta f_\alpha \end{bmatrix} \quad (15)$$

These equations are quite similar to those in Eq. 13 of Ref. 1. (Note that in Ref. 1 the sign of $C_F \Delta f$ was wrong.)

Solving Eq. 15 for the manipulator position response to α motor neuron firing, Δf_α , yields (for $F=0$)

$$G_m = \frac{C}{C_F \Delta f_\alpha} = \frac{C}{X} = \frac{-1}{\Delta} \quad (16)$$

where x is proportional to $C_F \Delta f_\alpha$ and Δ is given by

$$\begin{aligned} \Delta = & \left[\frac{m_L b_m s^3}{k_T} + m_L \left(1 + \frac{k_m}{k_T} \right) s^2 + b_m s + k_m \right] \\ & + \left(\frac{m_F s^2 + k_F}{k_I} \right) \left[\frac{m_L b_m s^3}{k_T} + m_L \left(1 + \frac{k_m}{k_T} \right) s^2 + b_m \left(1 + \frac{k_I}{k_T} \right) s + k_m + k_I \left(1 + \frac{k_m}{k_T} \right) \right] \end{aligned}$$

In general the denominator indicates that G_m is a fifth-order system. However for very small values of the feel system inertia, m_F , the denominator is essentially third-order for any value of the feel system spring from $k_F=0$ (for free-moving manipulator) to $k_F \rightarrow \infty$ (for pressure manipulator). For $m_F=0$ the denominator can be written as

$$\Delta = \frac{m_L b_m}{k_T} \left(1 + \frac{k_F}{k_I} \right) \left[s^3 + \frac{(k_m + k_T)}{b_m} s^2 + \frac{k_T}{m_L} \left(1 + \frac{k_F/k_T}{1 + k_F/k_I} \right) s + \frac{k_T k_m}{m_L b_m} \left\{ 1 + \frac{k_F (1/k_m + 1/k_T)}{1 + k_F/k_I} \right\} \right] \quad (17)$$

Here k_F appears only in the constant and first power of s terms, i.e., the very highest frequency portion of Δ is invariant to load spring.

The effect of k_F variations can be found by combining the measured G_m given in Fig. 18 where the third-order roots are a real root at very high frequency and a heavily damped quadratic. For this root configuration the real root is approximated by the coefficient of the s^2 term in Eq. 17 which is the sum of the real part of all the roots and in this case is invariant with k_F . Any changes in the constant terms (coefficient of s^0) which is the product of all the roots then reflects the changes in, ω_a (Fig. 27) the natural frequency of the quadratic term. The values of the s^0 terms for the extremes of spring restraint are given in Table VIII.

TABLE VIII
EFFECT OF SPRING RESTRAINT ON s^0 TERM OF Δ

| SPRING RESTRAINT | s^0 TERMS |
|--------------------------------------|---|
| Free Moving $k_F = 0$ | $\frac{k_T k_m}{m_L b_m} \left\{ 1 \right\}$ |
| Pressure $k_F \rightarrow \infty$ | $\frac{k_T k_m}{m_L b_m} \left\{ 1 + k_I \left(\frac{1}{k_m} + \frac{1}{k_T} \right) \right\}$ |

Thus the s^0 term which reflects ω_a , the natural frequency of the quadratic mode, increases as the spring restraint becomes stiffer. This trend in the modes of G_m is consistent with the data in Fig. 30. Although the analysis leading up to Fig. 30 assumed that G_m did not change the trend

noted in Table VIII may provide an alternate explanation of the effects of feel system spring restraint.

As indicated earlier the major new element in Fig. 35 is k_I , the interface compliance. This element is important in that if it were assumed to be infinite then the denominator of G_m (Eq. 17) would contain only the terms in s^0 and s^1 . The measured data for G_m , rudder pedal with a stiff spring restraint and hand manipulator (isometric) are all third-order thus implying that a noninfinite k_I is indicated by the data.

Thus the data and model interpretations presented in this section illustrate the role of the closed-loop neuromuscular system in the overall human operator dynamics for a variety of controlled elements (some requiring lead). Consideration of the effects of a wide range of spring restraints has lead to a revised muscle/manipulator dynamics model to explain the data trends. More specific conclusions are given in the next section.

SECTION V

CONCLUSIONS

This report presents experimental describing function data for the muscle/manipulator actuation element, G_m , and the whole human, Y_p , for two manipulator types (hand manipulator and rudder pedals). The rudder pedal manipulator has an inherently balanced agonist/antagonist muscle system and consequently produced the highest quality data for the processed EMG signals. Response components at the sum of sine wave forcing function frequencies were well up out of the noise thus allowing high fidelity identification of G_m . The more specific conclusions are:

Muscle/Manipulator Dynamics

1. For the rudder pedal manipulator direct measurements of the muscle/manipulator dynamics reveal that this is a low pass third-order system with all modes at high frequency well above the tracking task crossover frequency. A heavily damped quadratic mode (greater than 10 rad/sec) and a single root (greater than 30 rad/sec) make up these modes.
2. G_m for rudder pedals and hand manipulator was quite similar in form and close in bandwidth despite the difference in limb size and function.
3. For the hand manipulator G_m was basically unchanged for first-, second-, and third-order subcritical tasks requiring none, first- and second-order lead respectively.

While the hand manipulator muscle system is more complicated (four unbalanced muscles with two major and two minor pairs) than the rudder pedal (two well matched muscles) the basic behavior is the same for tasks where the pilot needs none, first-order or second-order lead.

Human Operator Dynamics

1. High frequency peaks in Y_p are due to the closed-loop neuromuscular system. Using a curve fit to a direct measurement of the muscle actuation path and some simple but quite reasonable assumptions about the effective feedback path yields a closed-loop neuromuscular

system which gives an excellent fit to the data if the alpha command signal is the command input to the neuromuscular system. The feedback path assumptions imply that muscle spindles are the dominant element for stiff spring restraints although the Golgi tendon organs fulfill a similar role. In addition the joint angle sensors may modify the pilot's dynamics for free-moving manipulators.

2. The inherently balanced agonist/antagonist muscle set involved in the rudder pedal experiments yielded high quality data for the average tension and all the describing functions taken. This data shows that the pilot's effective time delay decreased as average tension increased. This is the first direct validation of this relationship.
3. The human operator's describing function for rudder pedals is nearly identical with that for hand manipulators, i.e., they both have high frequency peaks due to closed-loop neuromuscular systems. The effective time delay is slightly larger for rudder pedals.
4. The neuromuscular system organization is essentially unchanged for controlled elements where low-frequency lead is required compared with that when it isn't. Using this in some precision curve fits to the overall human operator allowed us to separate the pilot's effective time delay into central and peripheral components and isolate the time delay penalty involved in computing low-frequency lead.

The data in this report has validated the neuromuscular systems basic organization and dynamics in actual tracking situations. Once the detailed identification of model elements in G_m to match the data is done then the likely effects of control system nonlinearities (e.g., hysteresis, backlash, Coulomb friction, preload) on pilot/vehicle system stability and performance could be obtained via describing function analysis and/or simulation. This, in turn, should ultimately lead to a better understanding of some kinds of pilot-induced oscillations, and to the establishment of necessary or sufficient conditions for their elimination.

REFERENCES

1. Magdaleno, Raymond E., Duane T. McRuer and George P. Moore, Small Perturbation Dynamics of the Neuromuscular System in Tracking Tasks, NASA CR-1212, Dec. 1968.
2. McRuer, D. T., L. G. Hofmann, H. R. Jex, et al, New Approaches to Human-Pilot/Vehicle Dynamic Analysis, AFFDL-TR-67-150, Feb. 1968.
3. Elkind, J. I., Characteristics of Simple Manual Control Systems, MIT, Lincoln Laboratory, TR-111, 6 April 1956.
4. McRuer, D. T. and E. S. Krendel, Dynamic Response of Human Operators, WADC-TR-56-524, Oct. 1957.
5. Hall, I. A. M., Effects of Controlled Element on the Human Pilot, WADC-TR-57-509, Aug. 1958.
6. McRuer, Duane, Dunstan Graham, Ezra Krendel and William Reisener, Jr., Human Pilot Dynamics in Compensatory Systems: Theory, Models, and Experiments with Controlled Element and Forcing Function Variations, AFFDL-TR-65-15, July 1965.
7. McRuer, D. T. and R. E. Magdaleno, Human Pilot Dynamics with Various Manipulators, AFFDL-TR-66-138, Dec. 1966.
8. Magdaleno, R. and D. T. McRuer, Effects of Manipulator Restraints on Human Operator Performance, AFFDL-TR-66-72, Dec. 1966.
9. Jex, H. R., J. D. McDonnell and A. V. Phatak, A "Critical" Tracking Task for Man-Machine Research Related to the Operator's Effective Delay Time. Part I: Theory and Experiments with a First-Order Divergent Controlled Element, NASA CR-616, Nov. 1966.
10. McDonnell, J. D. and H. R. Jex, A "Critical" Tracking Task of Man-Machine Research Related to the Operator's Effective Delay Time, Part II: Experimental Effects of System Input Spectra, Control Stick Stiffness, and Controlled Element Order, NASA CR-674, Jan. 1967.
11. Jex, H. R. and R. W. Allen, A Psychomotor Task Battery for Manual Control Performance: Development, Validation, and Some Psychophysiological Correlates, Systems Technology, Inc., TR-175-1, forthcoming NASA CR-
12. Ruch, Theodore C. and Harry D. Patton (eds.), Physiology and Biophysics, W. B. Saunders Co., Philadelphia, 1965.
13. Boyd, I. A. and T. D. M. Roberts, "Proprioceptive Discharges from Stretch-Receptors in the Knee-Joint of the Cat," J. Physiol., Vol. 122, 1953, pp. 38-58.
14. Houk, J. and E. Henneman, "Responses of Golgi Tendon Organs to Active Contractions of the Soleus Muscle of the Cat," J. Neurophysiol., Vol. 30, 1967, pp. 466-481.

15. Houk, James and Elwood Henneman, "Feedback Control of Skeletal Muscles," Brain Research, Vol. 5, 1967, pp. 433-451.
16. Matthews, B. H. C., "Nerve Endings in the Mammalian Muscle," J. Physiol., Vol. 78, 1933, pp. 1-53.
17. Gray, Henry, Anatomy of the Human Body, Charles Mayo Goss (ed.), Lea and Febiger, Philadelphia, 28th Edition, 1966.
18. Bendat, Julius S. and Allan G. Piersol, Measurement and Analysis of Random Data, John Wiley and Sons, Inc., New York, 1966.
19. McRuer, Duane, "Remarks on Some Neuromuscular Subsystem Dynamics," IEEE Trans., Vol. HFE-7, No. 3, Sept. 1966, pp. 129-130.
20. Gordon-Smith, M., "An Investigation into Some Aspects of the Human Operator Describing Function While Controlling a Single Degree of Freedom," Fifth Annual NASA-University Conference on Manual Control, NASA SP-215, 1970, pp. 203-240.
21. Lippold, O. C. J., J. G. Nicholls, and J. W. T. Redfearn, "Electrical and Mechanical Factors in the Adaptation of a Mammalian Muscle Spindle," J. Physiol., Vol. 153, 1960, pp. 209-217.
22. Blackman, R. B. and J. W. Tukey, The Measurement of Power Spectra, Dover Publications, Inc., New York, 1958.
23. Wilkie, D. R., "The Mechanical Properties of Muscle," Brit. Med. Bull., Vol. 12, No. 3, 1956, pp. 177-182.
24. Bullard, E. C., F. E. Oglebay, W. H. Munk and G. R. Miller, A User's Guide to BOMM - A System of Programs for the Analysis of Time Series, Univ. of California at La Jolla, Inst. of Geophysics and Planetary Physics, Jan. 1966.
25. Jansen, J. K. S., and T. Rudjord, "On the Silent Period and Golgi Tendon Organs of the Soleus Muscle of the Cat," Acta Physiol. Scand., Vol. 62, 1964, pp. 364-379.